# SWITCHING ANALYSIS OF MAGNETIC VORTICES IN REDUCED DIMENSIONS UNDER PULSED ELECTRIC FIELDS

by
WAEL ALI SAEED AL-DULAIMI

Submitted to the Graduate School of Engineering and Natural Sciences
in partial fulfilment of
the requirements for the degree of Doctor of Philosophy

Sabancı University
December 2022

# ABSTRACT

SWITCHING ANALYSIS OF MAGNETIC VORTICES IN REDUCED DIMENSIONS UNDER PULSED ELECTRIC FIELDS

WAEL ALI SAEED AL-DULAIMI

Materials Science and Nanoengineering,
Ph.D DISSERTATION, DECEMBER 2022

Dissertation Supervisor: Prof. Dr. Burc Mısırlıoğlu

Keywords: Ferromagnetic nano-structures, vortex state, LLG equation, spintronics, micromagnetic simulations

The stability of magnetism in reduced dimensions has become a major scientific agenda in the pursuit of implementing magnetic nanostructures as functional components in spintronic devices. Methods to probe and control magnetization states of such structures in a deterministic manner include the use of spin polarized currents, photon absorption, and relatively recently, electric fields that tailor magnetoelectric coupling in multiferroic based structures. In theory, a short electric pulse is able to generate localized magnetic fields that can couple to the local magnetic dipoles electrodynamically. Here, using the Landau–Lifshitz–Gilbert formalism of magnetism dynamics combined with continuum Maxwell relations, the response of a ferromagnetic permalloy nanodisc to nanosecond electric field pulses is studied. The dynamics of the magnetic order of the nanodiscs during this process are examined and discussed. Ferromagnet nanodiscs, when below a critical size and in the absence of any external field, relax to a vortex phase as the ground state due to the demagnetizing field. Simulations demonstrate that the planar chirality of such a ferromagnet nanodisc can be switched via a time-wise electric field pulse on the order of a few ns duration that generates radially varying tangential magnetic fields. These fields couple to the vortex state of the nanodisc ferromagnet electrodynamically, revealing an effective and robust method to control chirality. Here, we focus on the analysis of the energetics of the reversal process. A strong thickness dependence of the chirality reversal in the nanodiscs is found that emanates from the anisotropy of the demagnetizing fields. Our results indicate that chiral switching of the magnetic mo-

ments in thin discs can give rise to a transient vortex-antivortex lattice not observed in thicker discs. This difference in the chirality reversal mechanism emanates from profoundly different energy barriers to overcome in thin and thicker discs. We also report the polarity-chirality correlation of a vortex that appears to depend on the aspect ratio of the nanodiscs.

# ÖZET

SWITCHING ANALYSIS OF MAGNETIC VORTICES IN REDUCED DIMENSIONS UNDER PULSED ELECTRIC FIELDS

WAEL ALI SAEED AL-DULAIMI

Malzeme Bilimi ve Nano Mühendislik
DOKTORA TEZİ, ARALIK 2022

Tez Danışmanı: Prof. Dr. Burc Mısırlıoğlu

Anahtar Kelimeler: Ferromanyetik nano yapılar, girdap durumu, LLG denklemi, spintronics, simülasyonlar

Düşük boyutlarda manyetizmanın kararlılığı, spintronik cihazlarda fonksiyonel bileşenler olarak manyetik nanoyapıların uygulanması arayışında önemli bir bilimsel gündem haline gelmiştir. Bu tür yapıların manyetizasyon durumlarını deterministik bir şekilde algılamak ve kontrol etmek için spin polarize akımların, foton absorpsiyonunun ve nispeten yakın zamanda, multiferroik tabanlı yapılarda manyetoelektrik eşleşmeyi uyarlayan elektrik alanlarının kullanımı öne çıkmaktadır. Teoride, çok kısa süreli bir elektrik sinyali, yerel manyetik dipollere elektrodinamik olarak eşleşebilen bölgesel manyetik alanlar üretebilir. Bu tezde sürekli ortam koşullarında Maxwell ilişkileri ile beraber ele alınabilen manyetizma dinamiğinin Landau-Lifshitz-Gilbert formalizmi kullanılarak, bir ferromanyetik permalloy nanodiskin nanosaniye elektrik alan sinyallerine tepkisi incelenmiştir. Bu işlem sırasında nanodisklerin manyetik düzeninin dinamikleri ve enerjilerinin değişimi incelenmiştir. Ferromanyetik nanodiskler, kritik bir boyutun altındayken ve herhangi bir dış alanın yokluğunda, manyetizmayı bastırıcı alan nedeniyle temel durum olarak bir girdap fazında kararlı hale gelebilir. Gerçekleştirdiğimiz simülasyonlar, bu tür bir ferromanyetik nanodiskin düzlemsel kiralitesinin, radyal olarak değişen teğetsel manyetik alanlar üreten birkaç ns süreli, zamana bağlı bir elektrik alan darbesiyle değiştirilebileceğini göstermektedir. Bu alanlar, nanodisk ferromanyetiğin girdap durumuna elektrodinamik olarak eşleşmekte ve kiraliteyi kontrol etmek için etkili ve güvenilir bir yöntem ortaya koymaktadır. Kiraliteyi tersine bir işarete çevirme sürecinin ener-

jisi de incelenmiştir. Nanodisklerdeki kiralitenin tersine çevrilmesinin güçlü derecede kalınlığa bağlı olduğu, manyetizmayı bastırıcı alanlarının şekil anizotropisinden kaynaklandığı düşünülmektedir. Sonuçlarımız, ince ferromanyetik disklerdeki manyetik momentlerin kiral değişiminin, daha kalın disklerde gözlenmeyen geçici bir girdap-antivorteks düzenlenmesinin de geçici olarak oluşabileceğini göstermektedir. Kiralitenin tersine çevrilme mekanizmasındaki bu fark, ince ve daha kalın disklerde aşılması gereken çok farklı enerji bariyerlerine işaret etmektedir.

## ACKNOWLEDGEMENTS

First, I would like to thank God for giving me the strength, knowledge, and opportunity to undertake this research study and complete it satisfactorily. Without his blessings, this achievement would not have been possible.

I would like to extend my appreciation and gratitude to those because of whom I was able to achieve this scientific work represented in this dissertation.

I would like to express my sincere gratitude to Prof. Dr. I. Burç Mısırlıoğlu for accepting me as his Ph.D. student. He has been there providing his support and guidance at all times and has given me invaluable inspiration and suggestions in my quest for knowledge. Without his able guidance, this thesis would not have been possible and I shall eternally be grateful to him for his assistance. Thank you for going the extra mile for all of us who depend on you. I simply could not be more grateful.

I am so thankful for Assoc. Prof. Dr.Özge Akbulut for accepting me on her team. To work for someone with leadership skills like hers is an incredible experience. she has taught me so much over the time that I spent in her group, and I want to thank her for that. The opportunity I got means so much to me, and I am so grateful.

I am grateful to those, who have taught, guided, and helped me during my PhD study. Prof. Dr. Kürşat Şendur, Assoc. Prof. Dr. Fevzi Çakmak Cebeci, Prof. Dr. Mehmet Ali Gülgün, Prof. Dr. Cleva Ow-Yang, Assoc. Prof. Dr. Gozde Ince, Prof. Dr. Melih Papila, and Assoc. Prof. Dr. Emre Erdem. Words cannot express how much I am grateful. I cannot thank you enough.

I would like to thank the scientific committee members and express my appreciation for your contribution to the thesis evaluation.

I owe special thanks to my colleagues, friends who I have had the gladness of working with, Can Akaoglu, Dr. Canhan şen, Dr. Omid Mohammad Moradi, Lyn Zemberekci, Dr. Merve Buldu, Mervenaz Şahin, Pouya Zoghipour, M. H. Aleinawi, Bilal Iskandarani, Dr. Ali Ansari at Sabancı University.

Last but not least, I would like to thank my parents and my elder brother for their endless support, especially my parents they offered a lot to support me. They have always been there to straighten, raise and guide me. To my wife, It helps to have

someone who understands what it is that you're going through and can relate to your situation. Thank you for being my wife, my family, and my best friend. It is so heartwarming, I am glad that my daughter could be part of this event, and thank you for being in my life.

I would like to appreciate the financial support of the Faculty of Engineering and Natural Sciences at Sabanci univeristy. Also, I acknowledge the financial support by TÜBİTAK through project number 117F042.

*In memory of my uncle*
**JASM ALANI**

## TABLE OF CONTENTS

## LIST OF TABLES

## LIST OF FIGURES

## LIST OF ABBREVIATIONS

FM : Ferromagnet .....

LLG : Landau–Lifshitz–Gilbert .....

MFM : Magnetic Force Microscopy .....

PY : Permalloy .....

q : Vorticity .....

c : Chirality .....

p : Polarity .....

H : Magnetic field Strength .....

B : Magnetic induction .....

$\chi$ : Magnetic susceptibility .....

$\mathbf{M}$ : Magnetization vector .....

$M_s$ : Saturation Magnetization .....

$\lambda$ : Phenomenological damping .....

$\gamma$ : Gyromagnetic ratio .....

$g$ : g-factor .....

$e$ : Electron charge .....

$m_e$ : Electron mass .....

$H_eff$ : Effective magnetic field (include internal and external terms) .....

$\alpha$ : Gilbert damping constant .....

$\tau_{STT}$ : Spin transfer torque .....

$P$ : Degree of spin polarization .....

$J$ : current density .....

$A$ : exchange constant .....

$K$ : Anisotropy constant .....

$\chi$ : Magnetic susceptibility .....

SP-STM : Spin-Polarized Scanning Tunneling Microscopy .....

GMR : Giant Magnetoresistance .....

RAM : Random Access Memory .....

MDM : Magnetic Dipole Moment .....

*"Every great and deep difficulty bears in itself its own solution.*
*It forces us to change our thinking in order to find it."*
**Niels Bohr**

**Preface**

The thesis focuses on developing and introducing an innovative method to manipulate the magnetization of the ferromagnetic (FM) nanostructures and analyse the switching process of the exotic vortex state. Localized control of the orientation of the magnetization poses significant challenges in existing conventional approaches (e.g. devices based on microelectromechanical, etc.), especially in nanostructures. Some of the proposed methods for manipulating the magnetism in magnetic nanostructures have been quite complex and cannot go beyond the laboratory scale (e.g. magnetic force microscope, etc.). How to control the orientation of the magnetization locally with a swift and stable manner in FM-based devices is one of the facts that limit the development of data storing/reading technology based on submicron structures. In this study, our main purpose is to examine the dynamics of a magnetic vortex state in FM nanostructures under time-dependent electrical pulses. The aim is to demonstrate the feasibility of altering the orientation of the magnetization of the FM, which is expected to have a vortex-type orientation in reduced dimensions, under special boundary conditions that are anticipated to be signal dependent at the interface. This is mainly possible by understanding how this time-dependent electrical pulses generate in-plane magnetic field which forces magnetic dipole moments (MDMs) to alter their orientation and align with the magnetic field direction. Another aim is to shed light on thickness/diameter ratio of a nanodisc which is intuitively expected to play a crucial role in the vortex state reversal dynamics. We find that the vortex dynamic and reversal are both related to the energy barrier that the reversal process has to overcome as well as the major difference in the transient configurations that a FM nanodisc of a given radius takes on depending on thickness. Our results are expected to provide an intuitive understanding of magnetic vortex dynamics focusing on use of time-dependent electrical pulses to control this exotic state in FM nanodisc.

Chapter 1 provides historical, conceptual, and experimental techniques to control magnetic vortex states. Additionally, the properties of a magnetic vortex state, and its applications are discussed in order. We also discuss the the fabrication techniques, the specific size and aspect ratio radius/thickness of a nanodisc that is required to nucleate a magnetic vortex state. The comprehensive introduction also include the methods and techniques that are proposed to control, form, and/or switch the magnetic vortex state and employ these methods for a wide range of applications in different disciplines such as; data storage, sensors, or cell actuators.

Chapter 2 discuss Landau–Lifshitz–Gilbert (LLG) equation, the effective field terms and the internal and external energy terms and how to compute these terms. In theory we also discuss the time dependent electrical pulses that are used to induce

in-plane Oersted magnetic field. We demonstrate that vortex's chirality and/or polarity states in a ferromagnetic nanodisc can be manipulated under the effect of an asymmetric or symmetric electric pulse applied along the z-axis, generating an Oersted field with a maximum strength along the disc rim.

Chapter 3 provides the numerical results obtained with finite-difference method implementing a simple first order forward Euler method in MATLAB [1], to understand the dynamics of a vortex state under applied time dependent voltage drop. The numerical results obtained by implementing Runge-Kutta method using the object-orientated micromagnetic framework (OOMMF) [2], is also provided to understand energy barriers effect and the effect of thickness and radius of a nanostructure on a magnetic vortex state reversal process. The thickness/diameter ratio of a nanodisc is expected to play a crucial role in the chirality reversal dynamics. We find that the vortex dynamic is related to the energy barrier. We also observed a major difference in the transient configurations that form in FM nanodiscs with different thicknesses and radii. It is not a surprising result that the demagnetization field computed across the thickness is higher for thinner discs. We show in the current work that it is this very reason raising the energy barrier during reversal of the chirality where the z-component of the magnetic moments are severely restricted in thin structures. It is deduced that the ease with which components along the disc normal can align, even if transiently, have a profound impact on the switching fields. Moreover, whether or not chirality and polarity are intimately coupled to each other has been another topic of debate in relevant papers. The apparent reason for this stems from the possibility that a change in chirality could be possible to detect via the polarity change and vice versa. We identified that the relation or coupling between polarity and chirality can differ as a function of nanodisc thickness or aspect ratio, likely related to the difference in the demagnetization fields along the disc normal. The results imply that, apart from the material type, the thickness of a ferromagnetic nanodisc determines the field amplitudes necessary to enable easy reversal of chirality in nanosecond durations, likely placing extrinsic limits on functionality of topological states for spintronic applications.

The last chapter in the thesis focuses on the future work for magnetic vortex control and we may include the thermal effect, Joule heating, or study different exotic state such as skyrmions, solitons.

# 1. INTRODUCTION

## 1.1 Historical context

Understanding the behavior of nanoscale materials has become the focus of both device design and basic scientific studies. Essentially these two concepts, namely device design and basic scientific research, feed each other. Data storage applications, which are one of the most important components of digital technology, and the expectation of "saving more information in smaller volumes" in new generation devices have triggered intensive basic research especially to examine the functionality of magnetic materials at very low dimensions (submicron and less). Crystalline magnetic materials of low size where the surface area is larger compared to the volume, in such geometries they can have quite different properties such as; Curie points, magnetic permeability, and moment direction. Shape anisotropy is essentially insignificant compared to the spin-orbital interaction that the structure shows in bulky form, it becomes a very important energy term at low dimensions. Especially if at least one of the magnetic material dimensions (for example, planar dimensions) approaches to the degree of classical Neel and Bloch type domain wall widths, the configurations that contain such domain walls minimize the "demagnetization" energy and thereby become thermodynamically stable. This is mainly because the "domain wall energy" reaches levels comparable to the volumetric energy of the material [3]. One of the best examples is a vortex configuration in thin-film structures, nanodots and discs that are frequently studied at sub-micron scale and have a high surface/volume ratio. Theoretically, Abrikosov has predicted that vortex-type in solid nanostructures will first form in Type II superconductors, and the study is showing that vortices can interact with each other and the magnetic field can penetrate with quantized flux into the superconducting materials. Above mentioned study was the first publication to discuss the possibility of magnetic vortex-type formations in solids under the influence of the magnetic field [4]. Then, in 1967, a magnetic vortex formation in Type II superconductors was observed for the first time (See Fig. 1.1, [5]).

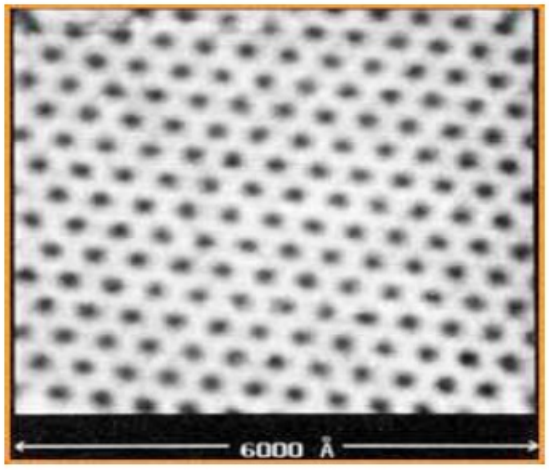


**Figure 1.1** Nb-based oxide "Abrikosov mesh" formed in a Type II superconductor [5]. Reprinted figure with permission from H. F. Hess, R. B. Robinson, R. C. Dynes, J. M. Valles, Jr., and J. V. Waszczak Phys. Rev. Lett. 62, 214 (1989) https://doi.org/10.1103/PhysRevLett.62.214. Copyright (2022) by the American Physical Society.

Recently, due to the emergence of advanced characterization techniques, it has been shown that magnetism or ferroelectric polarization, which is an analog system, can preserve a vortex type configuration and such a configuration can be stable in low-dimensional material structures [6–10]. As mentioned above, this type of orientation is observed in magnetic nanostructures that are getting smaller and smaller based on both device design and basic research efforts. The physical properties such as the coercivity, permeability, and Curie point of magnetic structures with vortex configurations are of great interest for research and applications. Attempts to make use of this configuration type, which is formed stably in low-dimensional circular, square, and triangular structures, in magnetic memory technology have just started [7]. It seems possible to express "1" or "0" in the binary system if the vortex chirality is clockwise or counterclockwise. It was shown in the 2013 study of Uhlit et al. that these two different vortex states can be read with the magnetoresistance effect [11]. In addition, the polarity of the vortex which describes the magnetization at the vortex core which is pointing out of the plane either "up" or "down", which is another possibility of maintaining double bits in a single dot as a free parameter. This approach is defined as "spin texture".

Magnetic nanostructures with vortex state attract great attention due to their exotic characteristics, but localized manipulation of the vortex states is almost impossible with applying the "external magnetic field" in existing conventional techniques. The main problem here is that current techniques are insufficient to confine the magnetic

field in a small volume. For example, recently Noske and his colleagues have been working on "vortex control and reversal of vortex polarity by two perpendicular in-plane magnetic field pulses", however, their research focuses on the study of the vortex formation dynamics on a laboratory scale and manipulation techniques are not valid in practice [12]. Although many theoretically published works investigating how the vortex states might respond to an external magnetic field [6, 13–15], how to generate this magnetic field locally in a real application remains unclear. In another study, it has been shown by simulation that a vortex state reversal can be obtained under the effect of an inhomogeneous magnetic signal, but in this study, the localized signal is far from being applied [16]. In a few laboratory-scale experimental studies, it has been reported that the magnetic vortex configuration, which occurs at nanoscales, can be tightly controlled by means of a magnetic force microscope (MFM) modified with a pointed magnetic tip (For example, see [17]). In another study, permalloy (PY) high quality nanodiscs with a diameter of approximately 100 nm were produced and a magnetization with vortex state was detected before and after applying a synchroton radiation (See Fig. 1.2, [18, 19]).

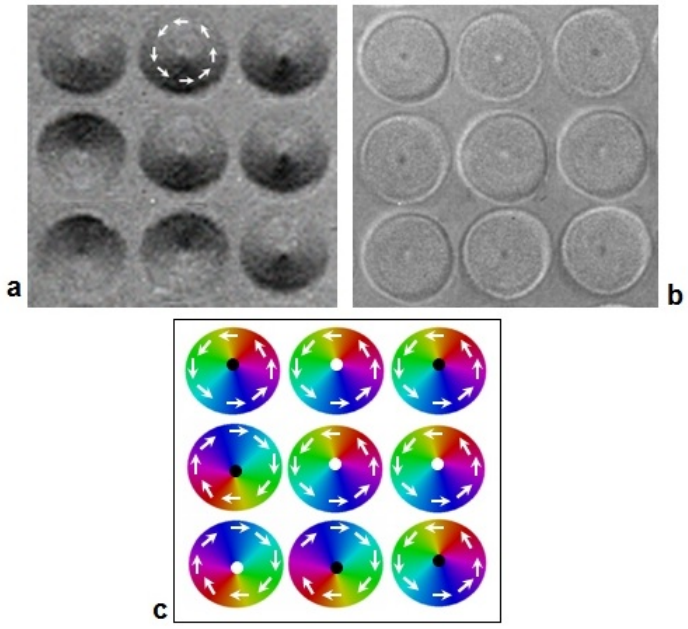


**Figure 1.2** magnetic transmission soft X-ray microscopy images of in-plane (a) and out-of-plane (b) magnetic components taken at the remanent state in a 100-nm-thick nanodisks. (a) The chirality of the in-plane magnetization is indicated by a white arrow. (b) The black and white spots of the central regions in nanodisks are upward and downward vortex polarities. (c) The vortex state of each nanodisc is also illustrated [19]. Reprented from Im, M-Y. et al. Symmetry breaking in the formation of magnetic vortex states in a permalloy nanodisk. Nat. Commun. 3:983 (2012), https://doi.org/10.1038/ncomms1978. with the permission of Springer Nature.

## 1.2 Origins of Ferromagnetism

The magnetic characteristics of materials are carried by the spins of the electrons and their orbital motion in the atoms. The material's crystal structure and electronic configuration determine the magnetism of the substance. The magnetic behavior of materials can be classified into the following five major groups: Diamagnetism, ferromagnetism, antiferromagnetism, ferrimagnetism, and paramagnetism.

Certain electrically uncharged materials have a significant attraction to one another due to a physical phenomenon known as Ferromagnetism. Lodestone (or magnetite, an oxide of iron, $Fe_3O_4$) and iron are two naturally occurring minerals that have the capability to have such attraction properties and are sometimes referred to as natural ferromagnets. They were the subject of all early scientific investigations into magnetism. Today, a wide range of everyday necessities, such as electric motors and generators, transformers, phones, and loudspeakers, all require ferromagnetic materials.

Three fundamental rules that govern how electrons fill-up orbitals are what determine the electron configurations of atoms. First, Aufbau (Building-Up) Principle simply state: Electrons are inserted into the atomic orbitals filling from bottom to top, from lowest to highest energy. Second, Hund's rule [20], If orbitals are degenerate (equal energy), and being filled, the electrons are inserted into separate orbitals before they are spin paired with another electron in the same orbital. In other words, Hund's rule requires lone electron occupancy before pairing. Finally, according to Pauli's Exclusion Principle [21], no two electrons in the same atom can have the same quantum numbers. In other words, two electrons in the same orbital must have opposing spins and no more than two electrons may occupy the same orbital. Since some of the electrons in some materials are unpaired, their atoms have a net magnetic moment. Large numbers of atoms' moments ($10^{12} - 10^{15}$) are aligned parallel in regions known as magnetic domains. Due to the existence of magnetic domains a strong magnetic field is acquired, and these materials have high magnetic characteristics and known as Ferromagnetic materials. A limited number of elements in the periodic table exhibits ferromagnetism properties. The electrons in $d$ shell of transition metals are carriers that orbit itinerant about atoms. $3d$ metals (Ni, Co, Mn, Fe) are elements that exhibit ferromagnetic properties among other elements. There are also some $4f$ and $5f$ elements exhibit ferromagnetism. Although, the electrons in $4f$ elements are localized separately, however, they behave collectively as the behavior of nearly free electrons of $3d$ metals, example of these elements are

$4f$ elements (Tb, Gd, Dy, etc.).

Ferromagnetic materials exhibit spontaneous magnetization without the influence of external magnetic field. And the reason behind that is the precise equilibrium between the exchange interaction and the atomic hybridization. The exchange interaction is dominant between the conduction band electrons in ferromagnetic materials. The exchange interaction forces the spins to form parallel configuration while the atomic hybridization tries to prevent spins alignment. Heisenberg exchange interaction illustrates the relation between these two interactions as shown below in Eqn. 1.1:

$$E_{His} = -2J_{ex}S_iS_j\ cos\theta \tag{1.1}$$

where $J_{ex}$ is known as the exchange coupling constant and $\theta$ is the angle between the spins $S_i$ and $S_j$ [22]. The Pauli exclusion principle keeps the electrons with the same spin far away and that reduces the Coulomb repulsion between electrons, accounting for the energy gain from spin alignment [23]. Band theory describes electron states in metals, and the band structure is determined by the kinetic energy, and exchange energy needed to fill electrons into one spin band [24]. The exchange interaction is very strong. It will cause a splitting of the $d$-bands and rearranging of the $3d$ bands. This leads to a larger concentration of spin-polarized carriers known as majority charge carriers ($N_+(E_F)$) and a smaller concentration known as minority charge carriers ($N_-(E_F)$), and this imbalance in the charge concentration leads to ferromagnetism [23]. Stoner criterion imposes a condition for the emergence of the ferromagnetic order in a simplified solid model which is given below in Eqn. 1.2:

$$J_{ex}(E_F)DOS(E_F) > 1 \tag{1.2}$$

where $DOS(E_F)$ is the density of states at the Fermi level $E_F$ highest energy level occupied with electrons and $U = J_{ex}(E_F)$ is the Stoner parameter, which is a measure of energy reduction and depends on a material type. The Stoner criteria make it clear that materials with a substantial DOS at the Fermi level and a strong exchange interaction will exhibit ferromagnetism. Fig. 1.3 presents the density of states and illustrates the splitting of $3d$ band.

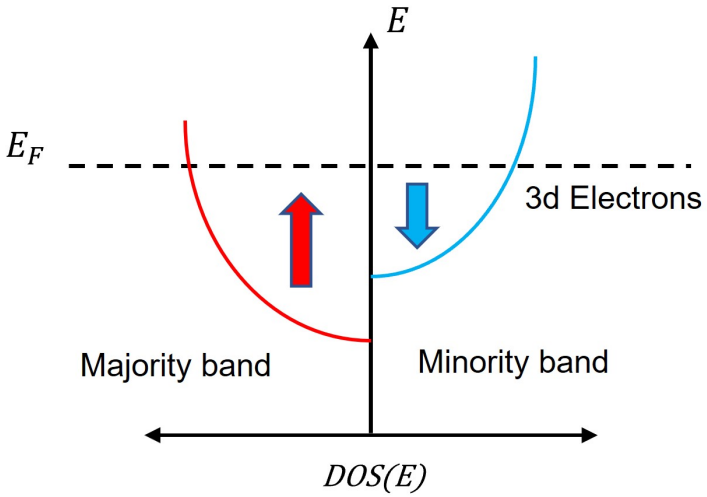


**Figure 1.3** A band structure of a FM metal showing the splitting of a 3d band. The majority carriers density of states (red region) and the minority carriers density of states (blue region).

### 1.2.1 Mean field approximation

Ferromagnetic materials (e.g. Fe, Ni, Co) have a non-zero magnetization $M \neq 0$ under zero external magnetic field $B_{ext} = 0$ below a critical curie temperature (Tc). The exchange interaction between spins is well described by Heisenberg model, and it is a more realistic model for modelling ferromagnetism. The Hamiltonian of the isotropic Heisenberg model is given by [25]:

$$H = -J_{ex} \sum_{i}^{N} \mathbf{S_i} \cdot \mathbf{S_j} - \mu B_{ext} \sum_{i} S_i^z \tag{1.3}$$

where $J_{ex}$ is the exchange coupling constant between the spins on sites $i$ and $j$, N is the nearest neighbor sites $j$ of lattice site $i$. $\mu = g\mu_B/2$ is the magnetic moment, $g$ is the Landé g factor, and $\mu_B$ is the Bohr magneton.. Under a reasonable assumption, the spin interaction is weak and disappears for all lattice sites further away from each other and it strong only between the neighboring spins. In ferromagnetism, $J_{ex} < 0$ and parallel spins decrease the system energy. In antiferromagnetism, $J_{ex} > 0$ and antiparallel spins decrease the energy, and for paramagnetism $J_{ex} = 0$.

The mean field approximation main notion is to replace the interaction of two neighboring spins by the interaction of a single spin of site $i$ with the mean spin value $< \mathbf{S} >$ of its surrounding:

$$\mathbf{S_i} \cdot \mathbf{S_j} \longrightarrow \mathbf{S_i} \cdot < \mathbf{S} > \tag{1.4}$$

The mean field Hamiltonian is given by:

$$H = \sum_i \mathbf{S_i} \cdot (nJ_{ex} < \mathbf{S} > + \mu \mathbf{B_{ext}}) \tag{1.5}$$

where $n$ is the coordination number (number of nearest neighbor sites of spin $i$) The term between the parentheses is total magnetic field consisting of the applied magnetic field $B_{ext}$ and the mean magnetic field $B_{MF}$ which is given by:

$$\vec{B}_{MF} = \frac{1}{\mu} nJ_{ex} < \mathbf{S} > = \frac{nJ_{ex}}{\mu^2 N_s} \mathbf{M} \tag{1.6}$$

where $\mathbf{M} = N_s \ \mu < \mathbf{S} >$ is the magnetization, $N_s$ is the spin density. The energies of the magnetic states are written as:

$$E = -\vec{\mu} \cdot \mathbf{B_{total}} = -m_J \ g \ \mu_B B_{total} \tag{1.7}$$

The magnetic moment of an atom depends on the total angular momentum quantum number $J$. Since the magnetic quantum numbers are restricted to the values $m_J = (J, J+1, , J1, J)$. Here $m_J = \pm\frac{1}{2}$, The occupation probabilty $p$ of the state is given by a Boltzmann distribution [25, 26],

$$p = \frac{\exp(\frac{-E}{K_B T})}{\sum\limits_{m_J=-J}^{m_J=J} \exp(\frac{-E}{K_B T})} \tag{1.8}$$

For a spin $\frac{1}{2}$ where $J = \frac{1}{2}$, there are two states spin-up favor the direction of the B field and spin-down favor the antiparallel direction to the B field. The spin up state has a higher occupation. The occupations of spin-up and spin-down can be written as:

$$\frac{N_\uparrow}{N} = \frac{\exp(\frac{\mu B}{K_B T})}{\exp(\frac{\mu B}{K_B T}) + \exp(\frac{-\mu B}{K_B T})} \tag{1.9}$$

$$\frac{N_\downarrow}{N} = \frac{\exp(\frac{-\mu B}{K_B T})}{\exp(\frac{\mu B}{K_B T}) + \exp(\frac{-\mu B}{K_B T})} \tag{1.10}$$

Where $B = B_{total}$, $N = N_\uparrow + N_\downarrow$ is the total number of states, $N_\uparrow$ is the number of spin-up states, and $N_\downarrow$ is the number of spin-down states. The magnetization per unit volume is given by:

$$M = \mu \frac{N_\uparrow - N_\downarrow}{V} \tag{1.11}$$

By substituting the occupation probabilities Eqn. 1.11 becomes:

$$M = N_s \ \mu \ \tanh\left(\frac{\mu B_{total}}{K_B T}\right) = M_s \tanh\left(\frac{\mu B_{total}}{K_B T}\right) \tag{1.12}$$

where $M_s$ is the saturation magnetization. To investigate the property of ferromagnetism (the spontaneous magnetization) the external field is set to zero so the $B_{total} = B_{MF}$. Eqn. 1.12 becomes:

$$M = N_s \ \mu \ \tanh\left(\frac{\mu B_{MF}}{K_B T}\right) = N_s \ \mu \ \tanh\left(\frac{\mu n J_{ex} M}{g^2 \mu_B^2 N_s K_B T}\right) \tag{1.13}$$

because $B_{MF}$ depends on $M$, therefore, Eqn. 1.13 is self-consistent equation of state of $M$. By inserting $\mu = \frac{1}{2} g \mu_B$, Eqn. 1.13 can be written as:

$$M = N_s \ \frac{1}{2} g \mu_B \ \tanh\left(\frac{\frac{1}{2} g \mu_B n J_{ex} M}{g^2 \mu_B^2 N_s K_B T}\right) = M_s \ \tanh\left(\frac{n J_{ex} M}{2 g \mu_B N_s K_B T}\right) \tag{1.14}$$

Where $M_s = N_s \ \frac{1}{2} g \mu_B$, and by inserting $T_c = \frac{n J_{ex}}{4 K_B}$(Curie temperature) Eqn. 1.14 can be simplified to:

$$M = M_s \ \tanh\left(\frac{T_c M}{T M_s}\right) \tag{1.15}$$

$$m = \tanh\left(\frac{m}{t}\right) \tag{1.16}$$

Where $m = M/M_s$ is the reduced magnetization and $t = T/Tc$ is the reduced temperature. One way to solve this equation is to plot lhs. and rhs. of Eqn. 1.16 separately as functions of m. The solution of the equation are the points where the curves for the lhs. and rhs. intersect. Fig. 1.4 shows this procedure for some values of $t$ [27].

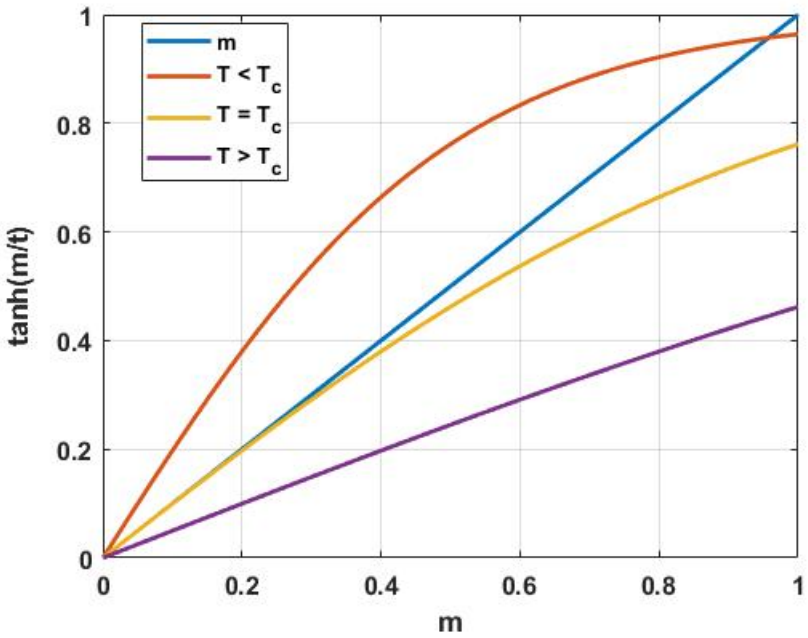


**Figure 1.4** Graphical solution of Eqn. 1.16 for the reduced magnetization as a function of temperature. The lhs. of Eqn. 1.16 is plotted as a straight line m with unit slope. The rhs. of Eqn. 1.16 is plotted as function of m for three different values of the reduced temperature. The three curves correspond to the temperatures $T > T_c$, $T = T_c$ and $T < T_c$.

The curve for $T > T_c$ intersects the straight line m only at $m = 0$ which is the paramagnetic region. The curve for $T = T_c$ is tangent to the straight line m at the origin; this temperature $T = T_c$ is the critical temperature for the phase transition from the ferromagnetic to the paramagnetic phase. The curve for $T < T_c$ is in the ferromagnetic region a spontaneous magnetization can occur. It intersects the straight line m at $\approx 0.94$. When $t$ approaches zero $t \to 0$, $m = 1$ which means that all the magnetic moments are aligned up at absolute zero Kelvin [27]. Another way to solve Eqn. 1.16 of the magnetization numerically for various values of t. The result shown in the Fig. 1.5 for the curve M vs. T reproduce roughly the features of the experimental results. The magnetization gets lower as T increases, and smoothly approaches zero as $T \to T_c$

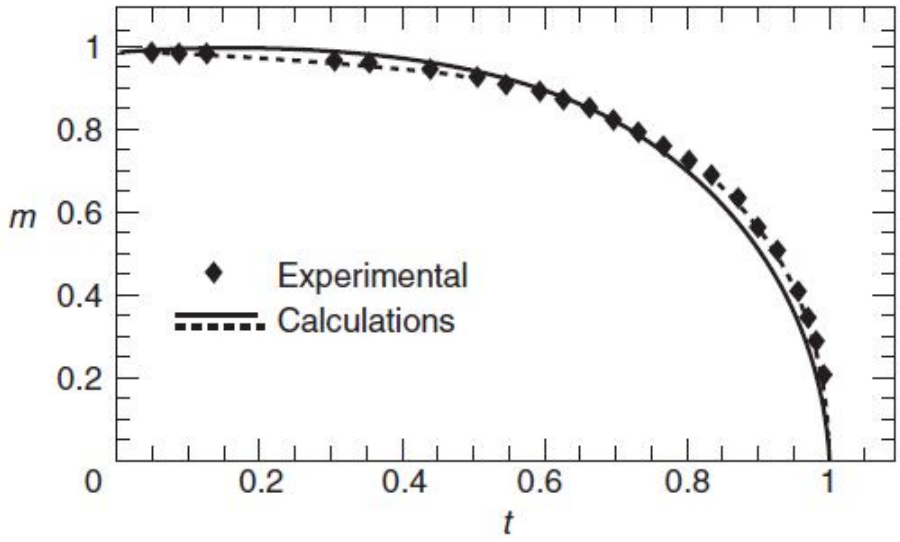


**Figure 1.5** Experimental results (diamonds) show the saturation magnetization of nickel as a function of temperature, together with theoretical curve for $J = S = \frac{1}{2}$ on the mean field theory. The black line is obtained from Eqn. 1.16. The dashed line describes the critical behavior near $T_c$ and includes the spin wave excitation [28]. Reprinted from Magnani, N. (2005). Ferromagnetism. In F. Bassani, G. L. Liedl, P. Wyder (Eds.) Encyclopedia of Condensed Matter Physics, (pp. 201–210). Oxford: Elsevier, https://doi.org/10.1016/B0-12-369401-9/01115-3, Copyright, with permission from Elsevier

### 1.2.2 Magnetic susceptibility and Curie-Weiss law

In general, the magnetic susceptibility is defined as how easily a material can be magnetized under an applied magnetic field [25].

$$\chi = \mu_0 \frac{\partial M}{\partial B_{ext}}|_{B_{ext}=0} \tag{1.17}$$

We recall the expression for the magnetization:

$$M = N_s \frac{1}{2} g\mu_B \tanh(\frac{g\mu_B B_{total}}{2K_B T}) \tag{1.18}$$

At high temperatures above $T_c$, Eqn. 1.18 is expended with $tanh(x) \approx x$ for $x \ll 1$.

$$M \approx N_s \frac{1}{2} g\mu_B (\frac{g\mu_B B_{total}}{2K_B T}) = N_s \frac{g^2\mu_B^2}{4K_B T} (B_{total}) \tag{1.19}$$

It is possible to simplify Eqn. 1.19 with the definition of the critical temperature $T_c = \frac{nJ_{ex}}{4K_B}$:

$$M \approx \frac{N_s g^2 \mu_B^2}{4K_B} \frac{B_{ext}}{T - T_c} \tag{1.20}$$

Substituting this expression in Eqn. 1.17 one gets the so-called **Curie-Weiss** law [27]:

$$\chi = \frac{C}{T - T_c} \tag{1.21}$$

Where $C = \frac{\mu_0 N_s g^2 \mu_B^2}{4K_B}$, With this law one can model the magnetic susceptibility above $T_c$ (paramagnetic behavior). One needs different models for magnetic susceptibility below $T_c$. The magnetic susceptibility and its reciprocal as function of temperature are shown in Fig. 1.6.

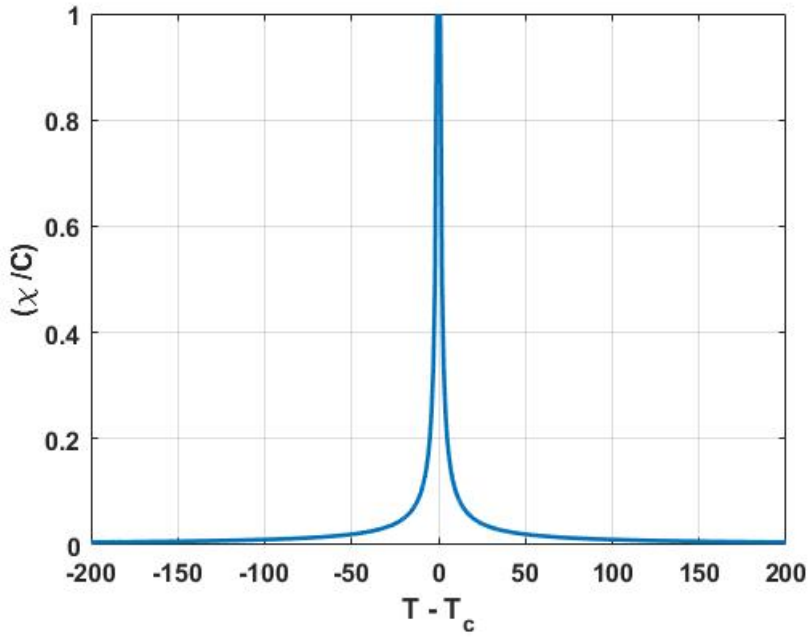


**Figure 1.6** Magnetic susceptibility in the vicinity of the Curie temperature.

## 1.3 A unique ground state in nanostructures: Magnetic vortex state

Ferromagnetic materials form magnetic domains to reduce the energy. Two neighboring domains that have different directions of magnetization form a transition region, this region is known as a domain wall. Over this region the magnetization continuously switches from its direction in one domain to that in the other [29, 30]. In general, there are two types of domain wall: Néel wall and Bloch wall which are depicted in Fig. 1.7. In a Bloch domain wall, the magnetization vector field turns around the normal of the domain wall, while in a Néel wall the magnetization vector field turns around a line that is orthogonal to the normal of the domain wall.

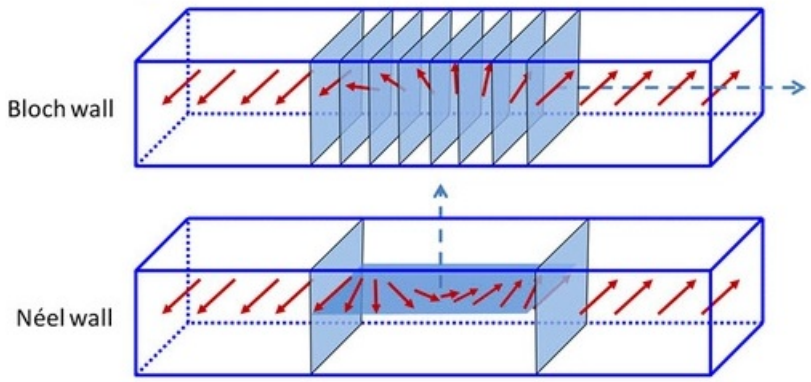


**Figure 1.7** Schematic depicting a Bloch and a Néel domain walls. The dashed arrows show the axis of rotation of the magnetization [31]. Reprinted from Bhatia, E., Barber, Z. H., Maasilta, I. J., Senapati, K. (2019). Domain wall induced modulation of low field ht phase diagram in patterned superconductor-ferromagnet stripes. AIP Advances, 9 (4), 045107, https://doi.org/10.1063/1.5087925, with the permission of AIP Publishing.

If a ferromagntic film has a small thickness, the Néel wall will exchange with the Bloch wall. A magnetic topology defect will form in the intersection of two Néel walls.

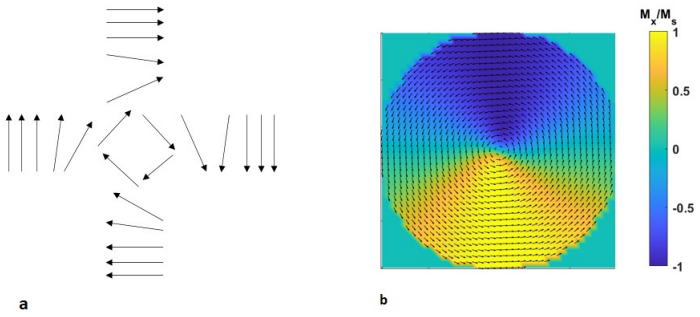


**Figure 1.8** (a) The intersection of two Néel walls forms a vortex state. (b) The planner view of a magnetic vortex in a FM nanodisc.

A magnetic topology defect forms when the structure is on the order of domain wall widths and is a way to minimize the total energy of the system. Three specific features characterize a magnetic topology defect: vorticity (q), chirality (C), and polarity (P). The vorticity also known as the winding number is a measure of total angle of spin field with respect to a given in-plane orientation through which the spin vector field curls in a rotational path around the center [32]. The chirality is a measure of the spin field rotation direction either clockwise or counterclockwise, while the polarity is defined as the magnetic moments direction along the normal to the plane inside the vortex core either up or down. The combination of the chirality and polarity allows a vortex to attain four degenerate states shown in Fig. 1.9 [33–35].

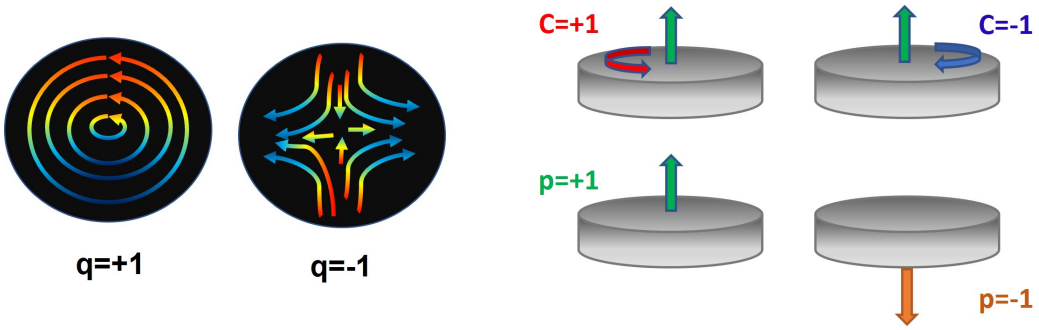


**Figure 1.9** Ferromagnetic exotic vortex and antivortex states: vorticity ($q = \pm 1$), polarity ($P = \pm 1$) and chirality ($C = \pm 1$).

In theory, the configuration of a magnetic vortex state has been anticipated long before, however, practical observation see the light lately. Nowadays and due to exceedingly advanced nanotechnology, one can prepare samples with nano-dimensions and characterize these samples with spectroscopy techniques. Shinjo et al. reported the first experimental observations of a magnetic vortex state utilizing magnetic

force microscopy (MFM) to probe circular discs of permalloy (PY) ($Ni_{80}Fe_{20}$) prepared by means of electron-beam lithograph, they did detect the vortex polarity at the center of the discs and provide a clear prove of the presence of a vortex state (See Fig. 2 in Ref. [33]). They obtained images that appear to have white and dark spots at the centers of the discs. The authors point out that each disc attains a magnetic vortex state and the magnetization in these white and dark spots has an opposite direction which represents the polarities of these magnetic vortices. However, there are resolution limits in the MFM technique; (i) The lateral resolution of MFM is between 20 nm to 100 nm, thus, the actual size of a magnetic vortex core cannot be determined. (ii) The magnetic stray field can easily affect the vortex state as the distance between the device tip and the surface of the sample gets very small. (iii) Finally, it cannot specify the internal spin structure. Fortunately, another technique can resolve these fine structures known as spin-polarized scanning tunneling microscopy (SP-STM)[35]. This technique can resolve magnetic domain walls [36], and it can go down to atomic scale [37]. Also, depositing antiferromagnetic layers on the device tip can prevent any dipolar interaction between the scanning tip and sample, and depending on the thickness of these deposited layers, different sensitivities can be obtained either in-plane or out-of-plane [38]. SP-STM is used to find magnetization orientation in a sample by measuring differential conductance $\frac{dI}{dU}$ which is given in the following formula:

$$\frac{dI}{dU}(\vec{r}, U_o)_{SP} = C(1 + P_T P_s \ cos\theta) \tag{1.22}$$

where $\vec{r}$ is the position on the surface, $U_o$ is the sample bias voltage, C is the spin-averaged differential conductance, $P_T$ is the spin polarization of the tip at Fermi energy $E_F$, $P_s$ is the spin polarization of the sample at the energy $E_F + eU_o$, and $\theta$ is the angle between tip magnetization $M_T$ and the local sample magnetization $M_s(\vec{r})$ below the tip. The $dI/dU_o$ map of in-plane magnetization utilizing a in-plane sensitive tip (See Fig. 3(A) in Ref. [35]). The $dI/dU_o$ map of out-of-plane magnetization utilizing a out-of-plane sensitive tip (See Fig. 3(B) in Ref. [35]), which exhibits a small bright area roughly in the center of the island. (Fig. 3(C) in Ref. [35]) shows $dI/dU_o$ signal along the circle path around the vortex core, the signal indicates that the sample in-plane magnetization component at a distance 19 nm from the vortex core continuously curls around the core. The $dI/dU_o$ signal measured along the lines plotted in (Fig. 3(A) and 3(B) in Ref. [35]) is shown in 3(D), utilizing this signal the core size was determined, which is found approximately equal to 9 nm.

Vortex configuration in the magnetic state has unique properties such as a minimum

stray field, faint interaction between the adjacent discs in arrays, and high stability against thermal fluctuations [39–44].

### 1.3.1 Domain Wall Length, Exchange Length, and Characteristic Length

In micromagnetic simulations, there are two parameters that one needs to consider to determine the cell size (discretization length $\Delta$) for a specific magnetic material [45]: First, domain wall Length; Mathematically is defined as $\delta = \sqrt{\frac{A}{k}}$ (SI), where A is the exchange constant in $J/m$, and $K$ is the anisotropy constant in $J/m^3$. In a hard material, the dominant energy term is crystalline anisotropy, and the typical domain wall length is equal to that of the Bloch domain wall, in that case, it is normal to define the domain wall length as magnetocrystalline exchange length. In this type, there is a competition between the anisotropy field which forces the wall towards its collapse, and the exchange field which tries to expand it. Second, exchange Length mathematically is defined as $l_E = \sqrt{\frac{2A}{\mu_0 M_s^2}}$ in (SI), where $\mu_0$ the permeability of free space, and $M_s$ is the saturation magnetization. $l_E$ is the length below which atomic exchange interactions dominate the typical demagnetization fields, so it measures the relative strength of exchange to demagnetization energies. To capture the most fine features in micromagnetic simulations such as, domain walls, defects, nucleation and annihilation, vortex states, and anti-vortex states, one needs to discrete the magnetic system into fine unit cells with $\Delta$ that is less than the exchange length of a specific magnetic material [46]. Indeed, if $\Delta$ across a domain wall is too coarse, the demagnetization energy will dominate and lead to the collapse of the domain wall, and eventually false simulation. An example of coarse grid simulation ($\Delta$=15 nm) leads to a weak exchange field and a strong demagnetization field which forces the Neel wall to collapse into a configuration as shown in Fig. 1.10(a). A fine mesh grid ($\Delta$=5 nm) is utilized to resolve the problem See Fig. 1.10(b).

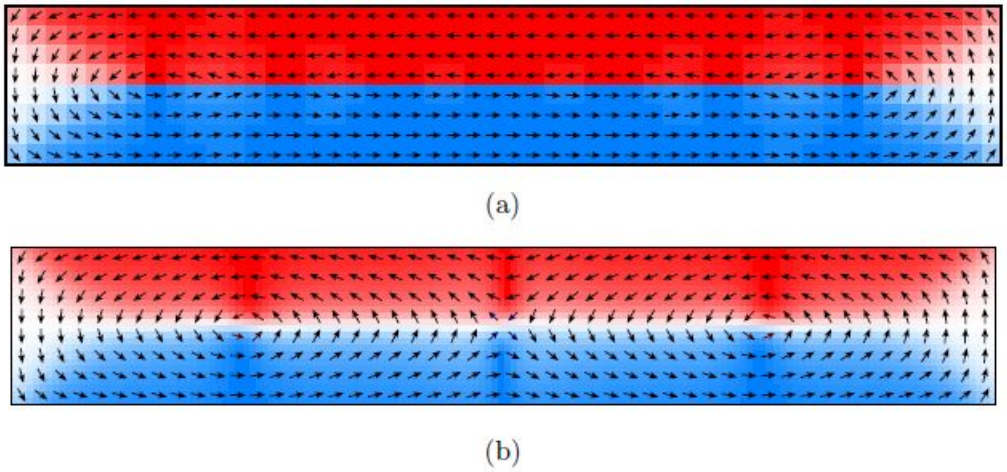


**Figure 1.10** Magnetization vector map illustrates Neel wall in $Ni_80Fe_20$ rectangle, equilibrium states. (a) Coarse grid ($\Delta$=15 nm) leads to wall collapse, compared to (b) fine grid ($\Delta$=5 nm) which keeps the wall. The colormap shows $M_x$-component [47]. Reprinted from Miltat, J.E. and Donahue, M.J. (2007). Numerical Micromagnetics: Finite Difference Methods. In Handbook of Magnetism and Advanced Magnetic Materials. https://doi.org/10.1002/9780470022184.hmm202, with the permission of John Wiley and Sons.

There is another parameter called characteristic length $R_0$, some authors have confused $R_0$ with the exchange length. $R_0$ is defined as the length that is roughly equal to the critical radius of a cylindrical nanostructure below which magnetization reversal occurs by nearly uniform rotation rather than through a nucleation process [46]. Mathematically, Frei et al. defined $R_0 = \frac{\sqrt{A}}{M_s}$ in (cgs), they stated that the ferromagnetic particle critical size is proportional to $R_0$ [48].

Some materials' magnetic properties are provided in Table 1.1. $l_E$ and $R_0$ are calculated in accordance with above mentioned equations, using the available data.

**Table 1.1** Exchange and characteristic lengths of some common ferromagnetic materials

| Material | $A$ (J/m) | $M_s$ (A/m) | $l_E = \sqrt{\frac{2A}{\mu_0 M_s^2}}$ (nm) * $^a$ | $R_0 = \frac{\sqrt{A}}{M_s}$ (nm) * $^b$ | Reference |
|---|---|---|---|---|---|
| Iron | $2.1 \times 10^{-11}$ | $1.7 \times 10^6$ | 3.4 | 8.52 | [48] |
| Nickel | $9 \times 10^{-12}$ | $4.9 \times 10^5$ | 7.72 | 19.36 | [49] |
| Cobalt (hcp) | $3 \times 10^{-11}$ | $1.4 \times 10^6$ | 4.93 | 12.37 | [50] |
| Permalloy $Ni_{80}Fe_{20}$ | $1.3 \times 10^{-11}$ | $8 \times 10^5$ | 5.7 | 14.25 | [51] |
| Permalloy $Ni_{50}Fe_{50}$ | $1.1 \times 10^{-11}$ | $1.11 \times 10^6$ | 3.8 | 9.44 | |

* Calculated in accordance with the given equation.

Notice: The units were converted from $^a$ m to nm, and $^b$ cm to nm

A magnetic vortex state can be obtained in ferromagnetic materials with dimensions less than one micron, several thin film shapes can attain vortex states as their ground

states such as square [52], pentagonal[53], heptagonal [15], elliptical, circular, and triangle [43, 53]. The ground states in circular particles of different diameters and thicknesses were investigated both experimentally and numerically [54–57], and the phase diagram is shown in Fig. 1.11. R and L represent the nanodisc's radius and thickness, respectively. $L_E$ is the exchange length. Three regions are visible in the phase diagram of nanoscale particles separated by the solid lines corresponding to distinct states, which are: (I) Vortex state, (II) in-plane magnetization, and (III) out-of-plane magnetization.

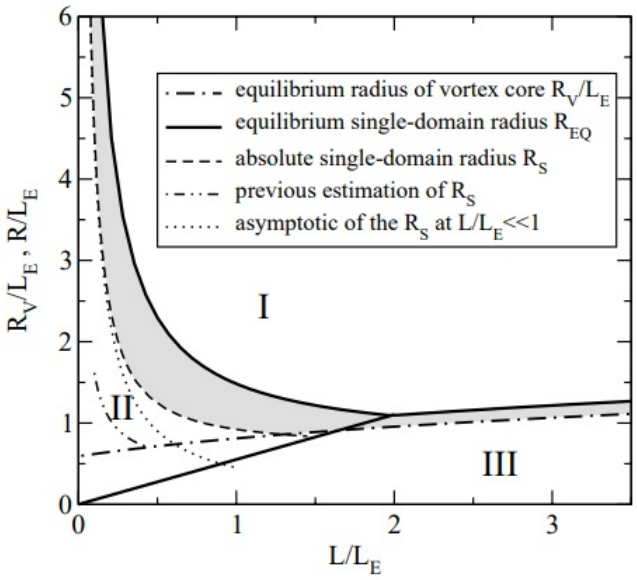


**Figure 1.11** The phase diagram of (I) a vortex state, (II) an in-plane magnetization state, and (III) an out-of-plane magnetization in nanoscale cylinders. The vortex states are metastable in the shaded region [54]. Reprinted from Metlov, K. L., Guslienko, K. Y. (2002). Stability of magnetic vortex in soft magnetic nano-sized circular cylinder. Journal of magnetism and magnetic materials, 242 , 1015–1017. https://doi.org/10.1016/S0304-8853(01)01360-9, Copyright, with permission from Elsevier

Subsequently, Metlov et al. put more effort to elaborate the phase diagram and they did find another energy minimum which appears when the magnetization forms a half-bent C state as shown in Fig. 1.12.

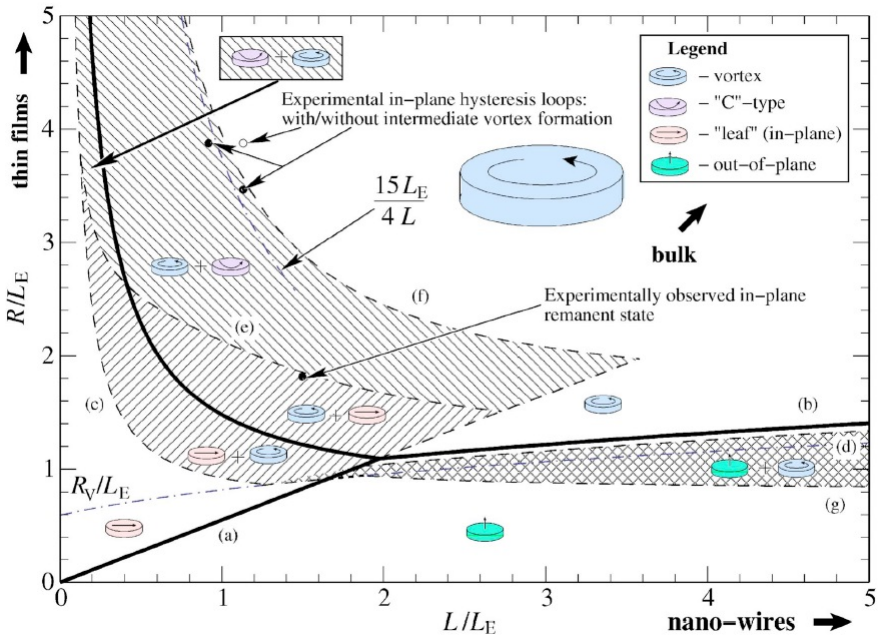


**Figure 1.12** The phase diagram of a vortex state, an in-plane magnetization state, and an out-of-plane magnetization in ferromagnetic nanoscale cylinders. Solid lines represent the boundaries between the ground states. Dashed lines represent the stability loss. The shaded regions can have more than one state (see the symbols with arrows) [58]. Reprinted from Metlov, K. L., Lee, Y. (2008). Map of metastable states for thin circular magnetic nanocylinders. Applied Physics Letters, 92 (11), 112506. https://doi.org/10.1063/1.2898888, with the permission of AIP Publishing.

### 1.3.2 Magnetic Vortex Applications

The fact that nanoscale systems with magnetic vortex states, are more stable at very low dimensions than the single-domain state puts this type of exotic configurations in the list of strong candidates for data storage and logic gates in the future [59–63]. It is clear that the memory function based on the local manipulation of such structures as well as the vortex chirality state clockwise (CW) or counterclockwise (CCW) will also require the readability of this parameter. It was reported in 2005 that the magnetoresistance of a single layer may depend on the chirality state [64]. In a relatively recent study on this subject, it has been reported that, similar to the giant magnetoresistance (GMR) effect, with the double layer approach, "low resistance" in the layers when the vortex chirality states are parallel, and "high resistance" when antiparallel states are observed, and it is stated that this can be a tool for "bit" reading from nanodiscs [7]. The schematic of the main idea in this article is given in Fig. 1.13.

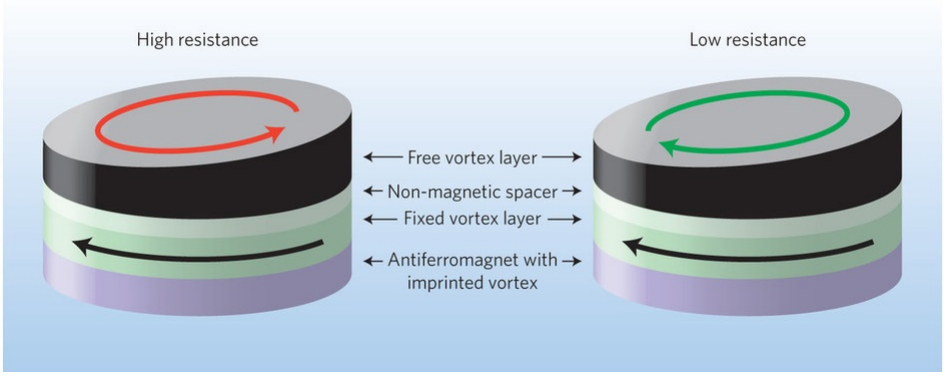


**Figure 1.13** Depending on whether the vortex chirality states of two ferromagnetic layers separated by a non-magnetic layer are the same or opposite, high resistance or low resistance situations arise, which is a way of reading information from these structures. One magnetic layer is "free" while the other is "pinned" and this feature of the fixed layer is due to the presence of an antiferromagnetic layer on top of it. It has been known since the 1980s that antiferromagnetic layers "fix" the magnetism of ferromagnetic thin films. Interestingly, this effect observed in single-domain GMR heads is also observed in magnetic nanodiscs with vortex state [7]. Reprinted from Hertel, R. (2013). Vortex states a la carte. Nature nanotechnology, 8 (5), 318–320. https://doi.org/10.1038/nnano.2013.81, with the permission of Springer Nature.

In traditional GMR, field sensors, recording read heads, and random access memory (RAM), the current that is used to measure the magnetoresistance, is applied in plane along the interfaces of the multilayered structure [65–68]. This method is known as current in plane (CIP). Another method was initially suggested in 1991 [69], in this method the current propagates perpendicular to the planes (CPP), it showed a five times larger GMR effect than previous CIP method. The first CPP-GMR device was reported by Bussmann et al. in 1999 [60]. They synthesized a multilayer structure and the metals sequence for their work was Si/SiN/40 Ta/1500 Cu/7 Ta/20 Cu/(23 NiFeCo/40 Cu/12 NiFe/40 Cu)$_5$/1000 Cu/1500 SiN and the diameter is 0.3 $\mu m$. The current is applied perpendicular to the plane as shown in Fig. 1.14(a). They noticed that there is a significant change in resistance as shown in Fig. 1.14(b), they attributed this change to the switching of the magnetization ordering in the multilayer caused by the coupling between magnetic dipole moments (MDMs) and the curl magnetic field generated by the current flowing through this multilayer. They reached a conclusion that the magnetic layer attains a vortex state, and if the magnetic layers acquire the same vortex states a low resistance state will be obtained. On the other hand, when these vortices have different states a high resistance state will be obtained. One of the first studies to examine the resistive behavior of magnetic vortices in submicron solids was Vavassori et al. [64]. In this study, which examines the magnetic direction-dependent resistance change along the plane in 1 $\mu m$ PY disc in the presence of an applied magnetic field, they found that

there is voltage drop when a vortex state evolves (See Fig. 1.15) and this voltage drop can determine the chirality state either CW or CCW. Therefore, magnetoresistance can be utilized to determine the vortex chirality state, thus, improving the chances that an array with magnetic vortices can be used in data storage technology.

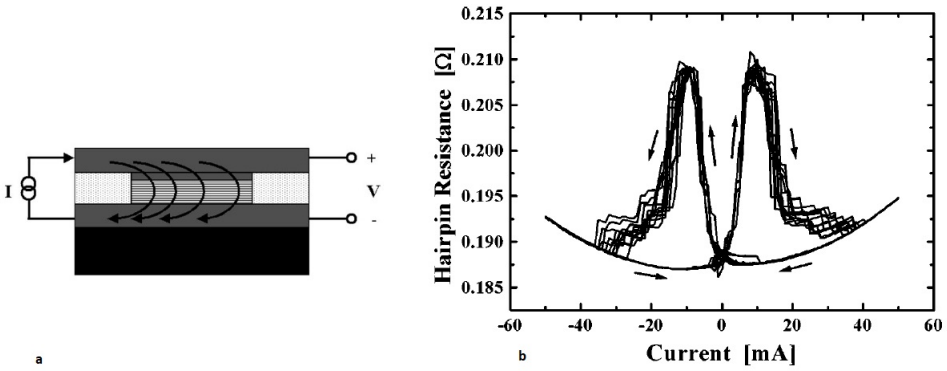


**Figure 1.14** (a) A schematic illustrates how to measure the resistance. (b) Resistance of the multilayer of 0.3 $\mu$m diameter [60]. Reprinted from Bussmann, K., Prinz, G., Cheng, S.-F., Wang, D. (1999). Switching of vertical giant magnetoresistance devices by current through the device. Applied physics letters, 75 (16), 2476–2478. https://doi.org/10.1063/1.125053, with the permission of AIP Publishing.

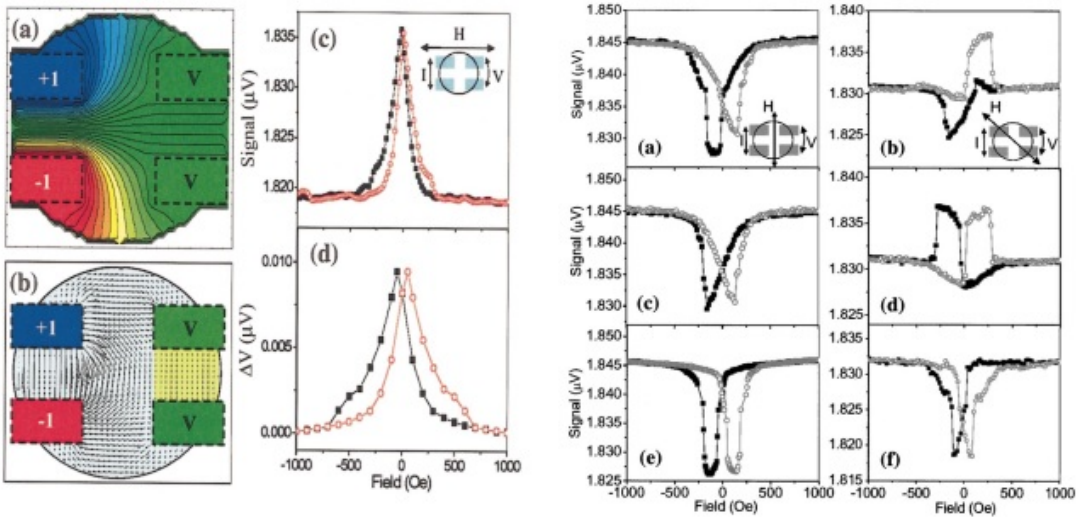


**Figure 1.15** Left: Simulation and experimental results of the resistance of the magnetic vortex in the terminal structure. (c) Measured and (d) calculated voltage drops across terminals 1 and 2 for H along the x direction. Right: Experimentally obtained inter-terminal voltage drop results from the same structure. They are given for different H combinations and different magnetic histories (See Ref. [64] for details). Reprinted from Vavassori, P., Grimsditch, M., Metlushko, V., Zaluzec, N., Ilic, B. (2005). Magnetoresistance of single magnetic vortices. Applied Physics Letters, 86 (7), 072507. https://doi.org/10.1063/1.1866212, with the permission of AIP Publishing.

Another promising application is to use a magnetic vortex state in radio frequency oscillators, which is the working principle for many modern technologies, such as satellites, radar, and cell phones. Nanostructures, high thermal stability, low phase noise, and broadband tunable oscillators are essential properties for the aforementioned applications. A potential candidate to substitute radio frequency oscillators is a spin transfer torque based nano device [70].

Nanomagnetic structures are also promising candidates in biomedicine. A scientific effort is well spent on promoting new methods to use these structures in different disciplines within this scope. There are two main reasons to drive this research: First, the nanoscale magnetic structures can easily interact with biological systems (e.g. cells). Second, these nanostructures could be simply manipulated by applying a magnetic field remotely. These features promote a wide range of biomedical applications, such as drug delivery, MRI, etc [71]. Although these are only four of the considerable biomedical applications of magnetic nanostructures that are presently being searched.

Torrejon et al. [72], have experimentally demonstrated that a nanoscale vortex-based spin torque oscillator (a magnetic tunnel junction that has magnetic vortex ground states) can be used to achieve neuromorphic computing. The neural inputs are encoded in the time-dependent current that is injected into the magnetic tunnel junction, the injected current exerts a torque on magnetic moments. Which results in oscillations, and their amplitudes are robust to noise. Furthermore, the amplitude of an oscillation is substantially nonlinear as a function of the input current and is based intrinsically on former inputs, therefore, the nanodevice combines the two most conclusive properties of neurons—nonlinearity and memory. They utilize a microwave diode to detect and measure the dynamics of the amplitude of the oscillations. Finally, they use these oscillation amplitudes as the neural output.

Recently, a magnetic vortex was proposed as a building block for a robust sensor application that can be used in a wide range of applications[73]. The main idea is to employ vortex dynamics under the effect of the field as a sensor response. When applying a magnetic field, the magnetic moments try to align parallel with the external field direction and the field results in vortex core displacement away from the symmetry center. It will push the vortex core toward the edge until the core is annihilated. The formed state is a nearly single-domain state and the magnetic moments align with the field direction. If the external field is removed, the vortex state is reformed to minimize the total system energy. Guslienko et al. have proposed a model (rigid vortex model) to estimate the annihilation field (the field required to annihilate a vortex core), nucleation field (the field required to form a vortex

core), and the initial susceptibility of magnetic vortex state[51], which are important properties for sensor applications.

The fabrication of ferromagnets of different disc-shaped nanostructures while maintaining a well-defined magnetic vortex state for various applications imposes challenges. There are two main methods to produce magnetic nanoparticles, chemical synthesis methods (bottom-up fabrication: construct bulk structures from atoms and molecules), and physical methods (top-down fabrication: shape a microstructure from a bulk material with specific size and features) [74]. Usually, the chemical synthesis methods produce spherical particles, they are hard to employ for fabricating multilayer structures with anisotropic shapes. However, chemical synthesis methods, require inexpensive equipment and have large application coverage, hence, these methods can generate an appreciable production yield. Nanosphere lithography (NSL) is one of these methods, this method employs polystyrene spheres as a mold to fabricate nanostructures [75]. This method has a drawback that imposes a limitation on its applications, it is hard to distribute the monolayers over a large area, they accumulate on some surfaces and other empty surfaces appear. Sparse colloidal lithography (SCL) is another approach, that is employing charged spheres that are well separated and arranged over the surface due to the effect of Coulomb force. This method improves the overall production of nanostructures of different shapes [76]. Hole-mask colloidal lithography (HCL) was presented as a development of SCL to increase the usage of the method, and it can combine new materials and fabricate different nanostructures [77]. Goiriena et al. have fabricated Permalloy nanodiscs using HCL with aspect ratios that fill in the vortex state region[75]. They were able to fabricate nanodiscs with average radii of 30 $nm$ and thickness ranging from 20 to 50 $nm$, which indicates that the HCL technique imposes a great degree of control over dimensions. To summarize the fabrication steps: (1) silicon wafers were used with silicon dioxide on top as substrate and polymethyl methacrylate is deposited onto the substrate (See Fig. 1.16(1)), the polystyrene nanospheres distributed sparsely on the surface because of the electrostatic interactions (2-3), (4) A thin layer of titanium is deposited on top in the polymeric layer to etch the holes, (5) the removal of the polystyrene nanospheres by peeling off with a pressure-sensitive adhesive tape, (6) oxygen plasma is used to etch the non-protected polymethyl methacrylate layer, (7) Permalloy with composition $Ni_80Fe_20$ is sputtered, and (8) lastly, acetone is used to detach the polymethyl methacrylate, the titanium is lifted off, eventually, an array of permalloy nanodiscs distributed on a silicon substrate is obtained [75].

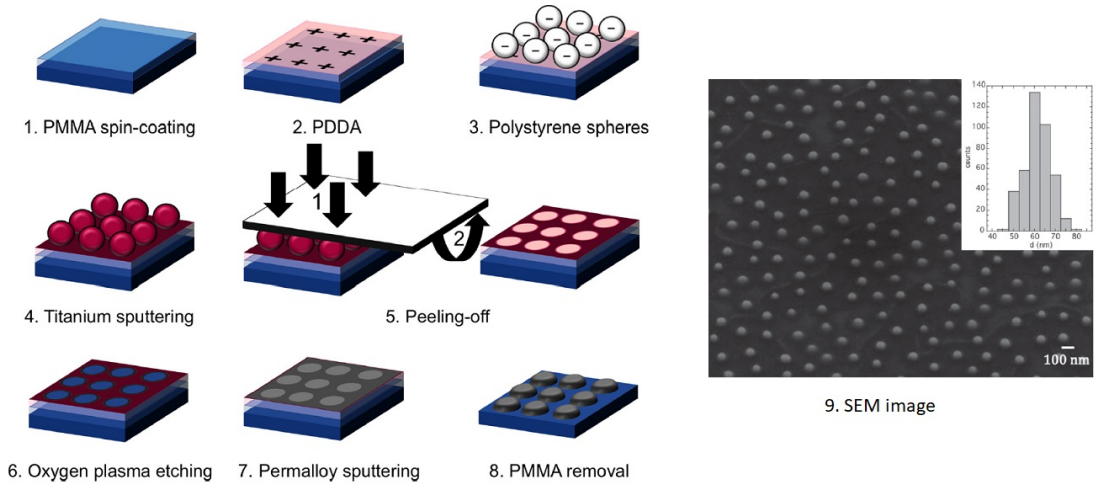


**Figure 1.16** (1-8) A schematic illustrates the fabricating PY nanodiscs by HCL, (9) SEM image of the PY nanodiscs prepared with average thicknesses of 50 *nm* and average radii of 30 *nm* [75]. Reprinted from Goiriena-Goikoetxea, M., García-Arribas, A., Rouco, M., Svalov, A., Barandiaran, J. (2016). High-yield fabrication of 60 nm permalloy nanodiscs in well-defined magnetic vortex state for biomedical applications. Nanotechnology, 27 (17), 175302. DOI 10.1088/0957-4484/27/17/175302, with the permission of IOP.

On the other side, physical methods allow the fabrication of different magnetic structures in terms of shape, size, and composition with precisely controlled magnetic properties, which promotes these methods for a wide range of applications of magnetic-based nanostructures. Among these methods are photolithography, electron-beam lithography (EBL), interference lithography, and nanoimprint lithography. The microdiscs patterned as an array usually are fabricated by conventional photolithography. On the other hand, EBL is a widely used method at smaller scales, and usually, this method is employed to study the extreme properties of the nanostructures [33, 78–80]. The EBL method is capable of small area processing. This disadvantage limits its use in applications that require massive production. Currently, deep-UV lithography is employed for microelectronic fabrication in the industry and that is due to its capability to achieve massive production but it is often not available for investigation purposes because of the expensive equipment. Further, it is likely the most preferable technique for nanofabrication.

The first experiments on vortex observation were reported in Refs. [33, 78], the samples in Shinjo's experiment were fabricated by means of EBL and evaporated in an ultrahigh vacuum utilizing an electron-beam gun. The array of permalloy nanodiscs (See Fig. 3 in Ref. [33]) were patterned on thermally oxidized Si substrates capped by a layer of resist. The resist is extracted by a lift-off process, and permalloy nanodiscs with different diameters reside on top of the Si surface. Cowburn et al. have shown that EBL can be employed to produce nanodiscs in the array that are

substantially similar to each other (See Fig. 1.17(A)), so one can presume that the average properties for the array can also be considered as the properties of a single nanomagnet [78]. Furthermore, they have presented the magnetic behavior of a soft magnetic alloy (Supermalloy) as a function of both diameter and thickness. Also, they were able to distinguish two specific states, a vortex state, and a single-domain state during the measurement of hysteresis loops under the effect of an external magnetic field (See Fig. 1.17(B)).

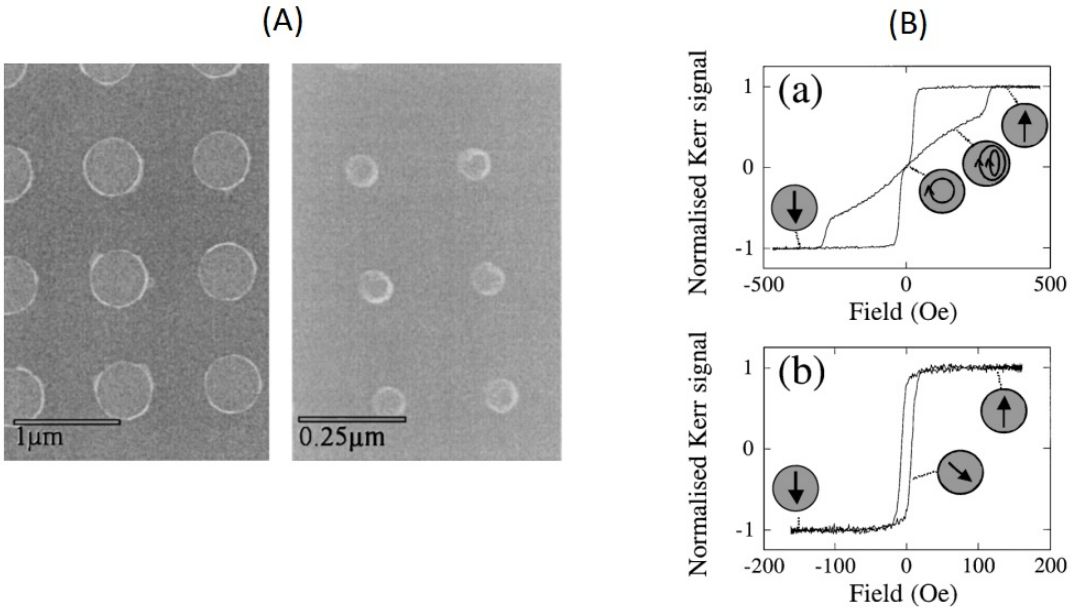


**Figure 1.17** (A) SEM images of circular Supermalloy nanodiscs of diameter 500 nm (left) and 55 nm (right), (B) Hysteresis loops measured for different aspect ratios: (a) t = 10 *nm*, d = 300 *nm*, (b) t = 10 *nm*, d = 100 *nm* [78]. Reprinted with permission from Cowburn, R. P., Koltsov, D., Adeyeye, A., Welland, M., Tricker, D. (1999). Single-domain circular nanomagnets. Physical Review Letters, 83 (5), 1042. https://doi.org/10.1103/PhysRevLett.83.1042. copyright (1999) by the American Physical Society

## 1.4 State of Art

Despite the potential of tailoring vortex states for a wide range of applications, few works have focused on the chirality reversal of these exotic states both theoretically and experimentally [81–85]. The main challenge is how to realize fast and repeatable manipulation of magnetism in these exotic states and obtain chirality, polarity, or both states reversal within a few nanoseconds. Usually, in bulk the vortex state is

unstable: The produced stability maps show the importance of the aspect ratios (radius/thickness) and geometry to obtain stable vortex states in reduced dimensions [55, 58, 78, 86, 87]. The different ferromagnetic states discussed in Section 1.2.2 show that a disc should have a specific radius/thickness ratio to acquire a vortex state. The degenerate states CW and CCW may appear randomly as ground states especially if there is no shape anisotropy [43, 53]. Few works have focused on inducing vortex state reversal in shape-wise anisotropic systems [15, 53, 88–90]. Vargas et al. have investigated the magnetic properties of asymmetric ferromagnetic dots using Monte Carlo simulations, and they reported shape asymmetry effects on the coercivity (Hc), remanence (Mr), and barrier for vortex and C-state formation [88]. They have shown that a dot with a small asymmetric geometry affects the hysteresis curves by lowering both the coercivity and remanence. Increasing the asymmetry of a dot leads to almost square hysteresis loops and the coercivity and remanence change as a function of the asymmetric parameter. Also, the geometry affects the stability of the C state and the vortex state. It determines the zone of vortex nucleation and annihilation during magnetization reversal.

Schneider et al. have investigated the magnetic switching of a single vortex in a permalloy element with a slight geometric asymmetry [89]. They explain the process of a chirality reversal in a magnetic vortex state as follows: The demagnetization field forces the magnetic moments to align parallel with the disc edges to avoid magnetic pole formation. Since the disc is asymmetric with a long curved edge and a short flat edge, a preferred orientation of the magnetization ordering is obtained by the peripheral spins (See Fig. 1.18), and exchange interaction forces the spins closer to the center to form a vortex state. Utilizing asymmetric nanodisc, one can reverse the chirality state of a vortex by applying an in-plane magnetic field parallel to the flat edge to obtain CW or CCW vortex configuration. Kimura et al. [90], confirm such results by the mean of micromagnetic simulation (See Fig. 1.19(a)), after the application of a magnetic field a CW vortex state form in disc A and CCW vortex state form in disc B (See Fig. 1.19(b)). Also, they investigated the dynamics of a vortex core in an asymmetric disc by applying an in-plane magnetic field that is perpendicular to the short flat edge as illustrated in Fig. 1.19(b) and (c). Inward vortex motion was induced by applying a positive magnetic field $H_{hor}$ as shown in Fig. 1.19(b), and Outward vortex motion was induced by applying a negative magnetic field. Producing such asymmetric magnetic nanodiscs requires precise adjustments and additional processes at reduced dimensions or the magnetic vortex state cannot be realized.

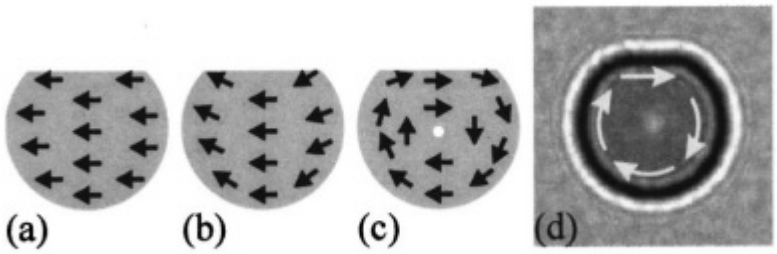


**Figure 1.18** Model for the evolution of the vortex: (a) A saturated state. (b) The spins at the element edge align parallel to the edge (c) determining the sense of magnetization rotation, (d) underfocused Fresnel image shows the vortex state with CW chirality [89]. Reprinted from Schneider, M., Hoffmann, H., Zweck, J. (2001). Magnetic switching of single vortex permalloy elements. Applied Physics Letters, 79 (19), 3113–3115. https://doi.org/10.1063/1.1410873, with the permission of AIP Publishing.

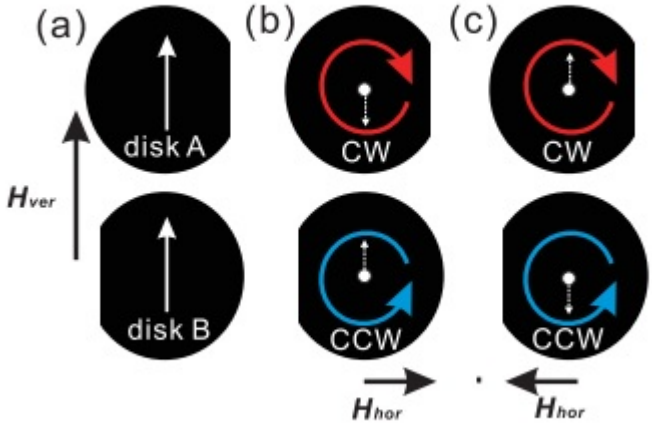


**Figure 1.19** (a) Applying a magnetic field parallel to the flat edge of the disc to form magnetic vortices with opposite chirality. The chiralities of disk A and disk B are CW and CCW, respectively. b) Applying a positive magnetic field perpendicular to the short flat edge of the disc to induce inward vortex motion. (c) Applying a negative magnetic field to induce outward vortex motion [90]. Reprinted from Kimura, T., Otani, Y., Masaki, H., Ishida, T., Antos, R., Shibata, J. (2007). Vortex motion in chilarity-controlled pair of magnetic disks. Applied Physics Letters, 90 (13), 132501. https://doi.org/10.1063/1.2716861, with the permission of AIP Publishing.

A vortex polarity is another parameter that describes the magnetization vector along the normal to the plane inside the vortex core either up or down. To control the polarity, different methods were proposed such as bursts of magnetic fields, rotat-

ing magnetic fields, microwave, spin-polarized currents, and optical manipulation [61, 63, 91–94]. Loubens et al. have investigated the gyration motion of the magnetic vortex core after applying a perpendicular magnetic field $B_\perp$ that was varied in wide range values from positive (parallel to the vortex polarity) to negative (antiparallel to the vortex polarity) [63]. They have reported the existence of two stable gyrotropic modes of the magnetic vortex core that can be generated under a certain range of the applied $B_\perp$ field. These two modes have a different opposite circular rotation with different frequencies and correspond to opposite directions of vortex core polarity relative to the direction of the applied $B_\perp$ field. Hertel et al. have reported a method to control vortex polarity by applying ultrashort unipolar magnetic field $B_\parallel$ pulses parallel to a ferromagnetic permalloy nanodisc utilizing micromagnetic simulations[92]. They have claimed that the switching of magnetic vortex polarity does not require matching the comparatively slow gyrotropic resonance frequency. They induce vortex polarity switching by applying nonresonant, and very short field $B_\parallel$ pulse (below 100 ps) of moderate strength (80 mT). In their study, the polarity switching occurs through a sequence of events: (i) vortex-antivortex pair creation, (ii) after that an annihilation process occurs. In consequence, a single vortex with opposite polarity is obtained. This process requires a specific combination of pulse strength and pulse width, otherwise, multiple switches, no reversal, and/or vortex annihilation. One or more of these events could take place. Kravchuk et al. have proposed a method to control the polarity of an immobile magnetic vortex which is pinned by a highly anisotropic easy-axis impurity at the disc center by applying a rotating magnetic field[93]. Inside the impurity, the magnetization is fixed perpendicularly to the disc plane because of the force exerted by the anisotropy field. The initial polarity state is $p = +1$. They apply an ac magnetic field that rotates against the vortex polarity. They summarize the switching process in three steps: (a) Formation of localized area with considerable out-of-plane magnetization, (b) a vortex–antivortex pair is created within this localized area after the out-of-plane magnetization reaches its maximum value, (c) the newly created antivortex annihilates with pinned original vortex yields in switching the polarity of the original vortex and $p = -1$ is obtained.

Kammerer et al. have presented experiments that confirm that vortex polarity switching can be realized by applying in-plane rotating magnetic fields [94]. These fields induce spin wave excitation. They formulate selection rules for different spin wave excitation modes and compare their results to that of Kravchuk et al [93]. Kravchuk et al have examined only one mode. On the other hand, Kammerer et al. have demonstrated by the means of micromagnetic simulations and experiments that the vortex core dynamic is important and describes the different spin wave modes

observed in the vortex polarity reversal [94]. They have shown that the different sets of azimuthal mode number and vortex polarity affect the dynamics remarkably, and they attributed these effects to the superposition of spin-wave amplitude with the gyrofield. Also, they noticed a vortex–antivortex pair creation during the reversal process, during which the newly created pair stay near the disc core. This process is followed by the subsequent annihilation of the newly created vortex–antivortex pair, the dynamical distortion of the original vortex is the source of the newly created pair. It forms a localized region with considerable out-of-plane magnetization near the moving vortex core. Guslienko et al. [62] explained this localized region formation by an effective field which is proportional to the critical vortex core velocity. A critical core velocity of approximately 320 $m/s$ in permalloy was reported.

Pigeau et al. [95], have demonstrated a method to control vortex polarity by single- and double-microwave pulse sequences. They apply a bias perpendicular magnetic field to distinguish the two different polarity states. The external field is almost five times weaker than the static field required to switch the polarity, consequently, this weak external field would not impose a great asymmetry between the two polarity states during the switching process. They use microwave power to manipulate the polarity state and read the polarity state with a magnetic resonance force microscope (MRFM). The power of the MRFM is weak enough, so it would not alter the core polarity during the reading sequence.

Yamada et al. [6], have demonstrated the control of the vortex polarity by using a polarized current. The current imposes a torque on the vortex core through the effect of spin-transfer, it enlarges the diameter of the circular trajectory of the vortex core during gyration. The damping force tries to stabilize the gyration, therefore, a steady motion is preserved. The high speed vortex gyration generates a robust dynamic field which reverse the vortex polarity.

Lee et al. [96], have reported a new method to switch vortex polarity, which is called edge-soliton-mediated vortex core reversal. This mechanism differs from the mentioned above switching processes driven by the creation and annihilation of vortex-antivortex pairs in terms of the accompanying topological defects, energy barriers, and spin-wave emissions. They found that in ferromagnetic nanodiscs with small diameters when a dc current flows perpendicular to the nanodisc sample, it would produce two different effects: spin transfer torque (STT), and in-plane magnetic Oersted field. These two effects exert a force on the vortex core and push it towards the nanodisc edge, the vortex core transforms into coupled edge solitons but this pair is merged by a fusion process and an opposite polarity is obtained. Finally, the vortex polarity switching is obtained through the splitting into two edge-

soliton pair and fusion of this pair, rather than the well known vortex-antivortex pair excitation mechanism reported in Refs [6, 62, 92–94]

Choi et al. have reported a method to manipulate vortex chirality and polarity simultaneously via applying a current along the disc normal, which induces an Oersted field, and spin transfer torque effect [97]. Luo et al. have proposed an alternative edge-solitons-mediated method to control both vortex chirality and polarity [85]. The edge solitons act differently with varied current density, in consequence, during the reversal processes S state or C state can be formed. Therefore, starting from a random state one can obtain any of the four degenerated vortex states by current pulses.

A vortex state can be manipulated via surface probing methods using a magnetic tip [6], but this can only be done in a laboratory. Experimentally, manipulation of the polarity state possesses challenges, due to the spatial oscillation of magnetic moments and there are a limited number of attempts made to control polarity [43].

# 2. Theory

## 2.1 The Landau–Lifshitz–Gilbert (LLG) equation

The first mathematical equation of time-dependent motion of uncoupled and undamped MDMs was reported by Bloch [98]. In 1935, Landau and Lifshitz [99] formulate an equation to describe the dynamics of the magnetic dipoles in a ferromagnetic [100]. The following equation is used only to describe small damping case:

$$\frac{d\mathbf{M}}{dt} = -\gamma(\mathbf{M} \times \mathbf{H_{eff}}) - \gamma\frac{\lambda}{M_s}(\mathbf{M} \times (\mathbf{M} \times \mathbf{H_{eff}})) \tag{2.1}$$

Where $\mathbf{M} = (\mathbf{M_x}, \mathbf{M_y}, \mathbf{M_z})$ is the magnetization vector, $M_s$ is the saturation magnetization, $\gamma = g|e|/2m_e$ is the gyromagnetic ratio, where $g$ is the g-factor, $e$ and $m_e$ are the electron charge and mass, respectively. $\lambda$ is a phenomenological damping parameter, $\mathbf{H_{eff}}$ is the effective field which includes the external and the internal fields. The first term $-\gamma(\mathbf{M} \times \mathbf{H_{eff}})$ in Eq. 2.1 is the precession of magnetization which describes the interaction between $\mathbf{H_{eff}}$ and local spin. This term can be easily obtained from the classical mechanical equation [98]:

$$\frac{d\mathbf{P}}{dt} = \mathbf{L} \tag{2.2}$$

where $\mathbf{P} = \frac{\mathbf{J_m}}{\gamma}$ is the angular momentum of a rigid body, $\mathbf{J_m}$ is the magnetic polarization, $\mathbf{L}$ is the torque applied, and substituting the magnetic torque $\mathbf{L} = (\mathbf{J} \times \mathbf{H_{eff}})$, Eq. 2.2 becomes:

$$\frac{d\mathbf{J_m}}{dt} = -\gamma(\mathbf{J_m} \times \mathbf{H_{eff}}) \tag{2.3}$$

By dividing Eq. 2.3 by the vacuum permeability $\mu_0$, the equation is transformed to first term in Eq. 2.1 which describes the undamped precession of the magnetization, Fig. 2.1(a) depicts the undamped precession motion:

$$\frac{d\mathbf{M}}{dt} = -\gamma(\mathbf{M} \times \mathbf{H_{eff}}) \tag{2.4}$$

The second term $-\gamma\frac{\lambda}{M_s}(\mathbf{M} \times (\mathbf{M} \times \mathbf{H_{eff}}))$ describes the damping of the precessional motion which forces the magnetization to align with the $\mathbf{H_{eff}}$ vector, as shown in Fig. 2.1. This term was chosen based on purely phenomenological reasons

summarized as follows: First, the damping process should minimize the total energy of the magnetic system and form a stable magnetization state. Second, the magnetization magnitude **M** should stay fixed.

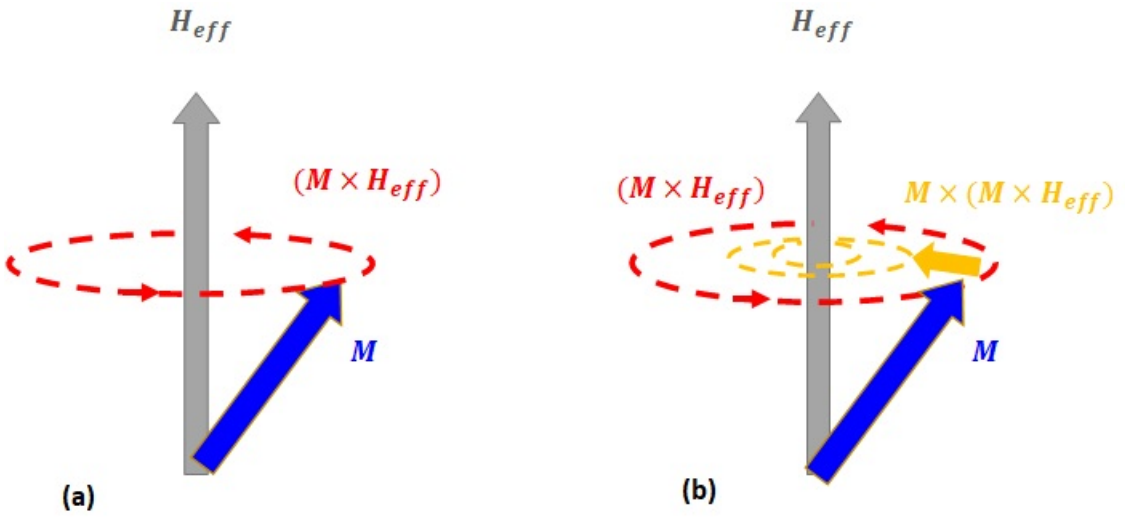


**Figure 2.1** The magnetization precession for (a) undamped motion and (b) damping of the precessional motion.

In 1955, Gilbert proposed a modification on Eq. 2.1, to describe the strong damping cases in the reduced dimensions[101]:

$$\frac{d\mathbf{M}}{dt} = -\gamma(\mathbf{M} \times (\mathbf{H_{eff}} - \frac{\alpha}{\gamma M_s}\frac{d\mathbf{M}}{dt})) \tag{2.5}$$

where $\alpha$ is the Gilbert damping parameter. Using algebraic manipulations, Eq. 2.5 converted into its open form:

$$\frac{d\mathbf{M}}{dt} = -\frac{\gamma}{1+\alpha^2}(\mathbf{M} \times \mathbf{H_{eff}}) - \frac{\gamma}{1+\alpha^2}\frac{\alpha}{M_s}(\mathbf{M} \times (\mathbf{M} \times \mathbf{H_{eff}})) \tag{2.6}$$

This is Landau-Lifshitz-Gilbert (LLG) equation. Eqn. 2.6 has the same form of Eqn. 2.1 with $\gamma/(1+\alpha^2)$ replacing $\gamma$ and $\alpha$ replacing $\lambda$. Usually, Eq. 2.6 is divided by $M_s$. This yield $m = M/M_s$, here $m$ is the unit vector of the magnetization, which gives us:

$$\frac{d\mathbf{m}}{dt} = -\frac{\gamma}{1+\alpha^2}(\mathbf{m} \times \mathbf{H_{eff}}) - \frac{\gamma}{1+\alpha^2}\frac{\alpha}{M_s}(\mathbf{m} \times (\mathbf{m} \times \mathbf{H_{eff}})) \tag{2.7}$$

A more general version of the LLG equation is the Landau-Lifshitz-Gilbert-Slonczewski (LLGS) equation, where the Slonczewski's spin transfer torque term $\tau_{\mathbf{STT}}$ is added to Eqn. 2.6, this effect is included only when a spin polarized current is passing through a magnetic system. This current then would induce a torque to align the magnetic moments with the current spin polarization direction. Eqn. 2.6 becomes [102]:

$$\frac{d\mathbf{M}}{dt} = -\gamma'(\mathbf{M} \times \mathbf{H_{eff}}) - \gamma' \frac{\alpha}{M_s}(\mathbf{M} \times (\mathbf{M} \times \mathbf{H_{eff}})) + \tau_{\mathbf{STT}} \tag{2.8}$$

Where $\gamma' = \gamma/(1+\alpha^2)$, $\tau_{\mathbf{STT}} = (a_{STT}/M_s)\ (\mathbf{M} \times (\mathbf{M} \times \hat{\mathbf{m}}_{\mathbf{p}}))$, where $a_{STT} = \hbar\gamma PJ/(2\mu_0 M_s eL)$, $\hat{m}_p$ is the unit vector of the spin polarization direction, $\hbar$ is the reduced Planck's constant, $J$ is the current density, $e$ is the electron charge, $L$ is the free layer thickness in meters, $P$ is the degree of spin polarization.

## 2.2 Effective Magnetic Field and Energy Terms in LLG Equation

$\mathbf{H_{eff}}$ is derived from the magnetic energy density, $\xi$ [47]:

$$\mathbf{H_{eff}} = -\frac{\partial \xi}{\mu_0 \partial \mathbf{M}} = \mathbf{H_{demag}} + \mathbf{H_{ani}} + \mathbf{H_{exch}} + \mathbf{H_{Zeeman}} + \mathbf{H_{current}} + \mathbf{H_{th}} \tag{2.9}$$

Where $\mathbf{H_{demag}}$ is the demagnetization field, $\mathbf{H_{ani}}$ is the magnetocrystalline anisotropy field, $\mathbf{H_{exch}}$ is the exchange field, $\mathbf{H_{Zeeman}}$ is the external magnetic field and $\mathbf{H_{th}}$ is the thermal field.

### 2.2.1 Demagnetization field and energy

The demagnetization field $\mathbf{H_{demag}}$ is in charge of forming domain structure in magnetic film, therefore, it contributes the most to the effective magnetic field $\mathbf{H_{eff}}$. $\mathbf{H_{demag}}$ arises from surface $\sigma_s$ and volume charges $\rho_v$ in resemblance with electrostatics [47, 103].

$$\begin{aligned} \sigma_s &= \mu_0 M_s(\mathbf{m}\cdot\mathbf{n}) \\ \rho_v &= -\mu_0 M_s(\nabla\cdot\mathbf{m}) \end{aligned} \tag{2.10}$$

And the gradient of the scalar potential $\Phi_d$ can be used to express the demagnetization field, $\mathbf{H_{demag}}$ can be written as:

$$\mathbf{H_{demag}}(\mathbf{r}) = -\nabla\Phi_d(\mathbf{r}) \tag{2.11}$$

$$\Phi_d(\mathbf{r}) = \frac{1}{4\pi\mu_0}\left(\int_v \frac{\rho_v(\mathbf{r}')}{|\mathbf{r}-\mathbf{r}'|}d^3\mathbf{r}' + \int_s \frac{\sigma_s(\mathbf{r}')}{|\mathbf{r}-\mathbf{r}'|}d^2\mathbf{r}'\right) \tag{2.12}$$

The geometrical relations between the vectors in Eq. 2.12 is shown in Fig. 2.2

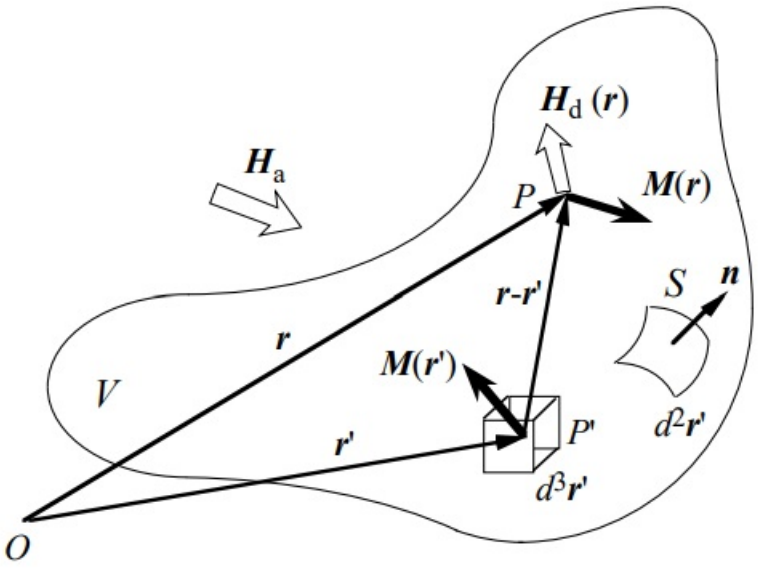


**Figure 2.2** Geometry attached to Eq. 2.12 [47]. Reprinted from Miltat, J.E. and Donahue, M.J. (2007). Numerical Micromagnetics: Finite Difference Methods. In Handbook of Magnetism and Advanced Magnetic Materials. https://doi.org/10.1002/9780470022184.hmm202, with the permission of John Wiley and Sons.

From Eqs. 2.11 and 2.12, the $\mathbf{H_{demag}}$ becomes as follow:

$$\mathbf{H_{demag}}(\mathbf{r}) = \frac{1}{4\pi\mu_0}\left(\int_v \frac{(\mathbf{r}-\mathbf{r}')\ \rho_v(\mathbf{r}')}{|\mathbf{r}-\mathbf{r}'|^3}d^3\mathbf{r}' + \int_s \frac{(\mathbf{r}-\mathbf{r}')\ \sigma_s(\mathbf{r}')}{|\mathbf{r}-\mathbf{r}'|^3}d^2\mathbf{r}'\right) \tag{2.13}$$

There are four important points we should consider here. First, considering the dipolar nature of magnetism, the charges must add up to zero. Second, in an easily magnetized material, the demagnetization term dominates the other energy terms, this leads to the pole avoidance principle which is the only way to minimize energy. This denote that the magnetization most likely will align parallel to the external surfaces and the formed state will satisfy $\nabla \cdot \mathbf{m} = \mathbf{0}$ in the bulk. Obviously, this can be possible at the cost of anisotropy and exchange terms when exist. Third, the long range dipolar interactions in demagnetization energy leads to major errors when truncation of the integrals is used. Finally, computing of demagnetization field is the most time-consuming part of micromagnetic simulation, however, in numerical computation, using Fast Fourier Transforms shortens the time consumed [47].

Another way to obtain $\mathbf{H_{demag}}$ is to take into account dipole-dipole interaction of magnetization in the considered sample [104, 105].

$$\mathbf{H_{demag}}(\mathbf{r})_i = \frac{1}{4\pi} \sum_j \int \frac{3\ \mathbf{r}(i)\mathbf{r}(j) - \delta_{ij}}{|\mathbf{r} - \mathbf{r}'|^3}\ \mathbf{M}_j(\mathbf{r}') d^3\mathbf{r}' \tag{2.14}$$

$$\begin{aligned} \mathbf{r}(i) &= \frac{\mathbf{r}(i) - \mathbf{r}'(i)}{|\mathbf{r} - \mathbf{r}'|} \\ \mathbf{r}(j) &= \frac{\mathbf{r}(j) - \mathbf{r}'(j)}{|\mathbf{r} - \mathbf{r}'|} \end{aligned} \tag{2.15}$$

Where , $i, j = x, y, z$ are vector component. The demagnetization energy density can be estimated from the following equation:

$$\xi_{demag} = -\frac{1}{s} \mu_0 M_s (\mathbf{H_{demag}} \cdot \mathbf{m}) \tag{2.16}$$

In order to numerically estimate the demagnetization field at point r, the magnetic structure is discretized into cells *index* $(i', j', k')$ with saturation magnetization and constant charge density in the tiles *index* $(l', m', n')$ of the boundaries as shown in Fig. 2.3.

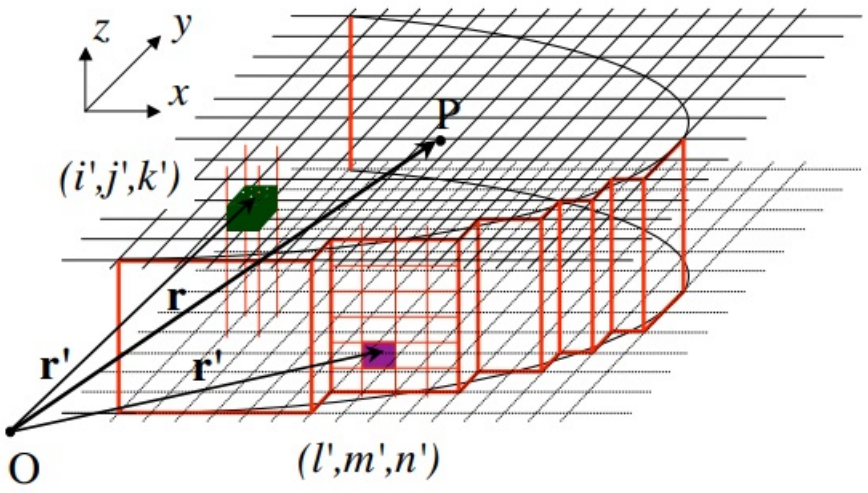


**Figure 2.3** The demagnetization field at point P(r) arising from the magnetization divergence in the volume cells and charge density in the surface tiles. The black lines describe the bottom and top surfaces, and the continuous edge. The red stair-like boundary is the numerical rim boundary [47]. Reprinted from Miltat, J.E. and Donahue, M.J. (2007). Numerical Micromagnetics: Finite Difference Methods. In Handbook of Magnetism and Advanced Magnetic Materials. https://doi.org/10.1002/9780470022184.hmm202, with the permission of John Wiley and Sons.

To estimate the demagnetizing field at point $(i,j,k)$ and vector $\mathbf{r}$ from the origin, Eqn. 2.13 is reduced with a finite sum to following form:

$$\mathbf{H_{demag}}(\mathbf{r}) = \frac{1}{4\pi\mu_0} \sum_{i',j',k'} \left[ \rho_v(i',j',k') \int_{v'(i',j',k')} \frac{(\mathbf{r}-\mathbf{r}')}{|\mathbf{r}-\mathbf{r}'|^3} d^3\mathbf{r}' \right] + \frac{1}{4\pi\mu_0} \sum_{l',m',n'} \left[ \sigma_s(i',j',k') \int_{s'(l',m',n')} \frac{(\mathbf{r}-\mathbf{r}')}{|\mathbf{r}-\mathbf{r}'|^3} d^2\mathbf{r}' \right] \tag{2.17}$$

In Eqn. 2.17, the integrals require to be estimated once because they are reduced to geometrical coefficients.

$$\mathbf{H_{demag}}(\mathbf{r}) = \frac{1}{4\pi\mu_0} \sum_{i',j',k'} \left[ \rho_v(i',j',k') \; C_v(i,j,k,i',j',k') \right] + \frac{1}{4\pi\mu_0} \sum_{l',m',n'} \left[ \sigma_s(l',m',n') \; C_s(i,j,k,l',m',n') \right] \tag{2.18}$$

To achieve this decomposition, one should consider the magnetization as function of the coordinates x,y,z within the magnetic bulk and constant over the surface in the tile, this function is called trilinear, which is a method of multivariate interpolation on a 3-dimensional regular grid. In that case all the coefficients $C_v$ and $C_s$ are definite integrals. For example, the demagnetization field (x-component) contribution from a volume cell is given as follow:

$$C_v^x = \int_{x_1'}^{x_2'} \int_{y_1'}^{y_2'} \int_{z_1'}^{z_2'} \frac{x - x'}{|\mathbf{r} - \mathbf{r}'|^3} dx' dy' dz' \tag{2.19}$$

In the same way, the demagnetization field (z-component) contribution from a tile parallel to the xy plane is provided as:

$$C_{sxy}^z = \int_{x_1'}^{x_2'} \int_{y_1'}^{y_2'} \frac{z - z'}{|\mathbf{r} - \mathbf{r}'|^3} dx' dy' \tag{2.20}$$

The demagnetization energy density of a single computational cell can be obtained from the following equation:

$$\xi_{demag}(i,j,k) = -\frac{1}{s} \mu_0 M_s (\mathbf{H_{demag}}(i,j,k) \cdot \mathbf{m}(i,j,k)) \tag{2.21}$$

### 2.2.2 Exchange field and energy

In ferromagnetic materials, the exchange interaction forces the MDMs of the neighboring atoms to align in the same direction. The exchange energy arises from deviations from the parallel alignment of the magnetic moments, and it is related to non-parallel spin distributions. The exchange energy term can be expressed as [47]:

$$E_{exch} = A \int_V [(\nabla m)^2] dV \tag{2.22}$$

The magnetic exchange field accompany this energy is given as:

$$\mathbf{H_{exch}} = \frac{2A}{\mu_0 M_s} (\nabla^2 m) \tag{2.23}$$

In uniform 6-neighbor exchange field, the exchange field contribution from cell (i,j,k) is given by:

$$\mathbf{H_{exch}}(i,j,k) = \frac{2A}{\mu_0 M_s} \sum_{i}^{N} \frac{m(i',j',k') - m(i,j,k)}{\Delta^2} \tag{2.24}$$

Where N is the set consisting of 6 cells neighboring to cell $(i,j,k)$ as illustrated in Fig. 2.4, A is the exchange coefficient between $(i,j,k)$ and $(i',j',K')$ cells in J/m, and $\Delta$ is the discretization step size between $(i,j,k)$ and $(i',j',K')$ cells in meters [47]. At the boundaries (surface of the magnetic system) the next neighbor is missing, in that case there are more than one approach to solve this problem. Most common solution is to consider the boundary cells has a magnetic vector with the same value as the nearest one, this known as free boundary condition $\frac{\partial m_{xs}}{\partial x} = \frac{\partial m_{ys}}{\partial x} = \frac{\partial m_{zs}}{\partial x} = 0$. The exchange energy density of a single computational cell can be obtained from the following equation:

$$\begin{aligned} \xi_{exch}(i,j,k) &= -\frac{1}{2}\mu_0 M_s(\mathbf{H_{exch}}(i,j,k) \cdot \mathbf{m}(i,j,k)) \\ \xi_{exch}(i,j,k) &= A\sum_{i}^{N} \frac{m(i,j,k) \cdot (m(i,j,k) - m(i',j',k'))}{\Delta^2} \end{aligned} \tag{2.25}$$

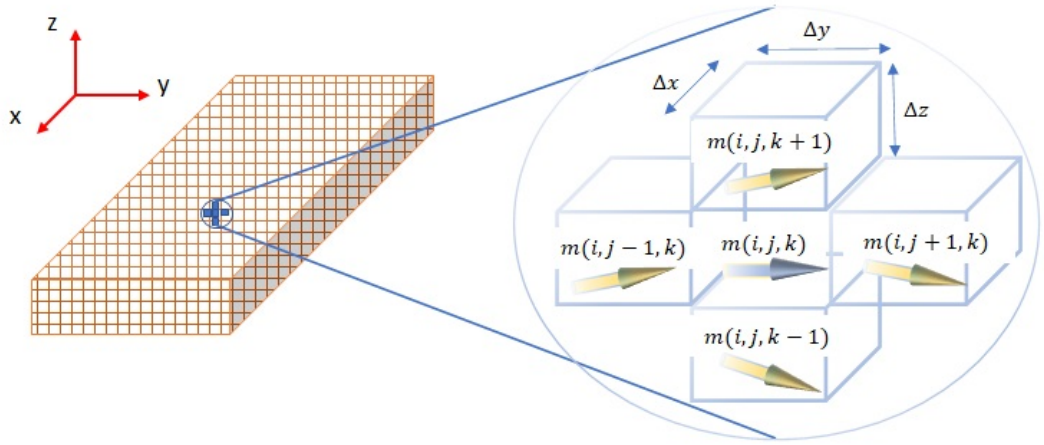


**Figure 2.4** The exchange field calculation basics, the system is discretized into cells with size steps $\Delta x$, $\Delta y$ *and* $\Delta z$. Note that the front and the rear cells are missing to give a better illustration, and the arrows represent the magnetization vectors.

### 2.2.3 Anisotropy field and energy

A material can exhibit a physical property with anisotropy effect, if that property is function of direction. The magnetic anisotropy is preference for the MDMs to lie in a particular direction in a sample. There are different types of anisotropy sources: (i) Crystal (magnetocrystalline) anisotropy which is casued by crystal symmetry, the only type that is intrinsic property. (ii) Shape anisotropy, this type is caused because of the sample shape and the effect of demagnetization (magnetostatic energy) at the surfaces which forces the MDMs to align with the surface and prevent pole formation to reduce system internal energy [106]. (iii) Stress anisotropy (magnetoelastic energy) results from the interaction between the magnetization and lattice deformation due to strain [107]. (iv) Exchange anisotropy (interface anisotropy) which arises due to coupling at the interface of fine particles or through a thin films. Fig. 2.5 shows the magnetic anisotropy in single crystals of common ferromagnetic metals Fe, Ni, and Co. In BCC Fe magnetization process is said to be easy in the <100> directions and hard in the <111> directions; that is, the field needed to magnetize iron to saturation is smaller in the <100> directions than in any others. FCC Ni requires smaller fields to saturate magnetization in the hard directions than that for Fe. Co has hexagonal unit cell, and its easy direction of magnetization is the c axis and saturating the magnetization in a sample along the hard direction is very hard, more than an order of magnitude harder than in the <111> directions in Fe.

There are two forms of magnetocrystalline anisotropy: cubic or uniaxial anisotropy. The anisotropy energy is the energy required to saturate the magnetization in particular direction. It is obvious that the anisotropy energy of a uniaxial magnetic material depends on the direction of the magnetization vector and a minimum energy is obtained when the magnetization orients toward the easy axis. A 3D energy surface for the direction of the magnetization vector can be used to visualize this contribution to the free energy. The anisotropy energy is defined as the distance from a point to the origin on the surface in that direction in the crystal. In the case of Co the energy surface has a minimum in the c direction (see Fig. 2.6) or in the plane normal to the c axis.

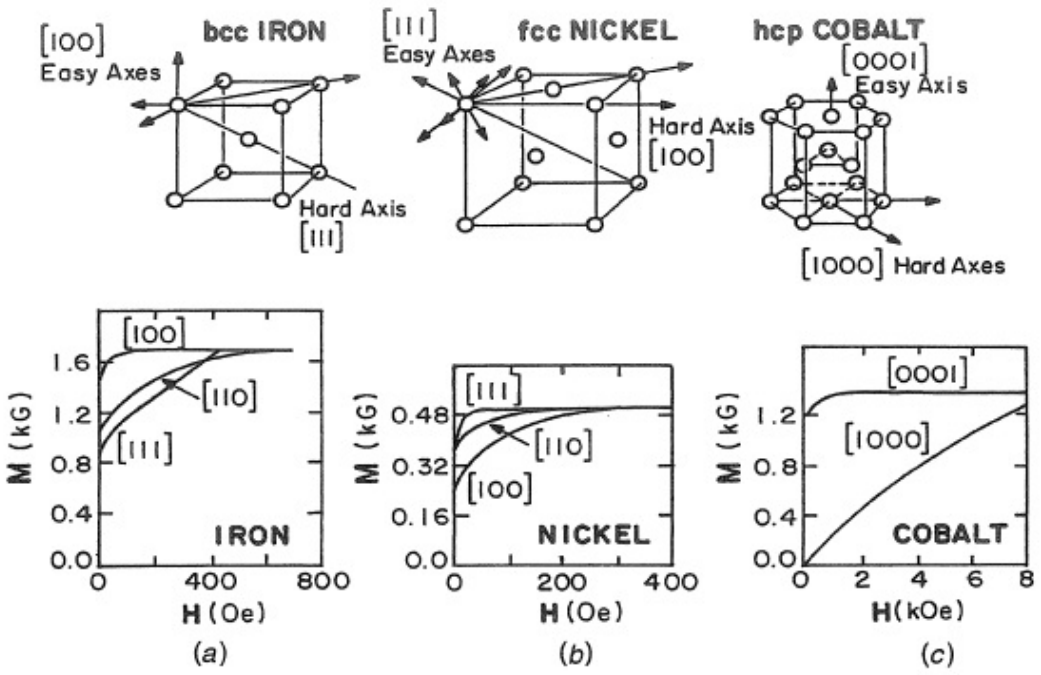


**Figure 2.5** The easy and hard magnetization axis are shown for different crystal structures: (a) Fe, (b) Ni, and (c) Co above. The magnetization as function of applied magnetic field curves are shown below. Copyright © 2005, IEEE [106].

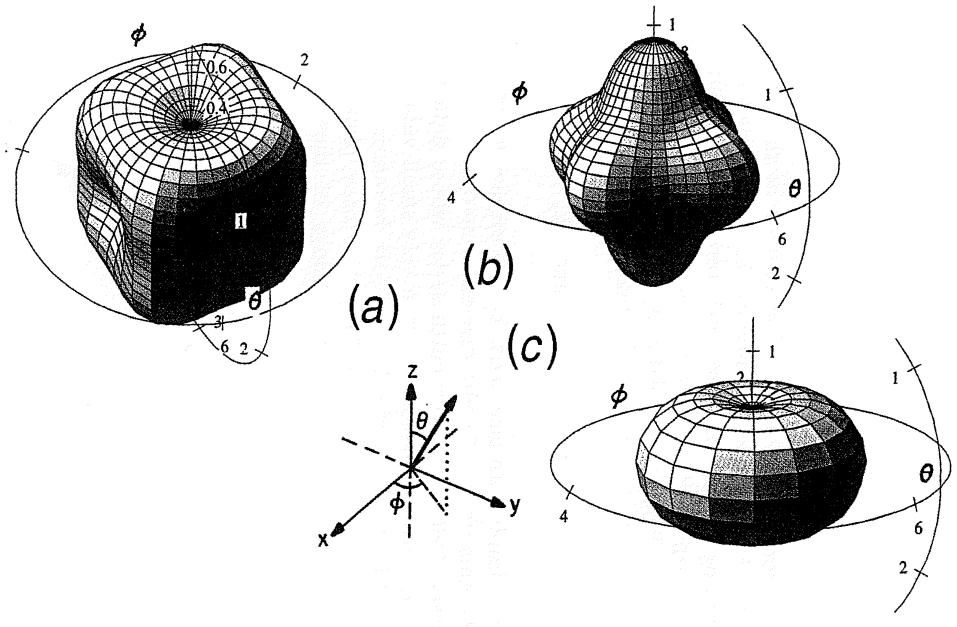


**Figure 2.6** The anisotropy energy surfaces for (a) iron, (b) nickel, and (c) cobalt. Copyright © 2005, IEEE [106].

If the MDMs in a magnetic material favor one particular direction (the easy axis) then the material has uniaxial anisotropy, like cobalt. On the other hand, if the

MDMs favor many particular directions, then the material has multiple easy axes and it possesses cubic anisotropy.

The anisotropy energy in transition metal magnets originates from from spin-orbit coupling.

### Uniaxial anisotropy

The uniaxial crystal anisotropy energy density is often expressed as a power series:

$$\xi_{uni} = \frac{U_o}{V} = \sum_n K_n sin^{2n}\theta \tag{2.26}$$

For most purposes it is sufficient to keep only the first three terms. Also, in most cases $K_2$ is negligible, and $|K_2| \ll |K_1|$ which justifies the reason to keep only the first three terms [108].

$$\xi_{uni} = K_0 + K_1 sin^2\theta + K_2 sin^4\theta \tag{2.27}$$

$K_0$ it is independent of the orientation of M, therefore it has no meaning for anisotropic properties [106]. The fourth-order approximation of uniaxial anisotropy energy density is given as:

$$\xi_{uni} = K_1 sin^2\theta + K_2 sin^4\theta \tag{2.28}$$

an equivalent form is [108]:

$$\xi_{uni} = -K_1 cos^2\theta + K_2 cos^4\theta = -K_1(\mathbf{m}\cdot\mathbf{n})^2 + K_2(\mathbf{m}\cdot\mathbf{n})^4 \tag{2.29}$$

$K_1$ and $K_2$ are the primary and secondary anisotropy coefficients obtained through experiment measurements, they depend on temperature and have units of energy density ($J/m^3$), $\theta$ is the angle between magnetization unit vector $\mathbf{m} = \frac{\mathbf{M}}{\mathbf{M_s}}$ and the easy axis $\mathbf{n}$. $K_1$ and $K_2$ can exist with either a positive or negative sign. The axis direction is an easy axis if $K_1 > 0$. Otherwise, if $K_1 < 0$, the axis direction is hard and it is the normal to the easy plane. For most cases, the energy for a uniaxial system is given by [47]:

$$E^{ani}_{uniaxial} = -\int_V K_1(\mathbf{m}\cdot\mathbf{n})^2 d^3r \tag{2.30}$$

The uniaxial anisotropy field contribution from cell $(i, j, k)$ is given as [47]:

$$\mathbf{H}^{\mathbf{ani}}_{\mathbf{uniaxial}}(i,j,k) = \frac{2K_1}{\mu_0 M_s}(\mathbf{m}(i,j,k)\cdot\mathbf{n})\mathbf{n} \tag{2.31}$$

$\mathbf{n}$ represents the anisotropy axis. if $K_1 < 0$, $\mathbf{n}$ is normal to the easy plane, and If $K_1 > 0$, $\mathbf{n}$ is the easy axis. An example of uniaxial anisotropy magnetic material is cobalt (see Table 2.1). The shape of the energy surface when $(K_1 > 0)$, is an oblate spheroid (see Fig. 2.6(c)). The minimum anisotropy energy on this surface is along $\pm z$ under zero applied field.

**Table 2.1** Anisotropy coefficients of some common ferromagnetic materials

| Material | Crystal structure | Type | $K_1$ $J/m^3$ | $K_2$ $J/m^3$ | Reference |
|---|---|---|---|---|---|
| Iron | (BCC) | Cubic anisotropy | $4.8\times10^4$ | $-1.0\times10^4$ | [106] |
| Nickel | (FCC) | Cubic anisotropy | $-4.5\times10^3$ | $-2.3\times10^3$ | [106] |
| Cobalt | (HCP) | Uniaxial anisotropy | $4.1\times10^5$ | $1.5\times10^5$ | [106] |
| $Ni_{80}Fe_{20}$ Permalloy | (FCC) | Cubic anisotropy | 0 | 0 | [109] |
| $Ni_{50}Fe_{50}$ Permalloy | (BCC) | Cubic anisotropy | $\sim 2\times10^3$ | – | [109] |
| $Fe_{50}Co_{50}$ alloy | (BCC) | Cubic anisotropy | 0 | 0 | [106] |
| $Fe_3Co$ alloy | (BCC) | Cubic anisotropy | $\sim 4\times10^4$ | – | [106] |

* These are experimental results

### Cubic anisotropy

The anisotropy energy surfaces for cubic crystals are not as easy to imagine and are not straightforward trigonometrically [106]: The anisotropy energy density of a cubic system is given as:

$$\xi_{cub} = K_0 + K_1(\alpha_x^2\alpha_y^2 + \alpha_y^2\alpha_z^2 + \alpha_z^2\alpha_x^2) + K_2(\alpha_x^2\alpha_y^2\alpha_z^2) + ... \tag{2.32}$$

Where $\alpha_i = m_i = M_i/M_s$ and $x, y$, and $z$ are the system coordinates. A positive sign for $K_1$ indicates easy axes along the body edges <100>, an example of that iron (see Fig. 2.6(a)). Change in the sign of $K_1$ indicates a change in the easy axis from <100> to <111> as shown in first order ansitropy energy surfaces, an example of that nickel (see Fig. 2.6(b)). The energy for a cubic system is given as [47]:

$$E^{ani}_{cubic} = \int_V [K_1(\alpha_x^2\alpha_y^2 + \alpha_y^2\alpha_z^2 + \alpha_z^2\alpha_x^2) + K_2(\alpha_x^2\alpha_y^2\alpha_z^2)]d^3r \tag{2.33}$$

The cubic anisotropy field contribution from cell $(i, j, k)$ is given as [47]:

$$\mathbf{H}^{\mathbf{ani}}_{\mathbf{cubic}}(i,j,k) = \frac{-2D}{\mu_0 M_s}(\mathbf{m}(i,j,k)) \tag{2.34}$$

Where $D$ is the diagonal matrix:

$$D = \begin{bmatrix} K1(m_y^2+m_z^2)+K2(m_y^2m_z^2) & 0 & 0 \\ 0 & K1(m_x^2+m_z^2)+K2(m_x^2m_z^2) & 0 \\ 0 & 0 & K1(m_x^2+m_y^2)+K2(m_x^2m_y^2) \end{bmatrix} \tag{2.35}$$

**For both cases**, the anisotropy energy density (in J/m3) of a single computational cell can be obtained from the following equation:

$$\xi_{ani}(i,j,k) = -\frac{1}{2}\mu_0 M_s(\mathbf{H_{ani}}(i,j,k)\cdot\mathbf{m}(i,j,k)) \tag{2.36}$$

It is worth noting that some ferromagnetic materials exhibit isotropic behavior with anisotropic coefficints ($K1 = K2 \approx 0$), such as permalloy $Ni_{80}Fe_{20}$ and $Fe_{50}Co_{50}$ alloy (see Table 2.1). These materials are considered soft magnets and typically very low applied field is required to saturate M along any direction.

### 2.2.4 Zeeman field and energy

The Zeeman field (external field) is an input parameter for simulation and to add this field, one need to add its value directly to the total effective magnetic field $\mathbf{H_{eff}}$ in Eq. 2.9. Zeeman energy density (in J/m3) of a single computational cell can be obtained from the following equation:

$$\xi_{Zeeman}(i,j,k) = -\frac{1}{2}\mu_0 M_s(\mathbf{H_{Zeeman}}(i,j,k)\cdot\mathbf{m}(i,j,k)) \tag{2.37}$$

Zeeman energy results from the interaction of magnetic moments with an applied magnetic field, and total Zeeman energy is given as [47]:

$$E_{Zeeman} = -\mu_0 \int_V \mathbf{M}\cdot\mathbf{H_{Zeeman}} d^3r \tag{2.38}$$

$\mathbf{H_{Zeeman}}$ involves fields externally applied, and also magnetic fields caused by currents passing through the system.

$$\mathbf{H_{current}} = -\int_V \mathbf{J}(r') \times \frac{\mathbf{r}-\mathbf{r}'}{|\mathbf{r}-\mathbf{r}'|^3} d^3r \tag{2.39}$$

#### 2.2.4.1 Oersted field

Oersted field can either be generated with a current passing along the disc normal or a time varying electric flux according to Ampere–Maxwell law as given in the following Eqn.

$$\oint \mathbf{B} \cdot d\mathbf{l} = \mu_0 \int_S \mathbf{J} \cdot d\mathbf{s} + \mu_0 \epsilon_0 \frac{\partial}{\partial t} \int_S \mathbf{E} \cdot d\mathbf{s} \tag{2.40}$$

The line integral on the lhs of the equality in the Eqn. 2.40, is the line integral of the magnetic field flux (where B is the magnetic field flux, has units of Tesla (T)) along a closed curve. J is current density (A/m2), ds is an infinitesimal area on the disc plane, $\epsilon_0$ is permittivity of vacuum, $\mathbf{E}$ is electric field. If the magnetic disc is conducting, the first term related to the current density is expected to dominate over the other unless a very sudden change of electric flux on the system with time is considered. In the limit of $J = 0$ due to either strong electric field penetration into the disc or the presence of a thin nonconducting layer on one of the surfaces of the disc preventing current flow, the first term on the rhs in Eqn. 2.40 is neglected, leaving one with:

$$\oint \mathbf{B} \cdot d\mathbf{l} = \mu_0 \epsilon_0 \frac{\partial}{\partial t} \int_S \mathbf{E} \cdot d\mathbf{s} \tag{2.41}$$

Eqn. 2.41 relates the time varying total electric flux (rhs term) through a cross sectional area S in space (ferromagnetic disc plane in the case presented herein) whose time derivative induces a magnetic field along the azimuthal coordinate (the line integral on the lhs of the equality) perpendicular to the electric flux direction (See Fig. 2.7(a)). Carrying out the integrations on both sides of Eqn. 2.41 on the disc yields:

$$B(r) = \frac{1}{2}\mu_0 \epsilon_0 \frac{\partial E}{\partial t} \times \begin{cases} r, & r \leqslant R \\ \\ \frac{R^2}{r}, & r > R \end{cases} \tag{2.42}$$

where $r$ is the radial coordinates at which B is calculated (distance from the disc center), $R$ is the disc radius. Thus, a magnetic field along the azimuthal coordinates will arise whose amplitude varies linearly with r but decaying inversely and rapidly outside the disc when r > R (See Fig. 2.7(b)).

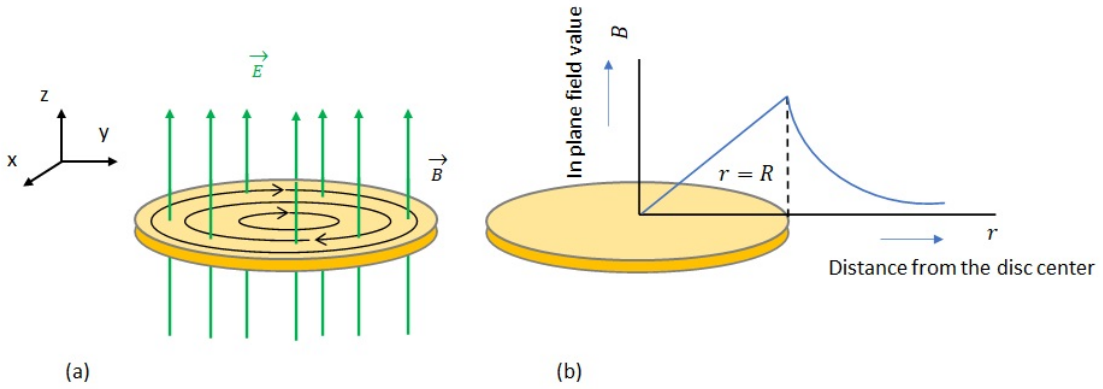


**Figure 2.7** (a) The applied time-varying electric flux perpendicular to magnetic disc along the z-axis (green vectors) and the induced magnetic field in-plane (xy-plane, black vectors) as a result of the electric field. (b) A magnetic field along the azimuthal coordinates at a distance $r$ from the disc center

When $J \neq 0$ due to electric current flowing along the disc normal due to a closed-circuit loop, the first term on the rhs of Eqn. 2.40 will contribute and even dominate the process. Neglecting the displacement field (2nd term on the rhs of Eqn. 2.40) one has:

$$\oint \mathbf{B} \cdot d\mathbf{l} = \mu_0 \int_S \mathbf{J} \cdot d\mathbf{s} \tag{2.43}$$

Carrying out the integrations on both sides of Eqn. 2.43 yields:

$$B(r) = \frac{1}{2\pi}\mu_0 I \times \begin{cases} \frac{r}{R^2}, & r \leqslant R \\ \\ \frac{1}{r}, & r > R \end{cases} \tag{2.44}$$

where I is the current flowing along the disc normal.

#### 2.2.4.2 Joule heating

Passing a huge electric current density of $10^{11} \sim 10^{12}\ A/m^2$ through a conductor produces heat. This thermal energy will raise the temperature of the system causes not only changes in spin dynamics but also a possible breakdown of the system. This process is known as Joule heating also known as Ohmic heating. You et al. have provided an analytic expression to approximate the temperature of Joule heated nanostructure by current pulse on 3D substrate as function of time, which is important in the study of the current induced magnetization switching, and the dynamics of magnetic defects such as domain walls and solitons [110]. The analytic expression is given in the following equation:

$$T(t) = \frac{whJ^2}{\pi\mu_s\sigma_w\rho_s C_s}(\ln\frac{4\sqrt{\mu_s t}}{w_G}) \tag{2.45}$$

Where T is the temperature, $w$ and $h$ are the width and height of the nanostructure, $J$ is the current density, $\sigma_w$ is the electric conductivity of the nanostructure, $\mu_s = K_s/\rho_s C_s$ is the diffusivity of the substrate, $\rho_s$, $C_s$ and $K_s$ are the density, specific heat, thermal conductivity of the substrate, $w_G = \alpha w$ is the width of the Gaussian profile, and $\alpha$ is an adjustable parameter. An example of Joule heating is provided by You et al. [110]. They consider a permalloy wire on $SiO_2$ substrate, a current density pulse of $10^{12}\ A/m^2$ and a pulse period of 5 $\mu s$ is applied. Fig. 2.8 shows comparisons between Eqns. (10) and (16-18) in Ref. [110].

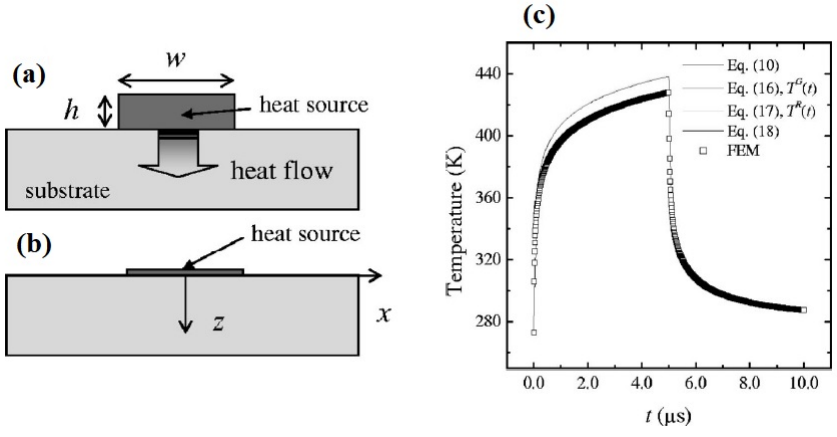


**Figure 2.8** (a) Cross-section view of nanostructure with the substrate. The thickness h and width w of the nanostructure are depicted. (c)Temperature variations with pulse period of tp=5 $\mu s$. Eqns (10) and (16-18), are solid lines, and indistinguishable. The finite element method (FEM) result is □. Reprinted from You, C.-Y., Sung, I. M., Joe, B.-K. (2006). Applied physics letters, 89 (22), 222513, with the permission of AIP Publishing. [110].

### 2.2.5 Thermal Field

The thermal field has three components $\mathbf{H_{th}} = \mathbf{H_{th,x}}, \mathbf{H_{th,y}}, \mathbf{H_{th,z}}$ which are space and time independent random Gaussian distributed numbers with zero mean value. This field describes the thermal fluctuations of the magnetization occur in the magnetic film when its temperature rises. In field discretization, each cell will get affected by a different thermal field value [111]. Thermal field of a single computational cell can be obtained from the following equation:

$$\mathbf{H_{th}}(i,j,k) = \sigma(i,j,k)\sqrt{\frac{\alpha}{1+\alpha^2}\frac{2k_BT}{\gamma\Delta V\Delta t M_s}} \tag{2.46}$$

where $\sigma$ is a Gaussian random uncorrelated function, $k_B$ is the Boltzmann constant, $T$ is the temperature in Kelvin, $\Delta V$ is the volume of a single cell, $\Delta t$ is the time step. The thermal field should satisfy the following statistical properties[112]:

$$\langle \mathbf{H_{th}},\ _i(t)\rangle = 0 \tag{2.47}$$

$$\langle \mathbf{H_{th}},\ _i(t), \mathbf{H_{th}},\ _j(t')\rangle = D\delta_{ij}\delta(t-t') \tag{2.48}$$

where D expresses the thermal fluctuations, i and j are the coordinates x,y,z, and $\langle\ \rangle$ is the average of the fluctuating field. Thermal energy density (in J/m3) of a single computational cell can be obtained from the following equation:

$$\xi_{th}(i,j,k) = -\frac{1}{2}\mu_0 M_s(\mathbf{H_{th}}(i,j,k)\cdot\mathbf{m}(i,j,k)) \tag{2.49}$$

## 2.3 Time-Dependent Voltage Pulses

Faraday's law of induction states: Under an electrical voltage drop signal, a magnetic field will be generated which is expected to be a circular and has in-plane component normal to current direction.

$$\frac{d\phi}{dt} = \oint \mathbf{B}\cdot d\mathbf{l} \tag{2.50}$$

Here $\phi = \int_s \mathbf{E} \cdot d\mathbf{s}$, it is the total electric field flux passing through a closed surface s, E is the electric field, and s is the surface where the electric field penetrates. Essentially the above equation is at a time-dependent voltage drop applied to the dielectric layer, it shows that an magnetic field starting from the central symmetry axis of the disc will increase along the interface and reach the maximum value at the lateral boundaries of the system. Whether this magnetic field is "clockwise" or "counterclockwise" affecting the ferromagnetic layer may use to stabilize and/or switch the magnetic vortex state. Although these relationships are the foundations of classical electrodynamics, the problem can be complicated in the presence of realistic and nonlinear environments. In cases where ferromagnetic and dielectric layers have linear permeability, and the numerical solution of integral equations of Maxwell's equations including the interface where a ferromagnetic is in contact with the dielectric are useful and real, electric field can penetrate into ferromagnetic layer.

$$\nabla \times \mathbf{B} = \mu_0 \epsilon_0 \frac{d\mathbf{E}}{dt} \tag{2.51}$$

As it is converted to differential operators, it is more convenient to use numerical computation (e.g. application of finite difference methods, etc.) than integration techniques. Accordingly, a "voltage signal" with a function of time defined under Eqn. 2.7 will be solved together with the Eqn. 2.51). In this way, the parameters of the manipulation of the ferromagnetic layer with vortex-type magnetic orientation under a time-varying voltage signal will be revealed (optimal form of the signal, frequency dependence, time, etc.). At this stage, a parameter that looks like detail but is very important is the time dependent form of the signal. For example, a symmetrical signal given in Fig. 2.9(a) will not change the vortex direction for the pre-signal and post-signal state, since it will create magnetic fields of the same intensity but in the opposite direction in accordance with the Eqns. 2.50 and 2.51 in the "ascent" and "descent" regimes of the signal. However, we can apply such pulses in a way that the magnetic field generated from the ascent regime of the signal has the same direction of the magnetic moments in a vortex state, and during the descent regime of the signal the magnetic field will switch its direction thus it will force the magnetic moments to switch their direction of rotation. Hence, the chirality of the magnetic vortex is switched, and the reversal of the magnetic vortex is achieved. There is another solution that one can use an asymmetrically varying signal over time (See Fig. 2.9(b)). Since the change of electrical flux to occur in the dielectric / FM interface determines the magnetic field, the situation in Fig. 2.9(b) will be able to switch the chirality of the magnetic vortex as it will create weak magnetic fields at the "ascent " and strong magnetic fields at the "descent " or vice

versa.

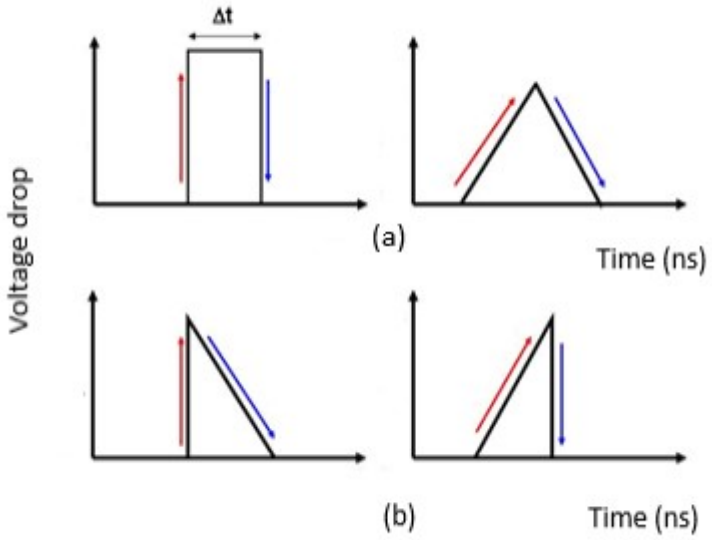


**Figure 2.9** Examples of (a) time-dependent symmetrical quadratic and triangular signals and (b) asymmetric voltage drop signals. $\Delta t$ indicates the signal duration and is expected to be within the range of a few nanoseconds (ns). In the perpendicular regime of the signals given in (b) (left: red arrow, right: blue arrow), the in-plane magnetic fields are expected to be higher than the coefficient field intensity of the Fe-Co-Ni permalloy material.

An excitation by half-cycle pulses (HCPs) is the most widely used form in controlling the spin dynamics in reduced dimensions. Realistic model temporal profiles are shown in Fig. 2.10.

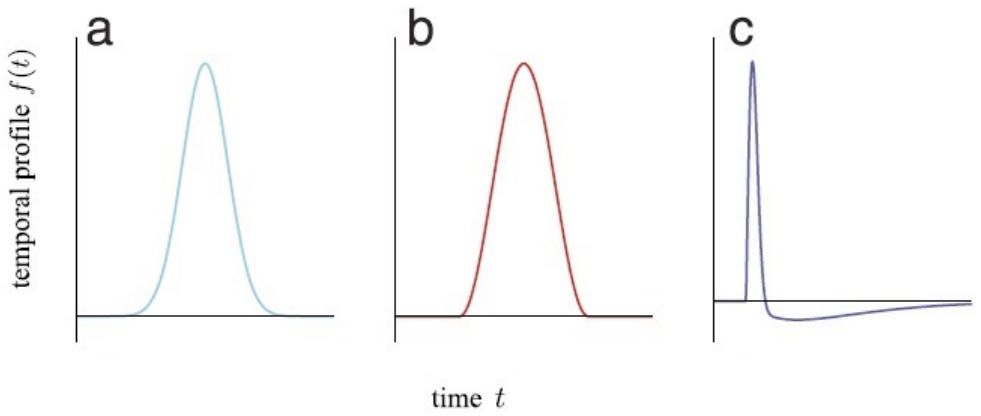


**Figure 2.10** Ultrashort pulses (a) Gaussian profile, (b) sine-square profile, (c) strongly asymmetric HCP [113]. Moskalenko, A. S., Zhu, Z.-G., Berakdar, J. (2017). Charge and spin dynamics driven by ultrashort extreme broadband pulses: a theory perspective. Physics Reports, 672 , 1–82. https://doi.org/10.1016/j.physrep.2016.12.005, Copyright © 1969, Elsevier

Fig. 2.10(a) is a Gaussian temporal profile, mathematically It is given as:

$$E(t) = E_0 \; exp(\frac{-t^2}{\tau_d^2}) \tag{2.52}$$

where $E(t)$ is a function of time, $E_0$ is the maximum amplitude, $\tau_d$ is the pulse width. Fig. 2.10(b) is the sine-square pulse profile given by:

$$E(t) = E_0 \; sin^2(\frac{\pi t}{\tau_d}) \tag{2.53}$$

Fig. 2.10(c) is the Strongly asymmetric HCP given by the following function:

$$E(t) = E_0 \frac{t}{\tau_0} \; \left[ exp(-\frac{t^2}{2\tau_0^2}) - \frac{1}{b^2} exp(-\frac{t}{b\tau_0}) \right] \tag{2.54}$$

The parameters $b$ and $\tau_0$ are the asymmetry and the duration of the HCP, respectively.

# 3. Results and Discussion

### 3.1 Micromagnetic simulations

In a micromagnetic simulation, the magnetic layer of the nanodisc is divided into cells as illustrated in Fig. 3.1. Each cell has an equal volume of $\triangle V = \triangle x \times \triangle y \times \triangle z$. We need to define a magnetization vector $\mathbf{M} = (M_x, M_y, M_z)$ in each cell. The magnetization is assumed to be constant in each computational cell which is equal to saturation magnetization. If one considers a uniform exchange interaction, in that case, each cell corresponds to the same exchange parameter A. The same is true for anisotropy interaction $K$, damping parameter $\alpha$, and gyromagnetic ratio $\gamma$.

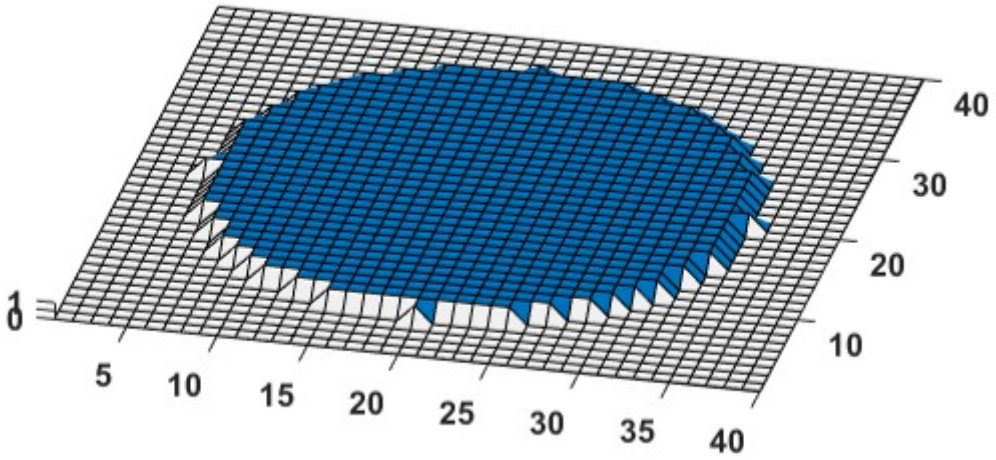


**Figure 3.1** Discretization of the magnetic layer of the nanodisc with an elliptical cross-section.

When below a critical size vortex state forms in circular FM nanodisc due to the demagnetizing field arises from the boundaries which forces the magnetic moments to align with surfaces. To obtain a vortex state as a ground state, one can start from different initial states. for example, one can start from a random configuration. Then let the system relax under zero external field, it will converge towards its ground state. However, sometimes it may get trapped in a metastable state. Fig. 3.2(a) shows how a vortex state can emerge from a random state. Also, it shows the nucleation of multiple vortex cores (See Fig. 3.2(a) at 0.2 ns). Then the annihilation of these cores by fusion. It also shows the precession of vortex core which nucleate away from the symmetry center. Fig. 3.2(b) shows the time evolution of magnetization from a random state to a vortex state with CW chirality and +1 polarity. During this process, the system relaxes and the exchange energy and demagnetiza-

tion energy decrease until they level off (See Fig. 3.2(c)). However, in this method one can not choose the initial ground state, because one of the four vortex state or a metastable will arise. Another method is to write the vortex state with applying in-plane Oersted field to obtain a specific chirality but not the polarity. Another method which is also a way to check if the 4 vortex states are degenerate, i. e. energetically equivalent from a thermodynamic perspective, is to conduct relaxation simulations under zero field from a given initial state as this would provide a basis for the configurations in the discs to attain specific chiral/polar states. To do so we prepared the 100 nm disc at 10, 20, and 30 nm thicknesses, each in the 4 states, and allowed them to relax as shown in Fig. 3.3. Note that initially "prepared" configurations, although in a vortex phase, are not necessarily in equilibrium and need to relax. Fig. 3.3 shows the relaxation of the demagnetization energy and the exchange energy for the discs with three different thicknesses. In the top row, the initial state was in-plane magnetization with a clockwise chirality and a small area in the center with positive polarity. Then the systems quickly relax in about 1 ns under zero external field as one can deduce from the energy curves in Fig. 3.3. Independent of the initial "prepared" state, all discs relax to the almost same energy densities, meaning that all four possibilities given above are degenerate. Therefore, from a thermodynamic perspective, for instance, a "CCW and negative polarity" state is energetically equivalent to a "CCW with positive polarity". The same argument holds for all discs of thicknesses considered in our work. Please note that the configurational state might relax into a different one than the initial but all states for all discs relax to the same energy range after around 1 ns. This approach allows one to obtain any state of the four vortex state and reduce the computation time. Experimentally, a random state is utilized to obtain a vortex state [43]. The random state is obtained by applying fs laser pulse which will heat the system and melt the spin structure, then during the cooling the vortex state is written by an electron beam.

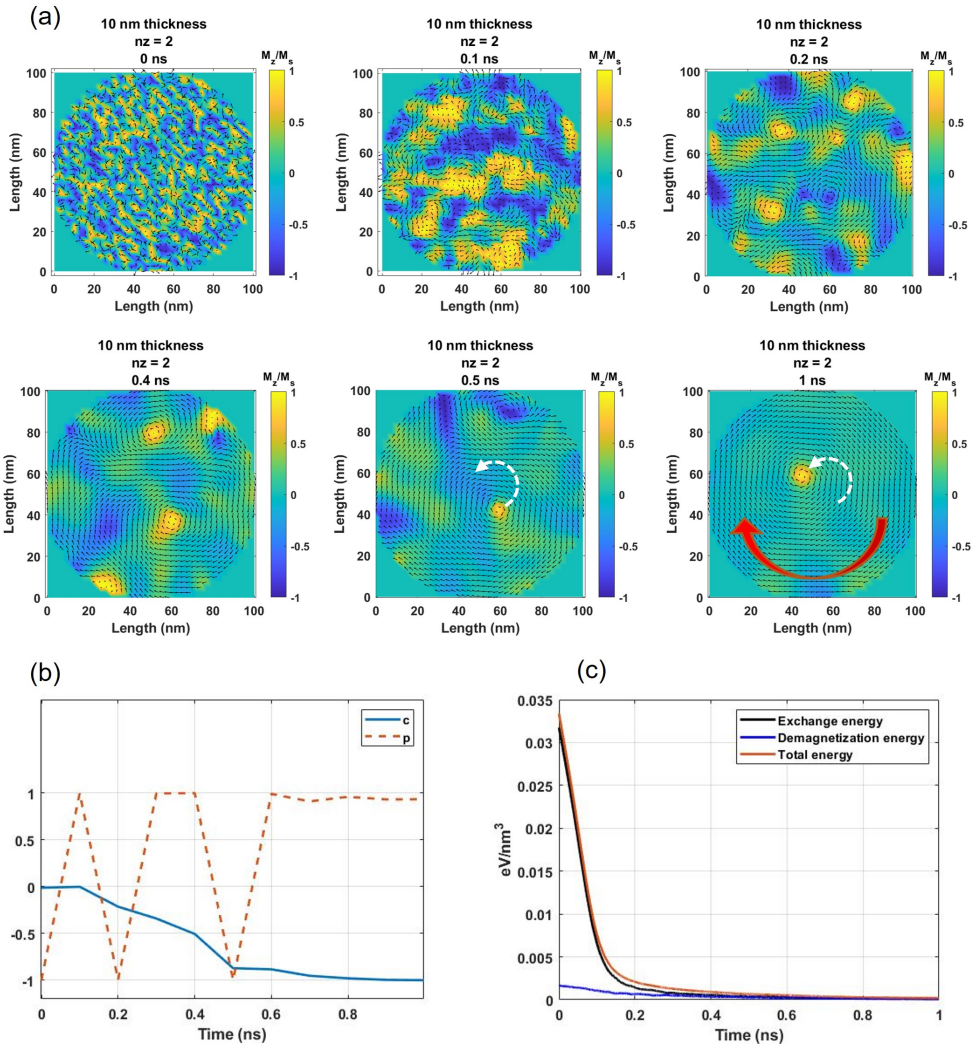


**Figure 3.2** (a) The evolution of planar magnetization vectors of PY of 100 nm diameter nanodisc from a random state to a vortex state. The magnetization vector map superimposed on the colormap of the Mz component. The white dashed arrows show the vortex core precession. The red arrow represents the chirality direction with CW rotation, (b) The chirality evolution from random state with zero value to CW rotation with -1 value and a vortex core polarity equal to 1, and (c) The evolution of energy density terms, exchange, demagnetization and total energy density of the system.

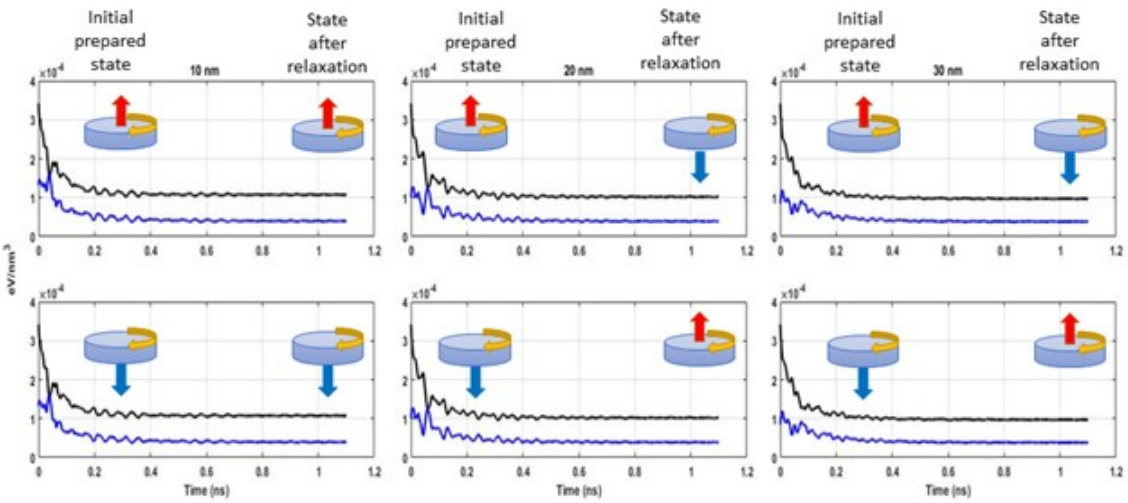


**Figure 3.3** Relaxation of vortex states initially set with the same chiralities but different polarities in nanodiscs with different thicknesses. All discs relax to identical energies, implying there is not a tendency for stabilizing in a specific chiral/polar state and that the disc thickness is not a parameter here.

The following sections present the results of applying an asymmetric or symmetric electric pulses on FM nanodiscs to control their magnetic vortex states and induce chirality and/or core polarity switching. For this purpose, we study the response of FM nanodiscs with specific geometrical dimensions which attain vortex state as their ground state to designed electrical pulses using the LLG equations with continuum Maxwell relations. These nanostructures have important implications for for spintronic applications, such as high density magnetic data storage, logic devices and microwave oscillators. Common FM materials are considered in this study. We examine and discuss the dynamics of the magnetic order during chirality and/or polarity switching processes.

### 3.2 Chirality reversal under the effect of an electric pulse [1]

The micromagnetic simulations are performed using an in-house modified code, the original code is provided in Ref. [1]. One of the factors that causes vortex nucleation is that the disc size is too small to form domains. Another factor is to minimize the demagnetizing field arising from the disc surfaces. The simulations are performed on a 95 nm diameter and a 11.4 nm thickness PY nanodisc. Material parameters are $M_s = 8 \times 10^5 \ A/m$, $A = 1.3 \times 10^{-11} \ J/m$, $l_{ex} = 5.29 \ nm$, and we choose a Gilbert damping parameter $\alpha = 0.02$. For such radius/thickness ratios, which fall into the vortex state region as previously reported in Refs [55, 58, 78, 86]. The cell size is $1.9 \times 1.9 \times 1.9 \ nm^3$. The total time for the simulations is 3 ns, consisting of 5 fs steps corresponding to 600K iterations. The initial state of the disc was obtained after 400K iterations under zero applied field starting from a random configuration. The magnetization components $\mathbf{M_x}$, $\mathbf{M_y}$, and $\mathbf{M_z}$ in each local cell satisfies the amplitude $\sqrt{(\mathbf{M_x^2} + \mathbf{M_y^2} + \mathbf{M_z^2})} = M_s$. The ground state is vortex state shown in Fig. 3.4. The composition that we consider in our simulation has the formula $Ni_{80}Fe_{20}$ and the anisotropy field is negligible with zero values for $K_1$ and $K_2$ as provided in Refs [106, 109, 114].

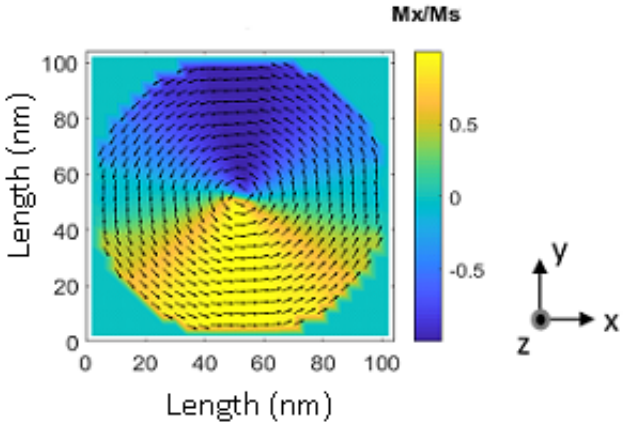


**Figure 3.4** The ground state of PY nanodisc of 95 nm diameter. The colormap here shows the Mx component.

We present the results of applying an electric field that is asymmetric and time dependent. Asymmetric half-cycle-pulses can be used experimentally and are generally

[1] The material in this chapter is from the paper published in https://onlinelibrary.wiley.com/doi/10.1002/andp.202170029 . The copyright permission has been obtained under License Number 5441320595046 and License date Dec 03, 2022, from John Wiley and Sons.

feasible. We designed four different pulses using Eqn. 2.54, with various durations as shown in Fig. 3.5(a). $E_0$ is 0.09 $V/nm$, $b$ is 180 for all pulses, and $\tau_o$ is 0.25, 0.35, 0.45 and 0.65 ns for the black, red, blue, and green pulse, respectively. A pulse in accordance with Eqn. 2.54 has a steep positive slope (head) and a negative slope (tail) asymmetrical in time, that is vital if a one way switching of the chirality is desired. If the pulse is along +z-axis, then the initial positive slope region of the pulse generates a CW traversal magnetic field while the negative slope region generates CCW traversal magnetic field. We utilize the negative slope region of the pulse to induce vortex chirality reversal. The magnetic field strength obtained from Eqn. 2.42 along the periphery of the nanodiscs ($B(r = R)$) varying over time as a result of the electric flux of the pulse is presented in Fig. 3.5(b). It is the radial magnetic field whose maximal value is plotted in Fig. 3.5(b) that enters the simulations as $\mathbf{H_{Zeeman}}$ in Eqn. 2.9.

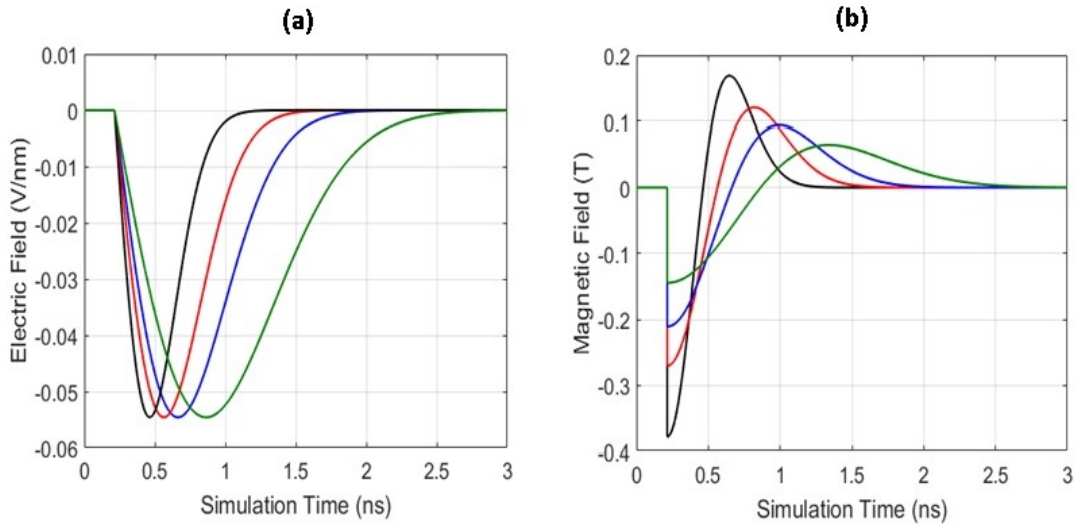


**Figure 3.5** (a) The electric fields applied with various time periods obtained from Eqn. 2.54. (b) The magnetic fields at ($B(r = R)$) derived from Eqn. 2.42.

The chirality of the nanodiscs were tracked under the pulse shown in Fig. 3.5(a) with the accompanying edge magnetic fields (3.5(b)) in Fig. 3.6. We note that there exists a critical pulse duration for chirality to reverse or else switching does not proceed (See the green data in Fig. 3.5(a) for the pulse and Fig. 3.6 for chirality).

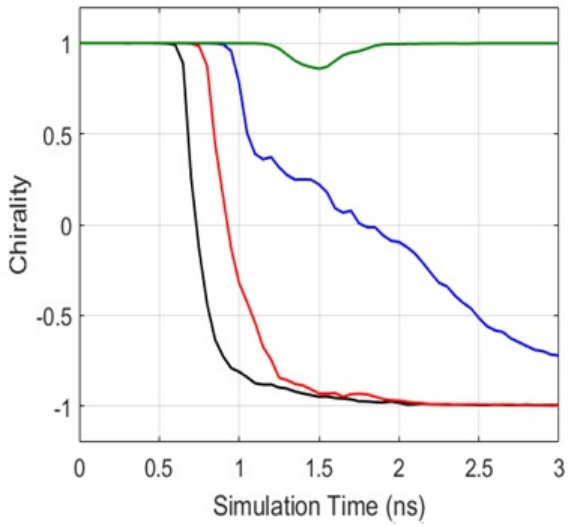


**Figure 3.6** The chirality reversal of the vortex state under the application of different electric pulses provided in Fig. 3.5(a).

The amplitude of the Oersted magnetic field to induce switching of chirality depends on the time derivative of the electrical pulse signal as seen in Eqn. 2.42: $d(E)/dt < 0$ yields a CCW and $d(E)/dt > 0$ yields a CW Oersted magnetic field. Keeping this in mind, the two electrical pulse signals (red and black) shown in Fig. 3(a), can switch the vortex state in about 1.5 ns after which the system remains stable in the CW state, and thus a reversed chirality state is obtained. However, under the (blue) pulse, the system requires more time to relax into the CW state. As expected from Eqn. 2.42, a longer electrical pulse signal generates a weaker magnetic field owing to the shallower slope in relation to the time axis. To overcome this, the strength of the electric pulse needs to be increased or otherwise chirality switching does not occur. We find that the electrical pulse signals required to induce switching can be shorter than 1 ns if the electrical signal strength is higher than 0.55 $MV/cm$.
Fig. 3.7, shows temporal evolution of the chirality from CCW to CW state after applying an electrical pulse signal of a strength approximately 0.55 $MV/cm$ along z-axis. Note that at t=0, the system is in its ground state whose data is given in Fig. 3.4. For an applied electric field pulse (black signal Fig. 3.7(a)), the switching starts with loss of order of the magnetic moments that are near the edge where the radially generated magnetic field is maximum as shown in Fig. 3.7(c-2). As the boundary sites lack neighbors, the electric pulse induced magnetic field at its maximum value dominates over the exchange field, realigning these magnetic moments. However, the initial CCW vortex core (yellow dot) [See Fig. 3.8(3)] still remains and spatially oscillates near the center at the time when the signal is turned off. Note that at 1 ns, a new vortex CW core (blue dot) starts to nucleate, with time evolution

the CW and CCW cores start to interact [Fig. 3.8(3-7)], and a yin-yang type of transient state near the center is observed where the magnetization aligns with the field under a Zeeman torque near the edges where the magnetic induction is at its highest. Eventually, CCW yellow core is annihilated which is observed between (1.9-2.1) ns, leaving its position to the CW (indicated by the blue core in Fig. 3.8(7-8). Apart from $\mathbf{H_{ext}}$ being maximal at the disc periphery, that magnetization vectors near the edge of the nanodisc experience a higher demagnetizing field make these dipoles respond earlier to the pulse-induced magnetic field compared to the interior sites of the disc. Similarly, in exactly the same manner, the vortex can be switched back into the CCW configuration with an electrical pulse signal in the +z direction. Thus, a deterministic and swift switching of the chirality is possible to achieve with the primary coupling of the $\mathbf{B}$ to $\mathbf{M}$.

In order to be able to track layer-wise variations associated with the vortex core, first its coordinates in the plane of the disc need to be determined in each layer of the disc, i.e., through the thickness of the disc. For this purpose, at each magnetic dipole site, ij in a given layer, we calculated the chirality "both spatially and globally" given by:

$$Chirality = \frac{1}{nM_s} \oint \mathbf{M}.\mathbf{dl} \tag{3.1}$$

where M is the magnetization in the XY-plane of the disc and $dl$ is the arc length of the path which was chosen as the circle centered at the magnetic dipole site with a radius equal to the dipole-dipole separation on the computational grid. In Eqn. 3.1, n is the number of sites over which the integral is evaluated. M values on a given path were determined via bilinear interpolation, a method used to form continuous curves on discrete set of data points, especially when one has to evaluate an analytical expression such as in the case of chirality defined as an integral over a closed continuous path. For the spatial chirality mapping procedure, magnetization components of the nearest and next nearest sites neighboring a given coordinate i,j were used. In order to track the global chirality of the disc, this procedure was applied to concentric circular paths with the disc center being the reference coordinate whose average chirality yielded results such as in Fig. 3.7. Chirality attains values ranging between -1 and +1 for CW and CCW oriented vortices respectively and a value of zero for a homogeneously magnetized media.

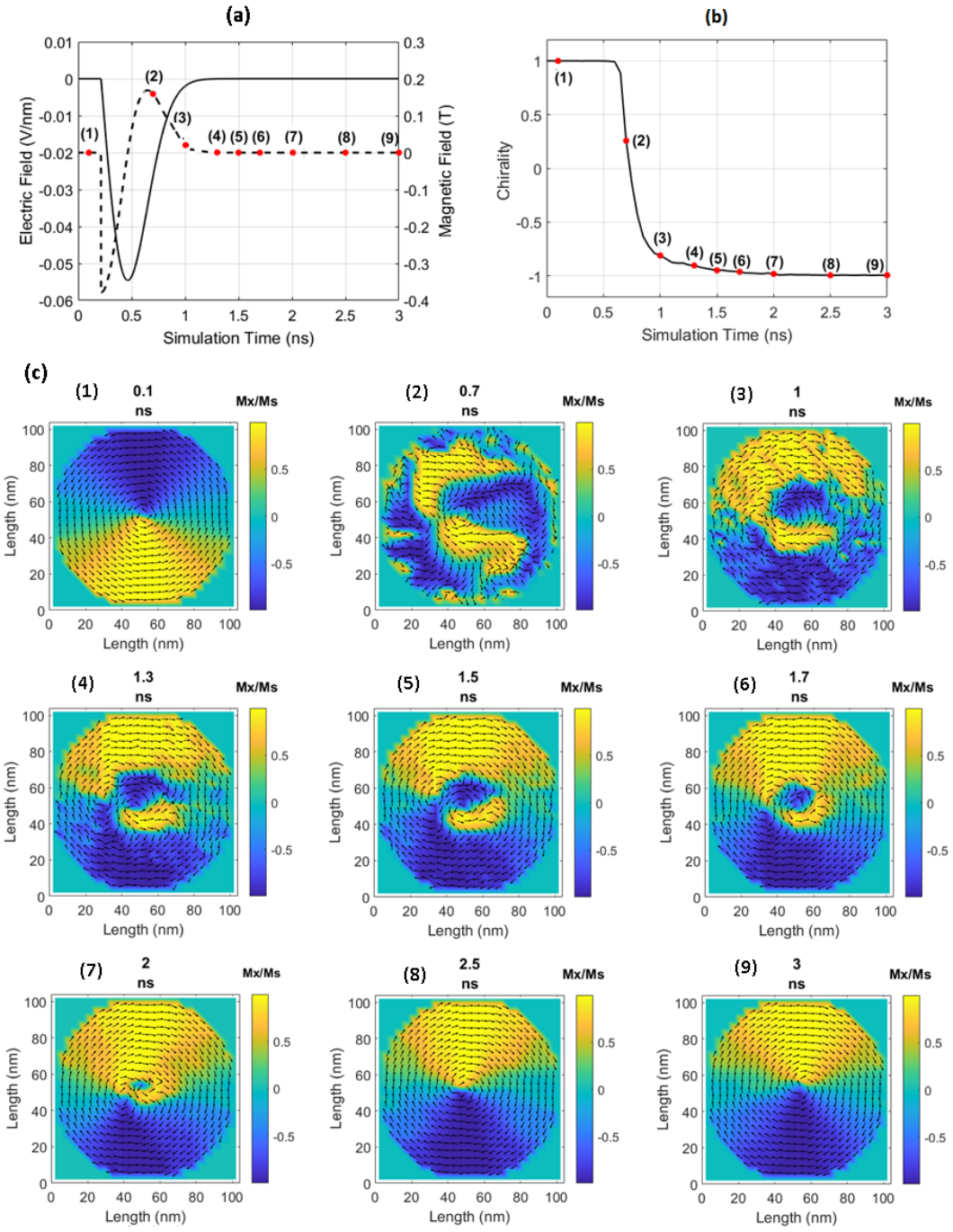


**Figure 3.7** (a) The electric field (solid line) and the induced magnetic field (dashed line) obtained from Eqn. 2.42. (b) Chirality reversal of the vortex state under the effect of the pulse given in (a). The red dots labeled as (1-9) in (a) are the snapshots illustrating the magnetization vector map in (c) under the effect of the electric field. The chirality states in (1) and (9) are CCW and CW, respectively, which indicate that the chirality state has switched.

Under the action of the black pulse shown in Fig. 3.5(a), we use Eqn. 3.1 as prescribed to track the vortex core position(s) and locate its coordinates on the vector field map of the magnetic dipole moments (MDMs), as shown in Fig. 3.8. The magnetic vortex cores ($|Chirality| > 0.8$) are labeled as a yellow dot for the CCW vortex orientation while a blue dot for CW vortex orientation. During switching, two cores can appear: At 1 ns, a new vortex core starts to nucleate with CW orientation near the center. Although the signal is turned off (see Fig. 3.5(a) at 1 ns), the old CCW remains and oscillates near the center of the disc. As the iterative steps of the simulation progresses, these cores interact while the magnetic dipoles near the disc edge have already switched to the CW state. To keep the demagnetization energy of the system in a local minimum, the MDMs along the periphery tend to be parallel to the disc edge. The exchange interaction for ferromagnetic materials favors the parallel alignment of the neighboring MDMs. Thus, a configuration according with a CW orientation gradually settles in a dominant portion of the disc after the field is switched off and the CCW core is annihilated at 2 ns as displayed in (7-8) of Fig. 3.8. Eventually, a reversed vortex chirality is stabilized.

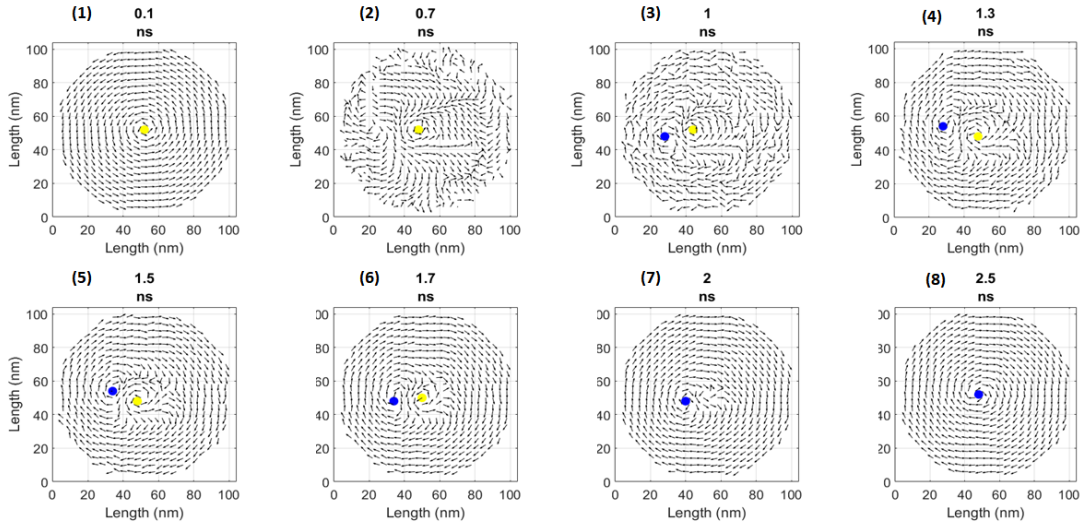


**Figure 3.8** The vortex core motion in response to the electric field given in Fig. 3.5(a). The yellow and blue dots represent the local CCW and CW chirality states, respectively. The CW core nucleates during the reversal process under the field effect, finally the CCW core disappears and CW core settles in the disc center (see (7)-(8)).

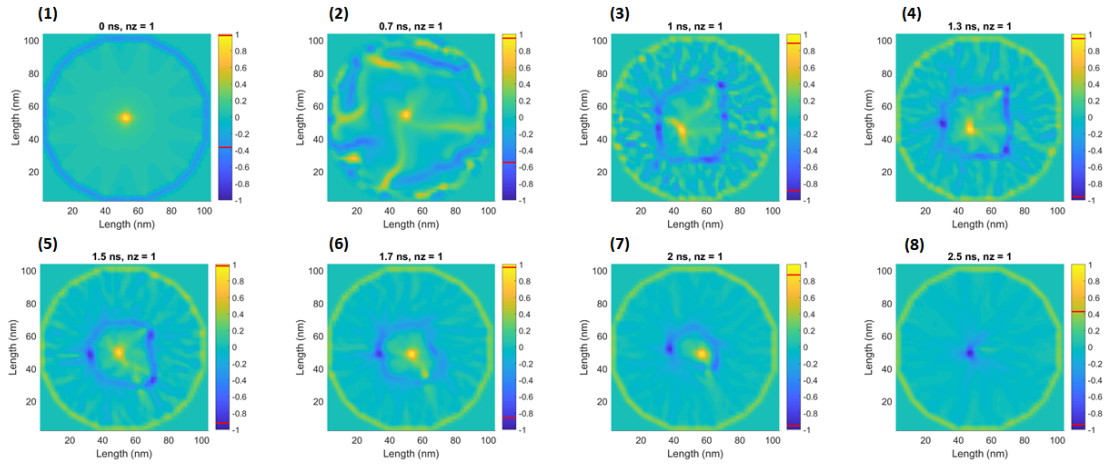


**Figure 3.9** The time evolution of Chirality switching from CCW (yellow dot) to CW (dark blue dot).

Fig. 3.9 presents the color maps which were obtained from Eqn. 3.1 where we can visualize the "degree of chirality". The yellow region represents the CCW state while the dark blue region represents the CW state. After applying the electrical signal pulse, a distinct ring forms at approximately 1 ns. This blue "chirality ring" that shrinks in radius with progressing simulation time mainly consists of antiparallel aligned dipole couples along x- and along y- at neighboring sites, yielding an overall negative value chirality locally. Along the ring, nucleation of CW vortices are visible as dark blue spots. These blue rings separate "switched" regions close to the disc periphery than regions that are "about to switch", which we deduce from the plot in Fig. 3.10. Here, we provide the average of the line integrals along circles at various distances to the center obtained from See Eqn. 3.1. It can be seen that along the paths close to the disc periphery, switching has occurred as can be deduced from the change of the average line integral value for these circular paths. The same value for the inner rings fluctuate between 1 and 0.5 until around 1.5 ns, implying gradual disappearance of the CCW order representing these regions followed by changing of chirality sign after around 1.75 ns. The blue rings corresponding to negative chirality appear inside of the nanodisc at around 0.7 ns and denote the boundary between the two tendencies. They gradually merge into a single ring, which acts as a site for nucleation of an at least one CW vortex that annihilates the CCW vortex at the center belonging to the state preceding the application of the electric pulse. The latter remains almost all the way through the switching process. We also note the manner with which the blue rings form near the periphery, first as individual segments that later on coalesce and shrink towards the center is related to the radial dependence of the magnetic field induced by the electric pulse. The very same reason causes an inhomogenous switching that start from the edges where the

pulse induced magnetic field is at its max. We deduce so because a virtual circular but homogeneous magnetic field does not induce such formations during switching (not shown here). It is the maximal value of the magnetic field at the periphery of the disc induced by the electric flux that causes the CW alignment parallel to the planar magnetic field direction. With further steps in the simulation, this ring gets smaller in diameter, rendering more dipoles switching towards the CW state emanating from the switching of dipoles propagating towards the interior. A dark blue region (CW nucleation) starts to appear (on the left side of the yellow region), and between 2 and 2.2 ns timesteps the yellow region that was the core of the CCW state disappears, and the dark shade representing the vortex with CW chirality locates itself in the center, stabilizing the global CW state. Please note that the apparent non-zero chirality at the disc periphery at all times is due to the fact that sites along this periphery lack neighbors and yield a non-zero result for the integration of Eqn. 3.1 and is therefore an artificial effect although its sensitive to the magnetization direction.

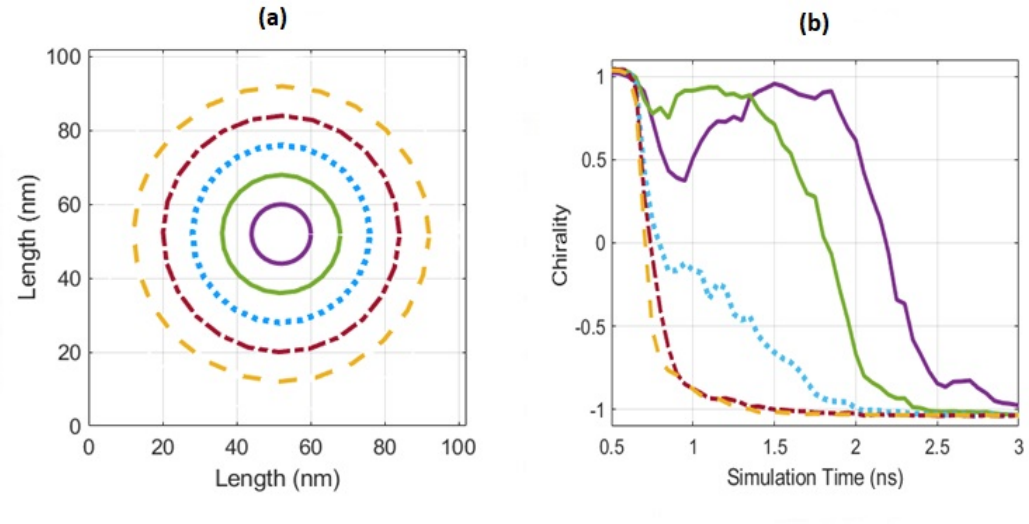


**Figure 3.10** (a) The average line integral (see Eqn. 3.1) at distinct circular paths. (b) The time evolution of chirality for each path given in (a).

### 3.3 Geometry effects on chirality and polarity reversal [2]

The simulations are performed using OOMMF [2], which is based on integrating the LLG equation on a discretized system. Part I, thickness effect: PY $Ni_{50}Fe_{50}$ nanodiscs having 100 nm diameter with 10 , 20, 30 and 40 nm thicknesses were considered. Part II, diameter effect, PY $Ni_{50}Fe_{50}$ nanodiscs having different diameters and thicknesss, the diameter range is between (100 -200 nm) and the thickness between (10-20). The dimensions fill within the feasible limits experimentally as demonstrated in Refs. [75, 115–117]. Such choice of thickness also allows us to stay within the stability regime of the vortex phase as this topological phase strongly depends on the disc aspect ratios as reported in Refs. [58] and [55]. Material parameters for PY $Ni_{50}Fe_{50}$ are $M_s = 1.11 \times 10^6$ A/m, $A = 5.85 \times 10^{-12}$ J/m, $l_{ex} = 2.76$ nm, and $\alpha = 0.02$. Magnetic anisotropy for the composition of interest here is negligibly small and is not considered [109, 114]. The cell size is $2.5 \times 2.5 \times 2.5$ nm$^3$. The ground states of the nanodiscs under zero field are vortex states given in Fig. 3.11 according to Refs [55, 58, 70, 86, 87], these predictions are accurate wherein various configurations of ferromagnetic order were computed as a function aspect ratio for a nanodisc.

In the simulations, we focus on time dependent electric pulses capable of generating an Oersted magnetic field that can alter magnetic vortex chirality of the nanodiscs. Such a field can either be generated with a current passing along the disc normal or a time varying electric flux as given on the rhs of Eqn. 2.40. In the limit of $J = 0$ due to either strong electric field penetration into the disc or the presence of a thin a thin nonconducting layer on one of the surfaces of the disc preventing current flow. We designed two sets of pulses which have the shape of sine-square temporal profile(see Eqn. 2.53) with two different amplitudes $E_{01} = 2\ V/nm$ and $E_{02} = 3\ V/nm$ given in Fig. 3.12(a) and (b) respectively. Each set contains two pulses with opposite sign separated by 2 ns time interval where the switched state following the first signal is allowed to relax. It is worth to note that such an electric field is expected to generate a magnetic field in the azimuthal coordinates relative to the direction of the electric field.

[2] The material in the following sections reproduced from Ref. W. A. S. Aldulaimi, M. B. Okatan, K. Sendur, M. monbasli and I. B. Misirlioglu, Nanoscale, 2022, DOI https://doi.org/10.1039/D2NR02768B with permission from the Royal Society of Chemistry.

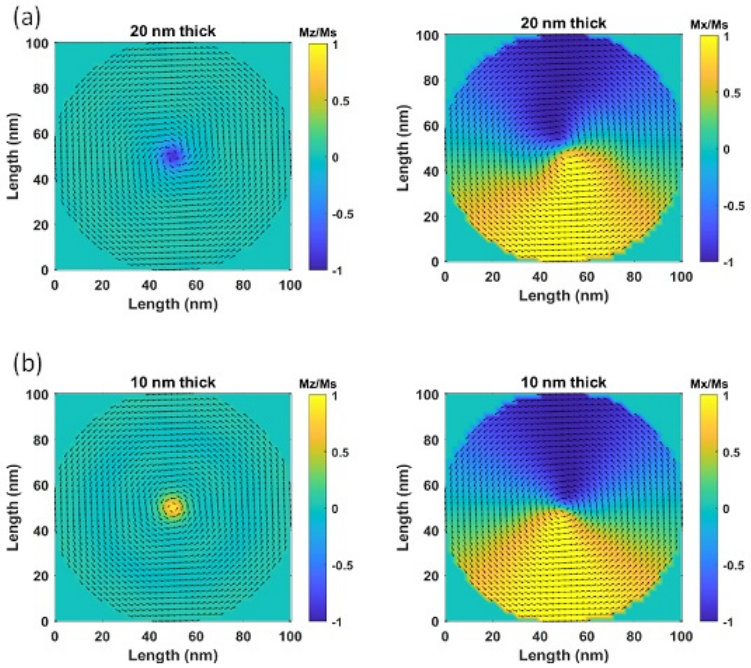


**Figure 3.11** Plan view vector maps of the PY Ni50Fe50 nanodisc stabilized in the vortex configuration as their ground states after system relaxation at zero field: (a) Left: 20 nm thick disc with CCW chirality having a polarity (Mz) in the negative direction (into the page here), Right: Map of the MX component in the plane of the disc (b) 10 nm thick disc with CCW chirality having positive polarity (out of the page). The colormaps superimposed on the vectorial plots are given to show the Mz component on the left panel and Mx component on the right panel.

When $J \neq 0$ due to electric current flowing along the disc normal (excluding the spin transfer torque effect due to spin polarization of the current) due to a closed-circuit loop, the first term on the rhs of Eqn. 2.40 will contribute and even dominate the process. Neglecting the displacement field (2nd term on the rhs of Eqn. 2.40) Eqn. 2.40 reduces to Eqn. 2.43. For this case, a significantly reduced pulse amplitude is required to prevent Joule heating. Exactly the same magnetic field form and amplitudes given in Fig. 3.12(e) can be achieved via the currents that can drive chirality reversal. If we consider a homogenous current density across the cross section of the disc, namely $J = \sigma E$, $\sigma = 1/(25 \times 10^{-8}\ \Omega m)$ for PY, one can obtain a maximum magnetic field of about $B_s \approx 0.8\ T$ at the disc periphery via applying a maximum current density of $\approx 2 \times 10^{13}\ A/m^2$ as a result of a pulse amplitude of $E_{0_1} = 0.0064\ V/nm$ whose radial form is schematically shown in Fig. 3.12(c) and another pulse was applied to induce a magnetic field of about $B_s \approx 1.2\ T$ via applying a maximum current density of $\approx 3 \times 10^{13}\ A/m^2$ result of a pulse amplitude of $E_{0_2} = 0.0095\ V/nm$ whose radial form is schematically shown in Fig. 3.12(d).

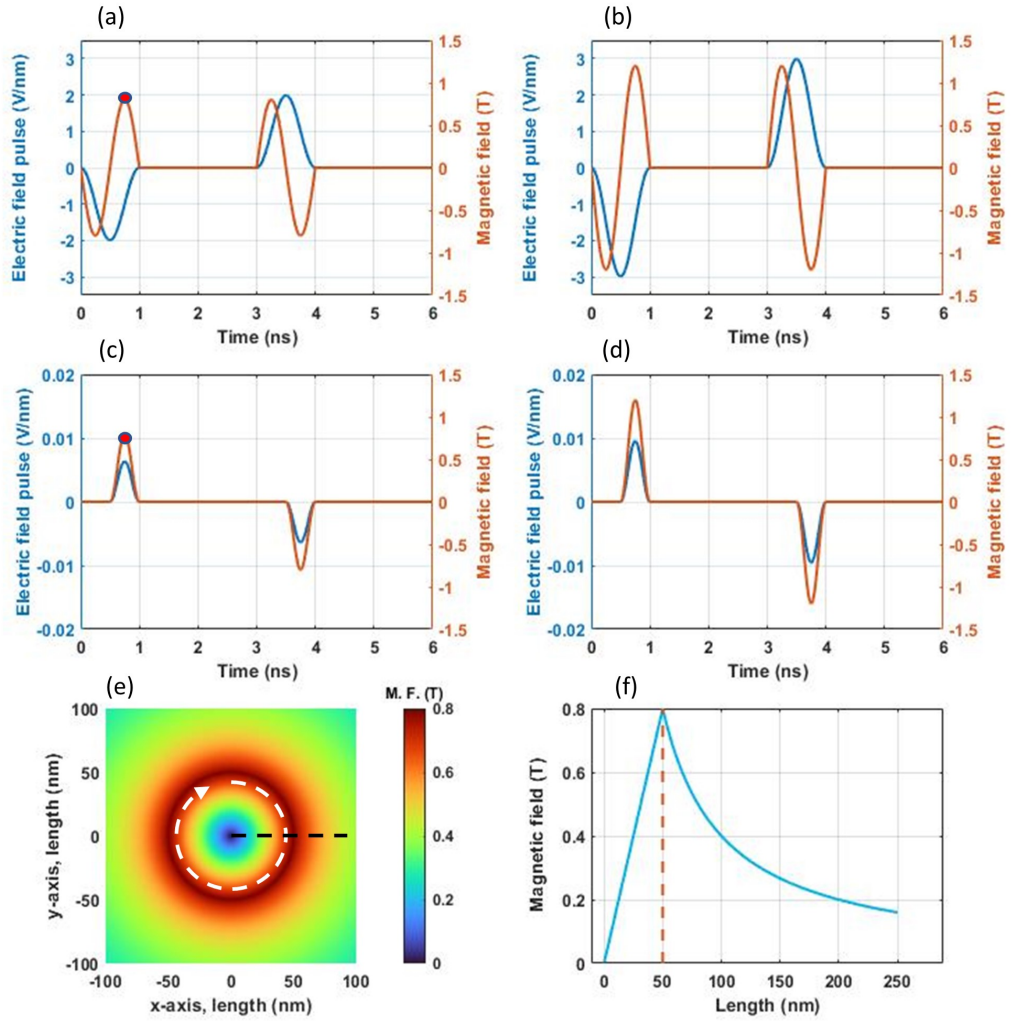


**Figure 3.12** (a and b) in case that $J = 0$ (a) The electrical pulse with the accompanying form of the Oersted magnetic field along the disc periphery is derived from Eqn. 2.53.The first pulse between 0 and 1 ns acts on the already relaxed discs followed by the wait-time between 1 ns and 3 ns, after which the second pulse but with the opposite sign is applied to the discs.(b) The pulse used to induce reversal in the 10 nm thick disc that is 0.5 times higher in amplitude than that of in (a). (c) and (d) represent the case when $J \neq 0$. (c) shows a time-varying ns electric current pulse with the accompanying form of the Oersted magnetic field along the disc periphery derived from Eqn. 2.44. The first pulse between 0.5 and 1 ns acts on the already relaxed discs followed by the wait-time between 1 ns and 3.5 ns, after which the second pulse but with the opposite sign is applied to the discs. In (b) the pulse, used to induce reversal in the 10 nm thick disc, is 0.5 times higher in amplitude than that of in (a). (e) plots the spatial planar distribution of the Oersted field strength (units in Tesla), induced by the electric field pulse or current flow of the indicated maxima (red dots) presented in (a) and (c). The white arrow and color-coded bar indicate the in-plane direction of the magnetic field. (f) provides the value of the induced magnetic field (units in T) along the disc radius and outside of the disc as well. Note that outside the disc, the field decays very rapidly with the distance as B $\alpha$ $\frac{1}{r}$.

If one considers the results in Fig. 3.12 for a disc interfacing with a substrate such as $SiO_2$, a common practice for similar device designs, the rate at which the heat dissipation is expected to occur due to the passage of current becomes an important question. As mentioned in Sec. 2.2.4, going to high current densities to get Oersted fields capable of inducing chirality reversal brings about the Joule heating into question as the PY would have a finite resistance. Upon application of a pulse as in Fig. 3.12(c) to a PY disc having 100 nm in diameter and with 2 different thicknesses, the Joule heating that is generated in response is shown in Fig. 3.13. We were able to obtain these results from Eqn. 2.45 in Ref. [110] where heat conduction was considered.

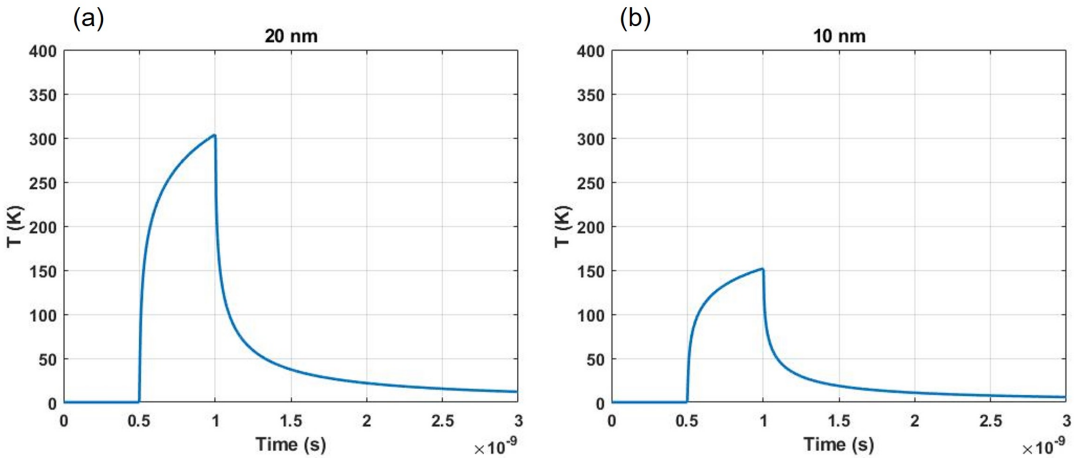


**Figure 3.13** Average temperature of the discs in K as a function of time for two different disc thicknesses (a) 20 nm, and (b) 10 nm.

### 3.4 Chirality and polarity response

We provide the chirality and polarity response of the 10 nm and 20 nm thick discs to the first of the electrical pulses (between 0 and 1 ns) in Fig. 3.14. The Oersted field to reverse chirality can either be generated by the currents flowing along the disc normal corresponding to the case when the nanodisc is treated as a conductor, or the time variation of the electric flux (the second term containing the time derivative on the rhs of Eqn. 2.40). The form of the Oersted field for both the rhs terms in Eqn. 2.40 is provided in Fig. 3.12(e) and (f). In the rest of this section, we considered the magnetic fields generated by the pulses given in Fig. 3.12(a) and (b) to obtain the results, treating the PY in the insulating limit (See Fig. 3.12 for details). The plan view distribution of the Mx and My components (color scaled quiver plots

in Fig. 3.14) reveals the vortex state stabilized in the two discs starting from their respective ground states. Upon application of the pulsed electric field in Fig. 3.12(a), the thicker 20 nm disc undergoes a reversal process as tracked via the chirality and polarity displayed in Fig. 3.14(a) and (c) as well as the planar magnetization maps 3(b) and 3(d) provided at various instants during the application of the pulse and proceeding the pulse. The thinner disc, on the other hand, remains unresponsive to the very same pulse (See the pulse in Fig. 3.12(a)) as neither the chirality nor the polarity are altered (appearing as a flat line in Fig. 3.14).

We provide chirality and polarity reversal results for 10 nm, 20 nm, 30 nm, and 40 nm thick discs wherein we applied an electric field pulse to induce chirality reversal of $E_{01} = 0.0064$ V /nm (See pulse shape in Fig. 3.12(c) in the original manuscript). We do so to also confirm that thickness impacts the chirality reversal process due to the barriers reduced with increasing disc thickness, as well as checking the relation between polarity and chirality. Defining a term such as sgn(p)×sgn(c) where we basically multiply the sign of polarity with the sign of chirality, neglecting their specific values, one can shed light on the polarity-chirality relation. By tracking this product, we can tell if there is a "coupled chirality-polarity" switching for 10 nm, 20 nm 30 nm, and 40 nm thick discs during the reversal process. If the sgn(p)×sgn(c) remains constant, this would mean that chirality and polarity are coupled, i. e., they switch together under an applied pulse. We have plotted the results for 10 nm, 20 nm, 30 nm, and 40 nm discs in Fig. 3.15.

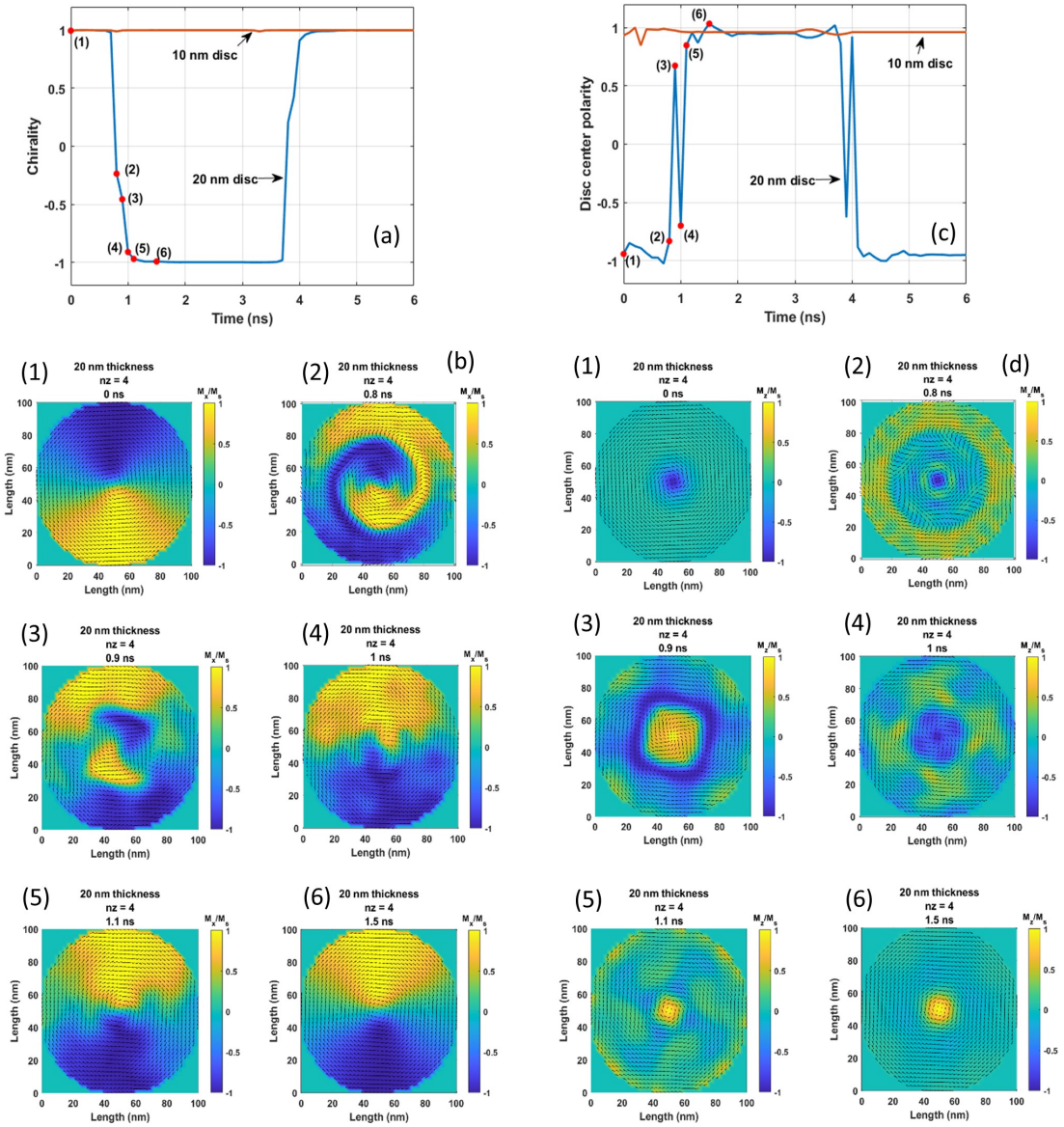


**Figure 3.14** (a) The vortex chirality in response to the time dependent electrical pulses given in Fig. 3.12(a). (b) Red points labeled as (1-6) in (a) are instants where we show the magnetization vector maps in response to the electrical pulses. (c) disc center polarity of the system during the reversal process and (d) gives the polarity maps at the instants labeled with the red points in (c).

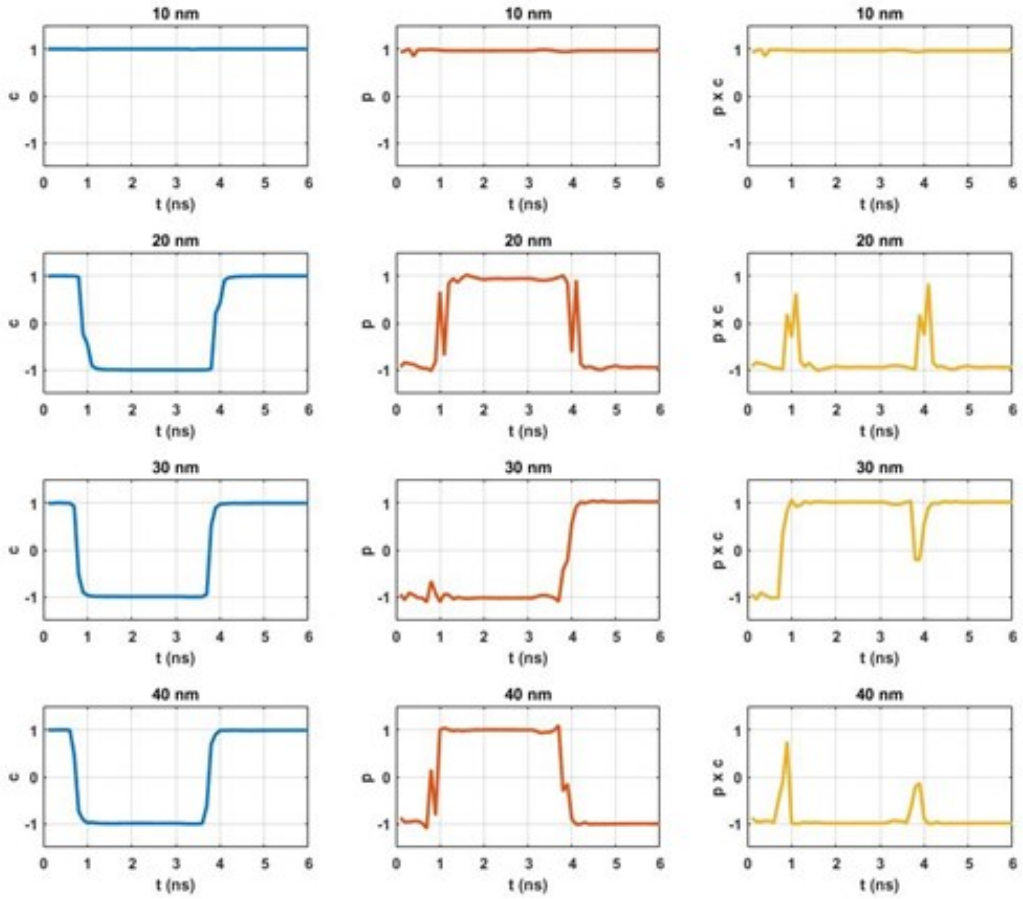


**Figure 3.15** The chirality (c, left column of plots), polarity (p, middle column of plots), and sgn(p)×sgn(c) result (right column of results) for 100 nm permalloy nanodiscs of 10 nm, 20 nm, 30 nm, and 40 nm thickness. Note that the 30 nm thick disc signals no coupling of chirality and polarity as the sgn(p)×sgn(c) product changes sign after reversal, meaning c and p behave independent of each other. The peaks in 20 nm and 40 nm thick discs appear due to the transient disorder during switching. The 10 nm disc displays no peaks as reversal has not occurred for the pulse used to generate the above plots. We give here the values other than -1 or +1 for the product arising from the p×c term to avoid disconnected curves when sgn(p)×sgn(c) changes sign.

### 3.4.1 Chirality-Polarity correlation

In order to verify a possible chirality-polarity correlation during excitation (application of an external field), we conducted a simulation by applying a strong homogeneous magnetic field pulse of 1 T along the z-axis (namely the disc normal), see Fig. 3.16. Note that this is different than applying a planar field via passage of a current along the disc normal or a time-varying short pulse. The homogeneous 1T

magnetic field applied along the normal of the disc here covers the majority of the disc area (See Fig. 3.16 (a)). We created 2 pulses to track the polarity and chirality response with time: The first pulse is opposite to the polarity sign and because of the very strong field most of the dipoles are forced to align with it, which reveals that the polarity has switched as in Fig. 3.17(a). For the prescribed pulse in Fig. 3.16, one can see that the polarity as well as the chirality respond to the applied 1T field along the disc normal (See Fig. 3.17(a)). The relaxed state following the first pulse (between 0.5 and 2 ns) reverses its polarity and chirality upon the application of the second pulse at 2 ns (Fig. 3.16(c)). Noting that there is no in-plane component of the direct applied magnetic field, it is possible to state in this case that polarity is connected with chirality. However, by reducing the effective area of the same magnetic field pulse to around 10 nm radius centered around the central symmetry axis of the disc (See Fig. 3.16(b)), we note that polarity reverses, but chirality does not (See Fig. 3.18). This implies that the polarity and chirality are coupled via a short-range interaction (See Fig. 3.18) as the reversal of the polarity at the disc center does not activate the chirality reversal of the disc.

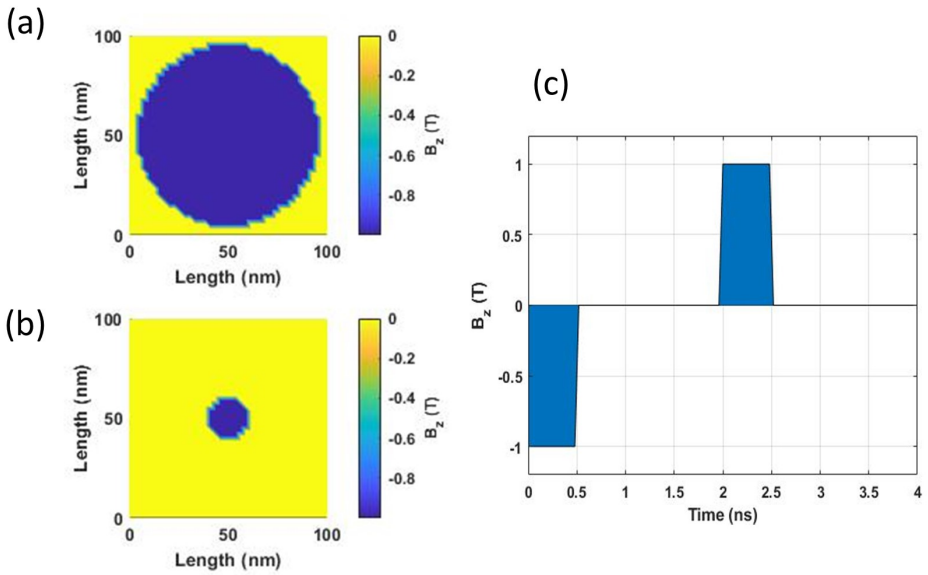


**Figure 3.16** A homogeneous magnetic field pulse along the disc normal is applied through (a) a large effective area almost equal to the disc size, (b) a small effective area, and (c) magnetic field pulse amplitudes and durations shown in time. Both fields act to reverse the polarity and we checked if the vortex chirality also reversed in response to the former.

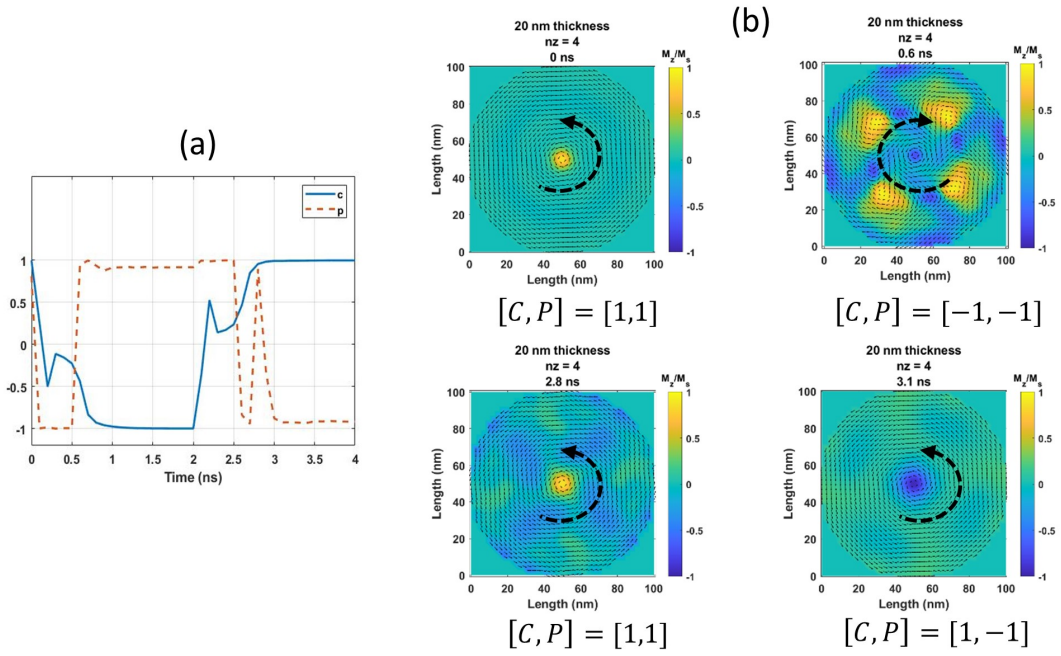


**Figure 3.17** (a) The blue line represents the chirality of the vortex state and the red dashed line represent the polarity of the vortex state in response to the magnetic field pulse given in Fig. 3.16(a), (b) snapshots were taken at different instants (2.8 ns and 3.1 ns) to illustrate the chirality (c) and polarity (p) states.

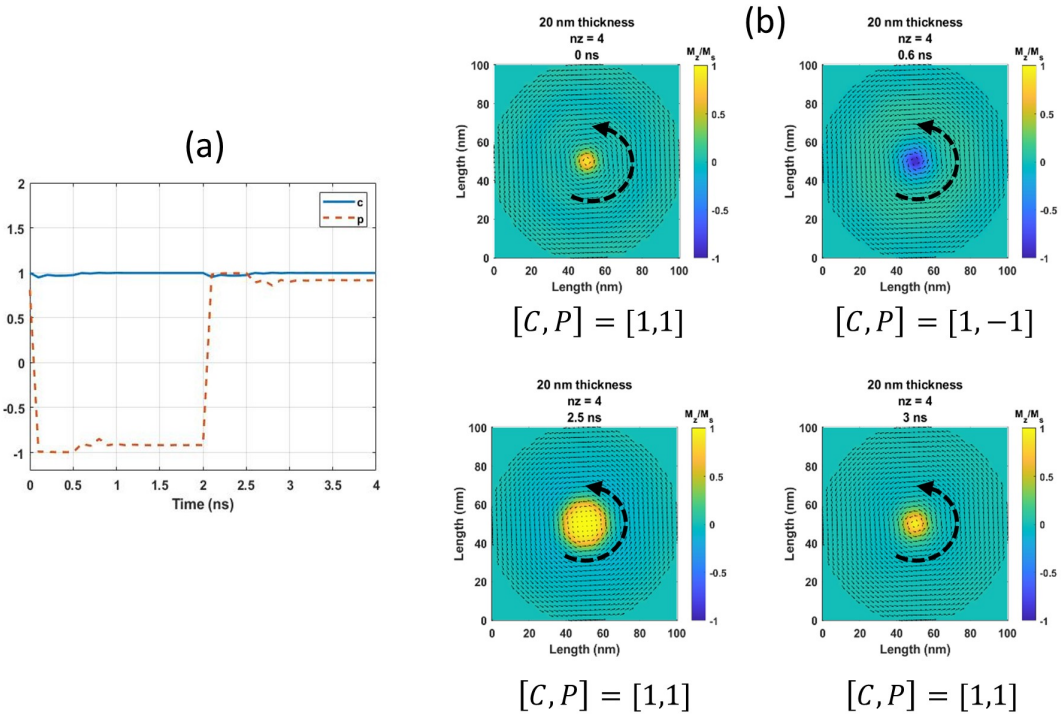


**Figure 3.18** (a) The blue line represents the chirality of the vortex state and the red dashed line represent the polarity of the vortex state in response to the magnetic field pulse given in Fig. 3.16(b), (b) snapshots were taken at different instants (2.8 ns and 3.1 ns) to illustrate the chirality (c) and polarity (p) states.

In Fig. 3.19, the polarity may oscillate between +1 and -1 during the application of the field in Fig. 3.16 for the range of thicknesses considered indicates that there is no strong coupling between the two parameters.

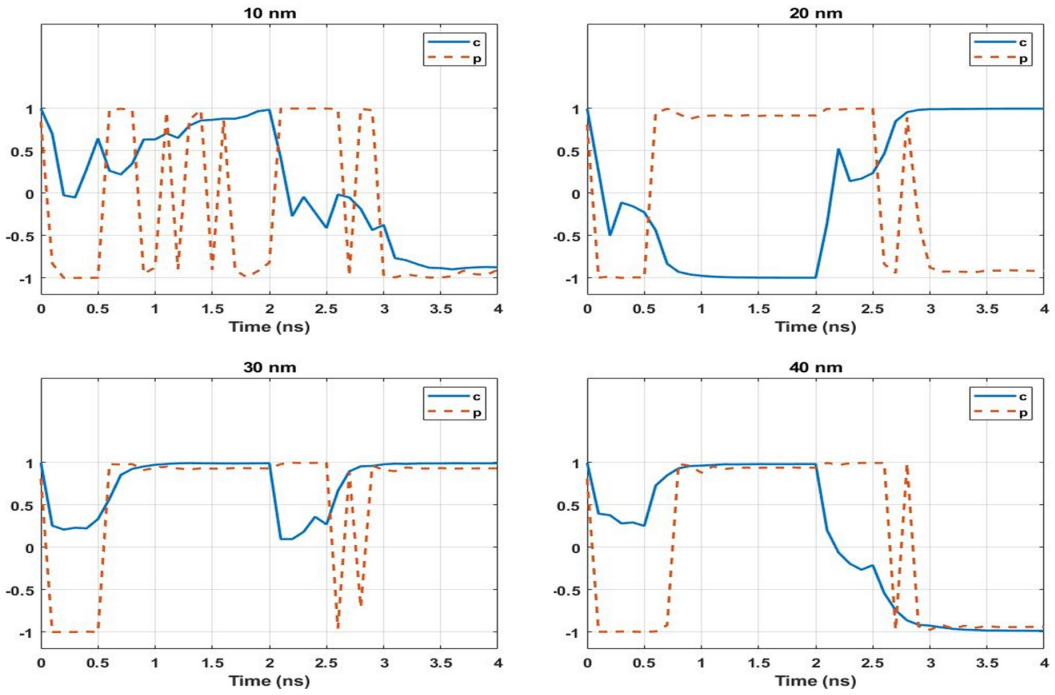


**Figure 3.19** The chirality and polarity evolution in response to the magnetic field pulse given in Fig. 3.16(a) for discs with different thicknesses: (a) 10 nm, (b) 20 nm, (c) 30 nm, and (d) 40nm. That the polarity may oscillate between +1 and -1 during the application of the field in Fig. 3.16 indicates that there is no strong coupling between the two parameters.

It was observed that polarity switching can drive chirality reversal in a fashion similar to the right hand rule where the product sgn(p)×sgn(c) always remained the same. On the other hand, independent of the polarity-chirality correlation behavior under perpendicular applied fields, we realize that all possible combinations of polarity and chirality correspond to the same energy states for both the 10 nm, 20 nm, and 30 nm thick discs (See Fig. 3.3). This implies that, in the thermodynamic limit, a state with a given chirality is not expected to exhibit different energies if it has a positive or a negative polarity. As we are conducting the simulations under external fields generating magnetic fields with spatial dependence, the degeneracy of the reversed state relative to the initial state are not directly evident in the results presented herein. So, despite an apparent correlation between polarity and chirality in the 10, 20 nm and 30 nm thick discs (See Fig. 3.15) during chirality reversal, we would like to refrain from making strict generalized statements on polarity-chirality coupling in such systems.

### 3.5 The effect of disc thickness on chirality and polarity reversal

In order to understand the dramatic difference in the response of the thin and the thick discs to the applied pulses, we computed and tracked the various energy terms in Eqn. 2.9, focusing specifically on the exchange energy and the demagnetization term that arise from the system response to the external pulse and are expected to compete during the reversal process. The signal whose form and amplitude are given in Fig. 3.12(a) is again applied to both systems wherein a 3 ns interval of relaxation is present that allows for the tracking of the stability of the reversed chirality. Concurrent with the simulation, the exchange and the demagnetization energy terms of the two discs are plotted in Fig. 3.20 during this process. The peak in the exchange energy is due to the deviation of the adjacent sites from the local parallel alignment, generating strong gradients of the vector M in Eqn. 2.22. Peaks in the demagnetization mostly stems from the Mz along the normal at the top/bottom surfaces during the reversal as these regions intercept the largest flux from the magnetic moments of the disc. For the given signal "strength" in Fig. 3.12(a), the 20 nm thick disc undergoes reversal as demonstrated in Fig. 3.14. Transient states during reversal for the 20 nm disc are revealed by the peaks in the energy terms in Fig. 3.20(a). The 10 nm disc, on the other hand, does not switch (See Fig. 3.20(c)) under the same pulse the 20 nm thick disc switches (the pulse in Fig. 3.12(a)). This implies that the magnitude of the barrier to reversal in the 10 nm thick disc is greater than that of the 20 nm one. In fact, checking this further for 30 nm and 40 nm discs, we identify that the energy peaks get reduced in magnitude, confirming our view that the energy barriers to chirality reversal are smaller in thicker discs (See Fig. 3.21). The induced magnetic field amplitudes capable of chirality reversal for the 20 nm thick disc are not very different from that of reported in Ref. [118] both via experiments and via micromagnetic simulations, pointing out to the local nature of the reversal process as the dimensions of the discs studied therein are considerably more.

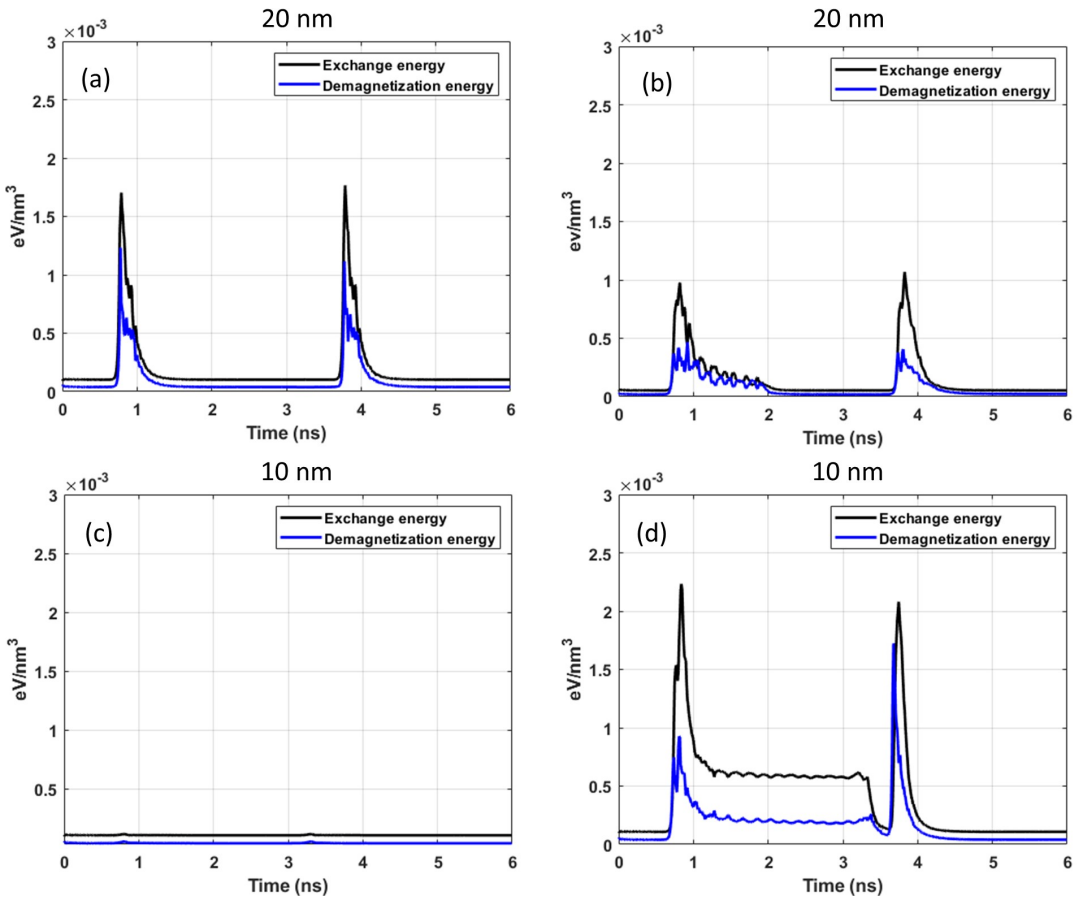


**Figure 3.20** Comparison of the exchange and demagnetization energy terms in (a) and (b) for the 20 nm thick disc under and (c) and (d) for the 10 nm thick disc under the pulses given in Fig. 3.12(a) and (b), respectively. In (b) a lower barrier is realized as the stronger Oersted field tends to induce a higher degree of local alignment of dipoles along the plane thereby reducing the z-component contribution, lowering the demagnetization energy as well compared to the result in (a).

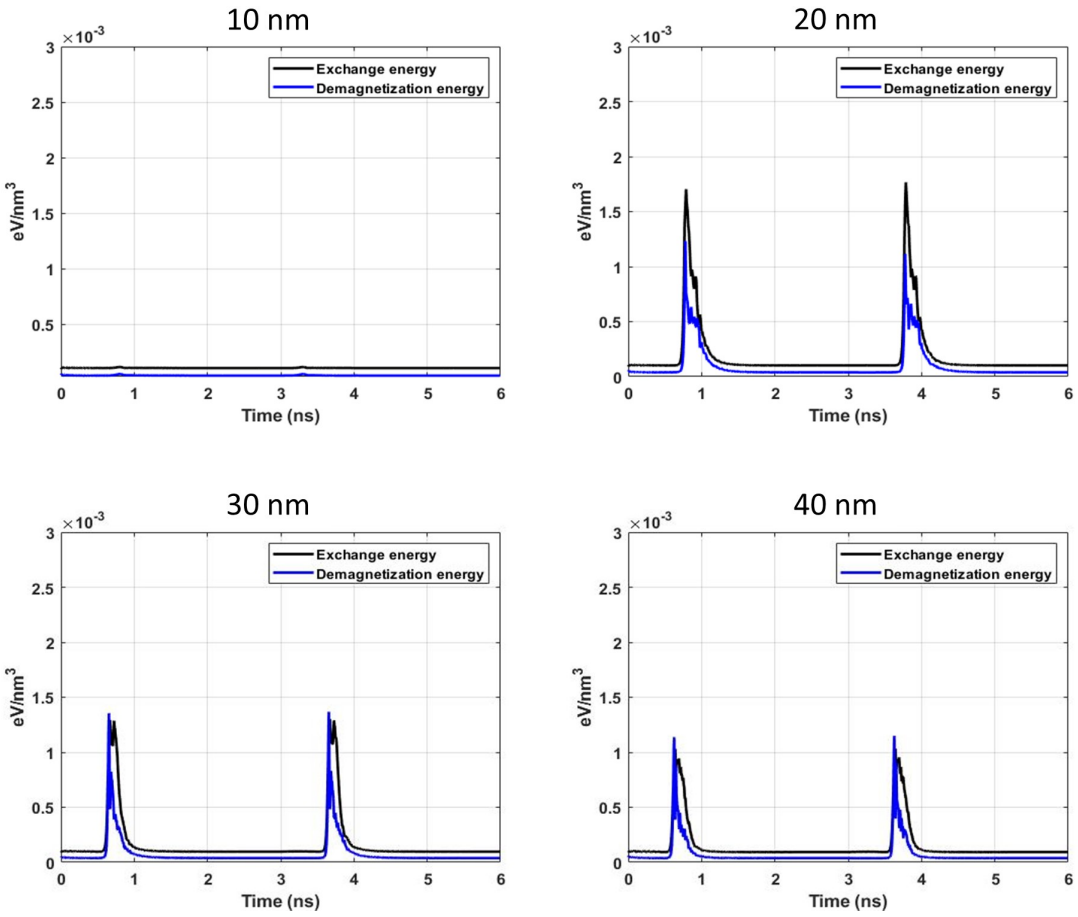


**Figure 3.21** Comparison of the exchange and demagnetization energy terms in (a) 10 nm thick disc, (b) 20 nm thick disc thick, (c) 30 nm thick disc, and (d) 40 nm thick disc under the pulses provided in Fig. 3.12(a).

To be able to justify the above argument based on the energy barriers, we increased the magnitude of the pulse 0.5 times of that in Fig. 3.12(a), forming the pulses in Fig. 3.12(b) for which the exchange and demagnetization energies of the 20 nm and 10 nm discs are provided (See Fig.3.20(b) and (d)). Under the stronger pulse in Fig. 3.12(b), the 10 nm thick disc also undergoes chirality reversal evidenced by the peaks in the exchange and demagnetization energy (See Fig.3.20(d)). That the peak magnitudes in the 10 nm are higher than the 20 nm underpins the argument that the thinner disc has to surmount a higher energy barrier for chirality reversal. Moreover, in striking contrast with the 20 nm thick disc, a vortex-antivortex (v-av) lattice that gyrates around the disc center (See Fig. 3.22) is detected and observed during the chirality reversal process of the 10 nm disc. The v-av lattice is a metastable state as can be deduced from the energy plot in Fig. 3.20(d). The time duration the v-av lattice forms and transiently exists corresponds to the interval between 1 ns and 3.5 ns in Fig. 3.20(d), confirming the metastability of this state relative to the single vortex ground state signaled by the flat energy regions. We find that the v-av

state, once formed, does not exhibit a prolonged existence even in the absence of any external fields (such as the second pulse in Fig. 3.12(b)) and quickly decays into the single vortex state. The single vortex state after chirality reversal then gyrates around the center of the disc that gradually slows down and stabilizes at the center.

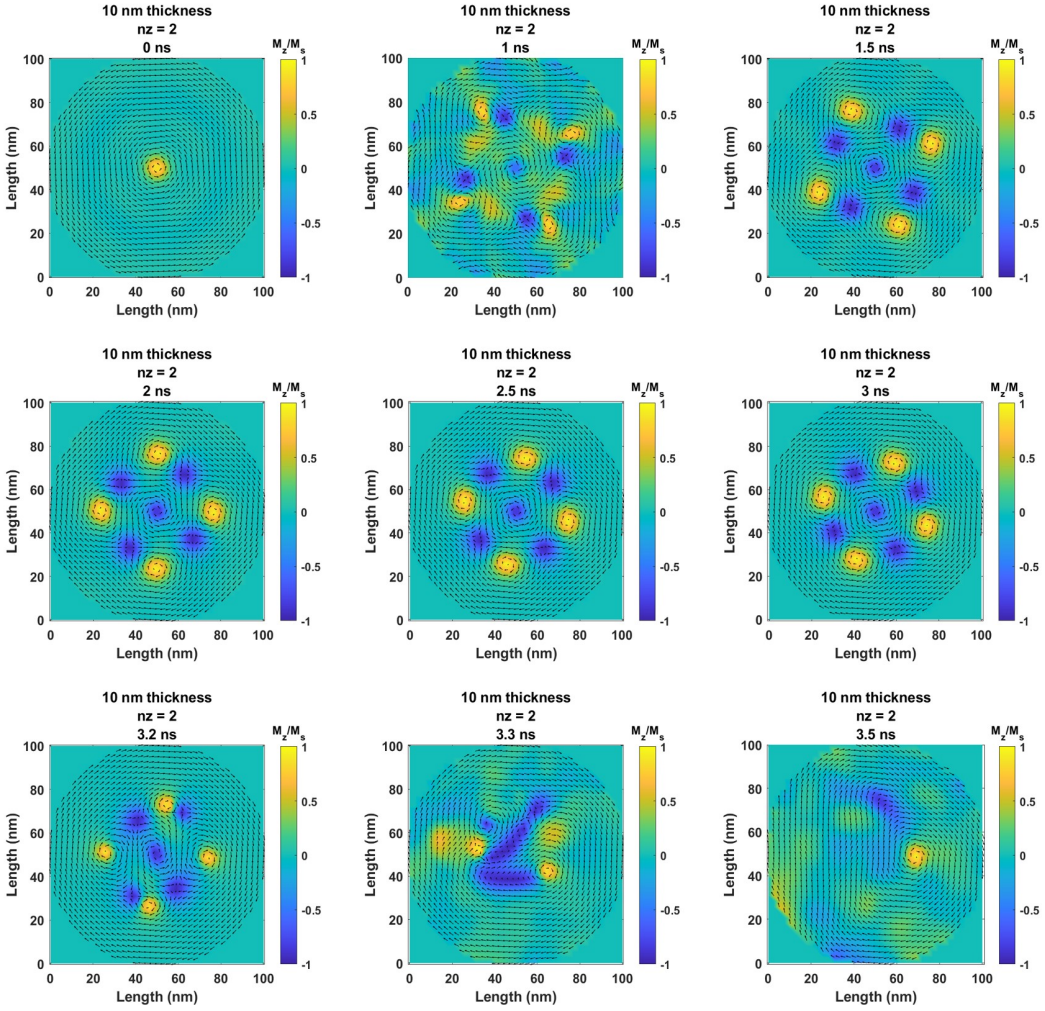


**Figure 3.22** The appearance of the v-av lattice as a transient state during switching of the 10 nm disc under the pulse provided in Fig. 3.12(a).

### 3.6 Polarity and $\alpha$ effect on core precession

The vortex core precession trajectory depends on the vortex polarity as well as on the damping constant as formulated in Ref. [119]. The trajectory of the vortex in our simulations for the computed polarity is also consistent (CCW) with that predicted in Ref. [119]. It is useful to state here that the precession frequency

and the trajectory can depend on the value of the damping constant $\alpha$. In order to understand the effect of the damping constant in a micromagnetic simulation, we tracked the formation of the transient states during the switching process and computed the various energy terms in a 10 nm thick disc in two separate simulations with two different damping constants $\alpha = 0.02$ and $\alpha = 0.05$. For $\alpha = 0.02$, A fusion of v-av lattice occurs without any external field applied, leaving behind a single vortex core with $p = +1$ which is nucleated away from the disc center during the switching process around 3.5 ns, this vortex core gyrates around the disc center and follows a CCW precession trajectory until it settles down in the disc center (See Fig. 3.23(a)). For $\alpha = 0.05$, a vortex core is formed by the fusion of multiple vortex cores around 3.2 ns with $p = -1$, after formation, the newly formed core follows a CW precession trajectory (See Fig. 3.23(b)). A large damping constant inhibits the fluctuations and the core precession follows a shorter trajectory to the disc center (See Ref. [119]). The exchange and demagnetization energy terms justify the above arguments, the fluctuations are prominent with a small damping constant (See Fig. 3.24(a) between 1-3 ns). The reason behind the fluctuations in energy terms is that the v-av lattice rotates around the center and a breathing mode is observed (breathing mode; the displacement of vortex cores from the disc center increases and decreases). Using a large damping constant yields fewer fluctuations and a shorter lifetime for v-av lattice which will decay into a single vortex core eventually (See 3.24(b)). It seems that the energy barrier is dropped a little with larger damping term (See 3.24(a) and (b), the reason is that the second term in LLG (See Eqn. 2.7) forces the magnetic moments to align with the effective field, using large damping constant will exert even a larger force on the magnetic moments and prevent them from forming a higher energy state.

The v-av lattice exhibits alternating polarity at the v and av centers as shown in Fig. 3.25, reminiscent of the 180° domain structures in thin ferroelectric films that appertain to the depolarizing fields emanating from the imperfect screening of the polarization charges at the film/electrode interface. However, such an argument fails to explain the v-av lattice occurrence as we find that the demagnetization field for such a structure is more pronounced compared to a single vortex configuration (See Fig. 3.24). That the transient v-av lattice state in the 10 nm thick disc appears to be favored during chirality reversal in the thinner disc, we find, is the result of what one can identify as a momentary soliton formation (See Ref. [85]) during the peak of the exchange and demagnetization energy (at around 0.8 ns in Fig. 3.24) that collapse into this state. The polar centers of the v-av lattice then annihilate, leaving the disc with a single vortex reversed chirality relative to its initial state.

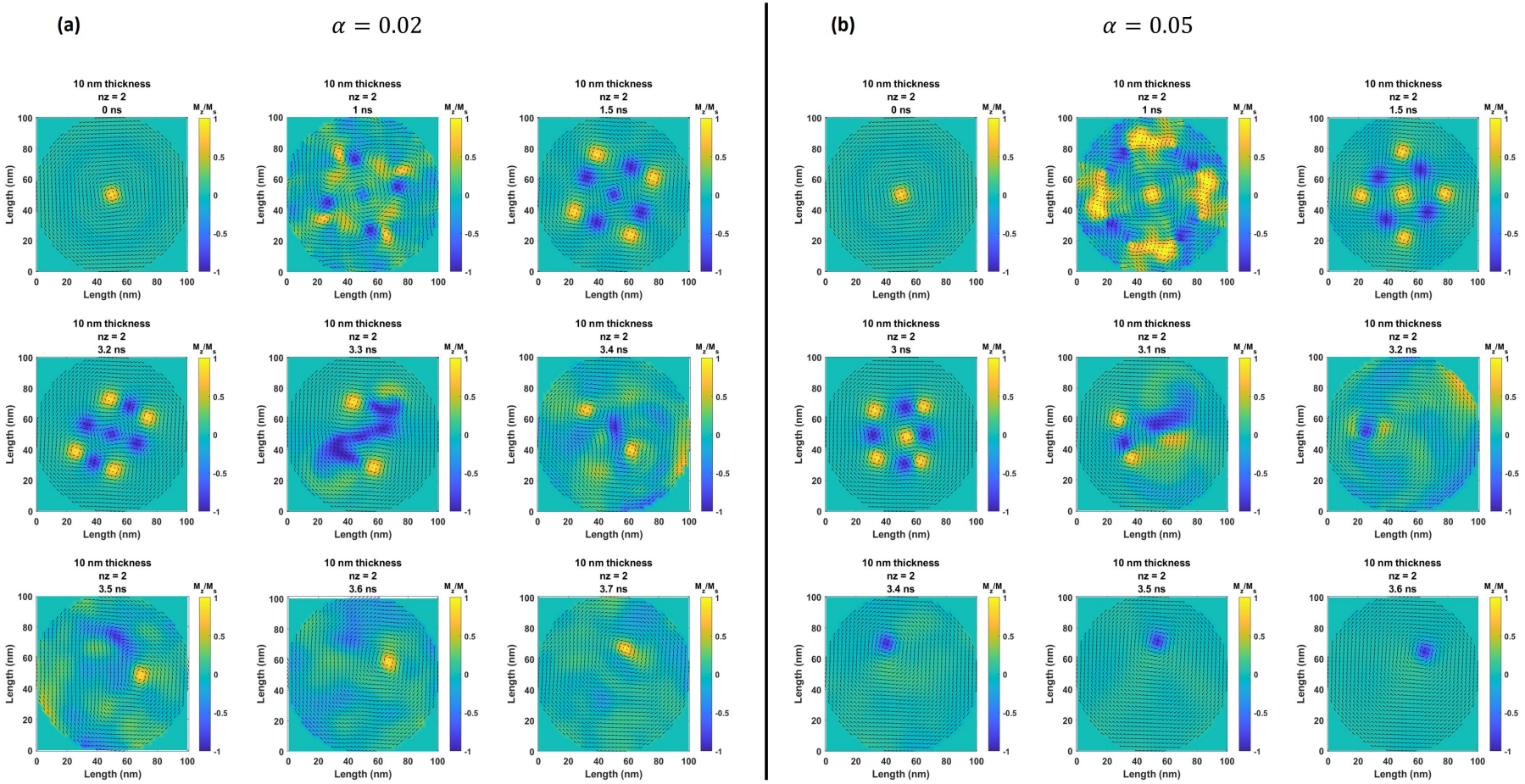


**Figure 3.23** The effect of damping constant $\alpha$ on the dynamics of the v-av lattice as a transient state during switching of the 10 nm disc under the pulse provided in Fig. 3.12(a). (a) $\alpha = 0.02$ and (b) $\alpha = 0.05$.

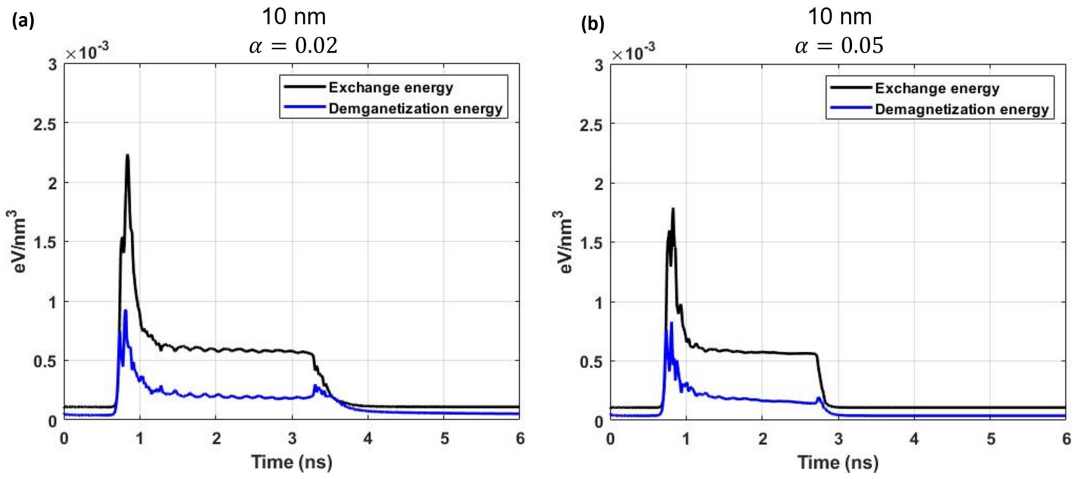


**Figure 3.24** The effect of damping constant $\alpha$ on the exchange and the demagnetization energies of the v-av lattice as a transient state during switching of the 10 nm disc under the pulse provided in Fig. 3.12(a). (a) $\alpha = 0.02$ and (b) $\alpha = 0.05$.

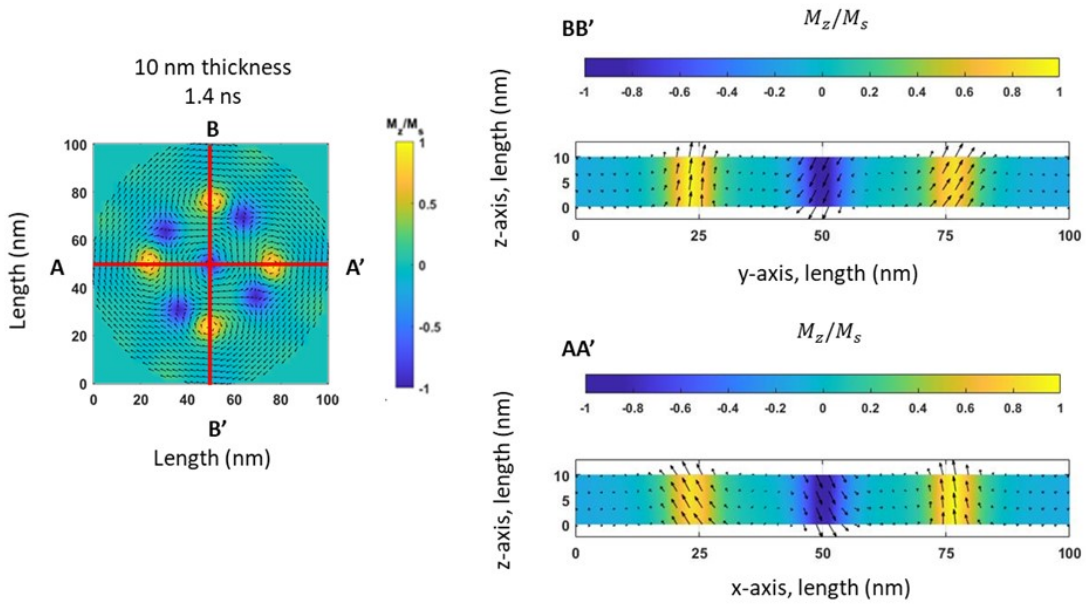


**Figure 3.25** Left panel: 2D arrows with directional components of magnetization superimposed on color map of Mz component. Right panel: The magnetization vector field superimposed on color map of Mz component along the cross sections (AA') along the x-axis, (BB') along the y-axis for the 10 nm thick disc.

### 3.7 Demagnetization effect on chirality reversal

Motivated by the above discussion in Section 3.5 on the effect of the disc thickness regarding the effect of the demagnetization field acting as an energy barrier to chirality reversal, we plotted the component of the demagnetizing field in the 20 and 10 nm thick discs across the thickness in Fig. 3.26 for the respective ground states (not the v-av lattice state, which is a transient state during chirality reversal of the 10 nm thick disc). Fig. 3.26(c) and (d) present the values of the demagnetization field along the diameter of the disc along the x-axis for the top and the center layer during relaxation, which clearly show that the thin disc acquires higher demagnetization energy near the center, almost 4 times higher than the thick disc. Indeed, the overall demagnetizing field in the 10 nm disc is higher than the 20 nm one, which also tempts us to think of it as the main obstacle to the ease of chirality reversal. Despite a vortex state being composed of magnetic moments primarily configured in the disc plane, i. e., along the x-y axes, an increase in the z-component of the magnetic moments is expected when the chirality switches under an applied field. With this increase in the z-component of magnetic moments, there will be an increase in the demagnetizing field particularly at the top/bottom surfaces that result in a resistance to reversal, manifested via a cost of additional demagnetization energy to the system. If the external field is insufficient, no reversal will occur as shown in Fig. 3.20(c). The thicker disc experiences lower transient demagnetization energy during chirality reversal and overcomes this field at a relatively lower energy cost than the 10 nm disc. The 10 nm disc forms the v-av lattice with the alternating polarity between v and av centers followed by the transition into the opposite chirality state that could, in principle, allow for circumvention of the strong demagnetizing effect due to thickness. Indeed, the demagnetization energy for this v-av state is lower than that of the initial reversal process (the first peak indicating that reversal has started in Fig. 3.20(d)). A counterargument, on the other hand, could be that the v-av lattice should have formed in the early stages of reversal to be considered as an easy path instead of being an intermittent state occurring when the spiral-like state appears in the first moments of switching that coalesces, forming eventually the v-av lattice. Nevertheless, this is a thickness driven occurrence and is not observed in the thicker discs considered herein and warrants further study for a precise understanding of its origins.

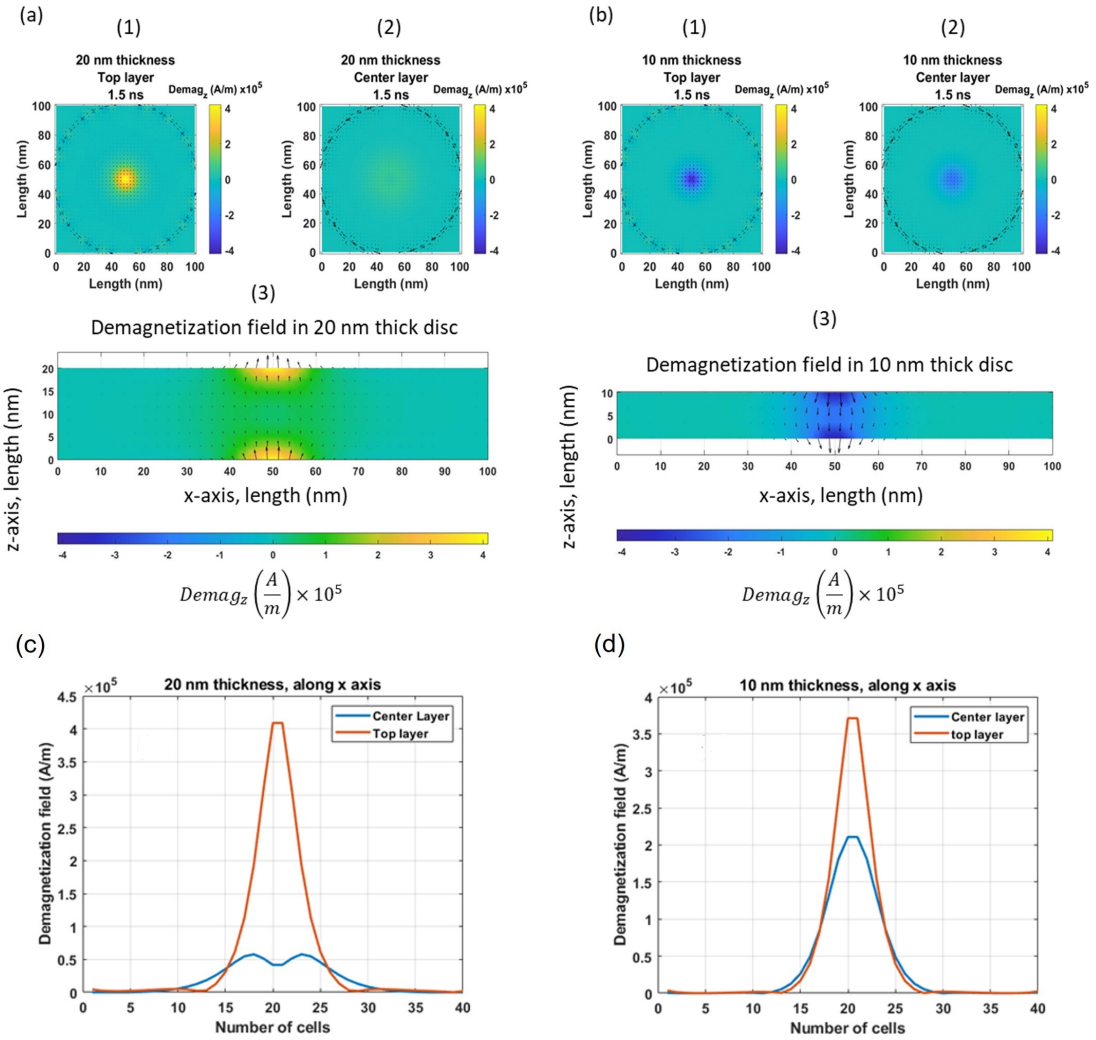


**Figure 3.26** (a) The demagnetization field in 20 nm thick disc in (1) xy-plane top layer, (2) xy-plane center layer, and (3) zx-plane cross section of the disc. (b) The z component of the demagnetization field in 10 nm thick disc in (1) xy-plane top layer, (2) xy-plane center layer, and (3) zx-plane the cross section of the disc. Demagnetization field along the diameter of the disc along x-axis in the center and the top layers for (c) 20 nm thick disc (d) 10 nm thick disc.

### 3.8 The effect of disc diameter on chirality and polarity reversal

Increasing the disc diameter can allow one to reduce the pulse amplitude in order to obtain the same magnetic field distribution with B being around 0.8 T near the periphery. This is due to the linear spatial dependence of the field inside the disc as a function of disc radius (See Eqn. 2.44). Moreover, the reversal process starts from the disc periphery (due to the additional surface energy in these regions and

that the field strength is the highest along the periphery). Please check Fig. 3.27 for the effect of disc diameter on the amount of current to be passed to achieve a 0.8 T magnetic field at the disc periphery for 3 different diameters.

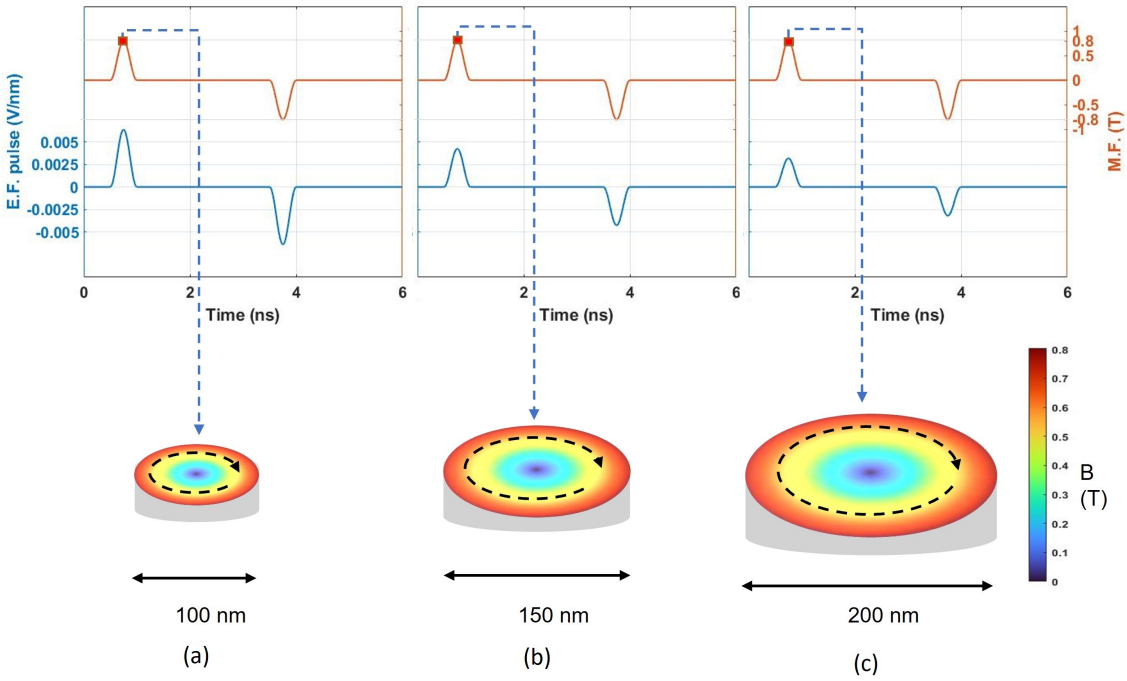


**Figure 3.27** Electric pulse and the magnetic field distribution as a function of disc diameter for (a) 100 nm, (b) 150 nm, and (c) 200 nm.

Similar to presented in Fig. 3.13, possible Joule heating magnitudes were also obtained from Eqn. 2.45 in Ref. [110] for the discs above having different diameters in response to the pulses shown in Fig. 3.27. These results are given in Fig. 3.28. A larger disc diameter requires less amplitude which also aids in a more efficient loss of heat that arises as a result of Joule heating.

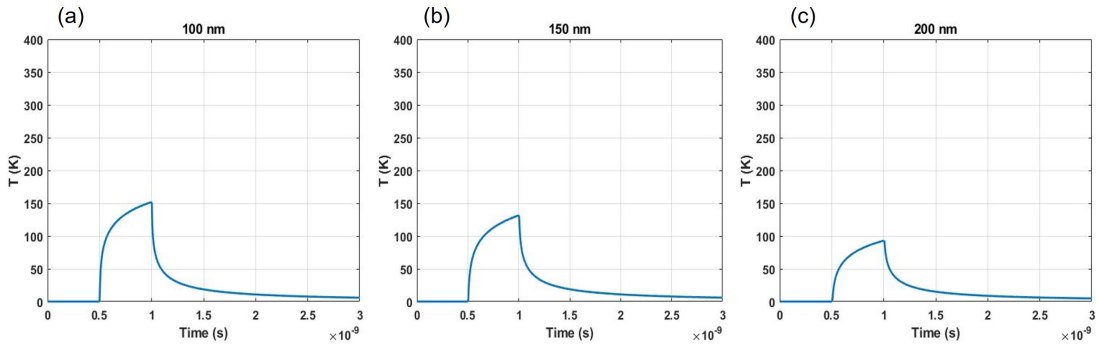


**Figure 3.28** Temperature evolution as a function of time during the application of the pulse given in Fig. 3.27 for discs with 10 nm thickness and different diameters (a) 100 nm, (b) 150 nm, and (c) 200 nm.

Going further with the analysis of the disc diameter effect, we provide the energy density results obtained from these simulations are shown in Fig. 3.29. Clearly, by increasing the diameter of the disc and under the same induced magnetic field distribution given in Fig. 3.27, one can obtain a chirality switching in 150 nm and 200 nm discs compared to the case of the 100 nm diameter disc where no reversal has occurred. (See Fig. 3.29 (a,c, and e)). However, in 10 nm thick discs there is no significant change in energy barriers between 150 nm and 200 nm as shown in (c) and (e). Increasing both the diameter and the thickness reduce fluctuations as well as the demagnetization energy (See Fig. 3.29 (b, d, and f)), increasing the stability of the magnetic order (this is in fact the well-known size driven effect). The 20 nm thick 100 nm, 150 nm, and 200 nm discs undergo chirality reversal for the same pulse amplitude but one should keep in mind that the greater the disc diameter, the greater the field near the disc periphery, meaning that easier reversal is possible. Therefore, weaker induced magnetic fields could be possible to use to initiate switching (via weaker currents or smaller pulsed field amplitudes, See. Eqn. 2.44) for larger discs. One can also note that with increasing diameter of the disc (for 20 nm thickness) the exchange energy peak becomes more dominant than the demagnetizing field: The reason for this is that the magnetic field gets stronger near the disc periphery for large diameters, inducing a more pronounced magnetism on the moments, causing deviation from the parallel ordering of the moments, eventually increasing the exchange contribution (as this energy imposes almost-parallel ordering of moments and during switching this order momentarily disappears, resulting in an increase of this energy term). The demagnetization field is relatively reduced again emanating from the tendency of the majority of the magnetic moments to lie in the plane for larger diameter discs. The demagnetization energy always yields a peak in proportion to the amount of magnetic moment rotation whose normal component transiently intersects the disc plane, generating a discontinuity in the magnetic induction, which in turn causes the appearance of the demagnetization field, hence the demagnetization energy. This energy is relatively smaller in larger diameter discs (such as the 150 nm and 200 nm ones). For smaller diameter discs, due to the size effect, a greater oscillation of the z-component of the magnetic moments is recorded (See Fig. 3.30 (a)), which in turn causes a greater demagnetization energy peak during switching relative to the exchange peak. Note that the demagnetization energy also oscillates as a result of the z-component of the magnetic moment fluctuation, providing another argument for the size-driven amplification of the demagnetization field. The z-component oscillations of the 150 nm and 200 nm diameter discs are profoundly less significant as much of the "reorientation processes" occur along the x- and y-components of the magnetic moments. In fact, that disc diameter influences the manner in which the moments respond to

the induced magnetic field is an important conclusion reached.

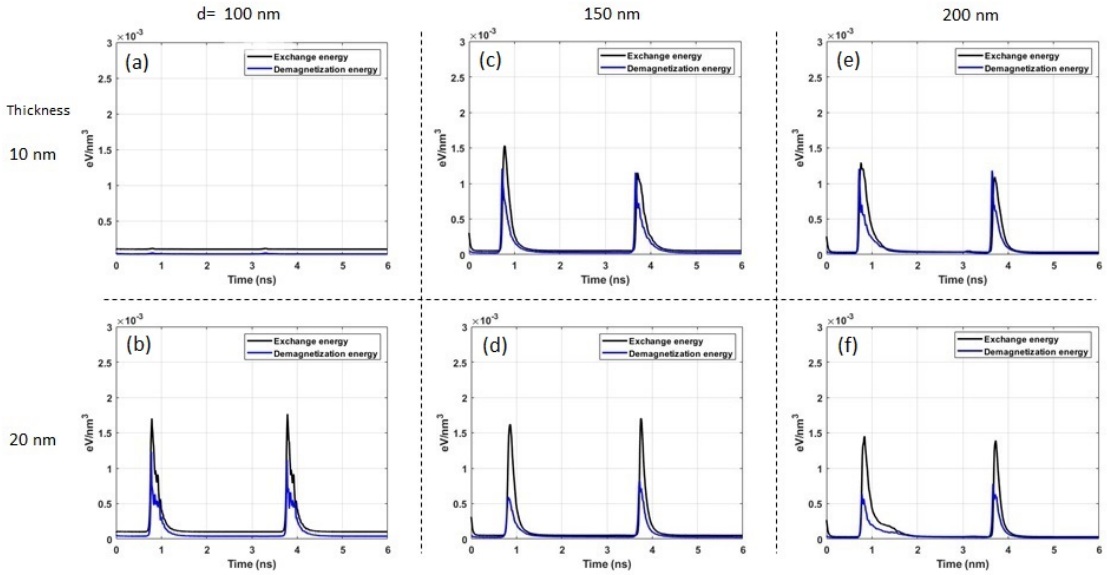


**Figure 3.29** Comparison of the exchange and demagnetization energy terms in left panel: 100 nm in diameter discs (a) 10 nm thick disc, (b) 20 nm thick dics, center panel: 150 nm in diameter discs, (c) 10 nm thick disc, (d) 20 nm thick dics, right panel: 200 nm in diameter discs, (e) 10 nm thick disc, (f) 20 nm thick dics.

As can be seen from Fig. 3.30, increasing the diameter of the disc allows the magnetic moments a higher freedom to stabilize in the plane of the disc. During the switching process, the formed vortex core with reversed chirality gyrates around the symmetry center, causing a magnetization wave with time shown as the components mx (blue curve) and my (black curve) (Fig. 3.30(b) bottom row). The magnetization wave amplitude depends on the gyration orbit. If a vortex core nucleates far away from the symmetry center the magnetization wave is large and it would decay when the vortex core approaches the symmetry center. After the second excitation with the second pulse, we clearly see that the newly formed vortex core with reversed chirality is nucleated near the center, therefore, a small magnetization wave is observed (See Fig. 3.30 (b, c) bottom). The gyration orbit is shown in Fig. 3.31, under the first pulse the formed core is far away from the symmetry center and a large gyration orbit is observed which agrees with the magnetization wave amplitude (See Fig. 3.30 (c) bottom). After the second pulse, a random configuration is observed (see Fig. 3.31(b) 3.8 ns). Later, a newly nucleated vortex core is emerged at 3.9 ns close to the symmetry center with a small gyration orbit. The magnetization oscillations along the z-axis are also decreased with increasing disc diameter as shown in Fig. 3.30 (b, c) top.

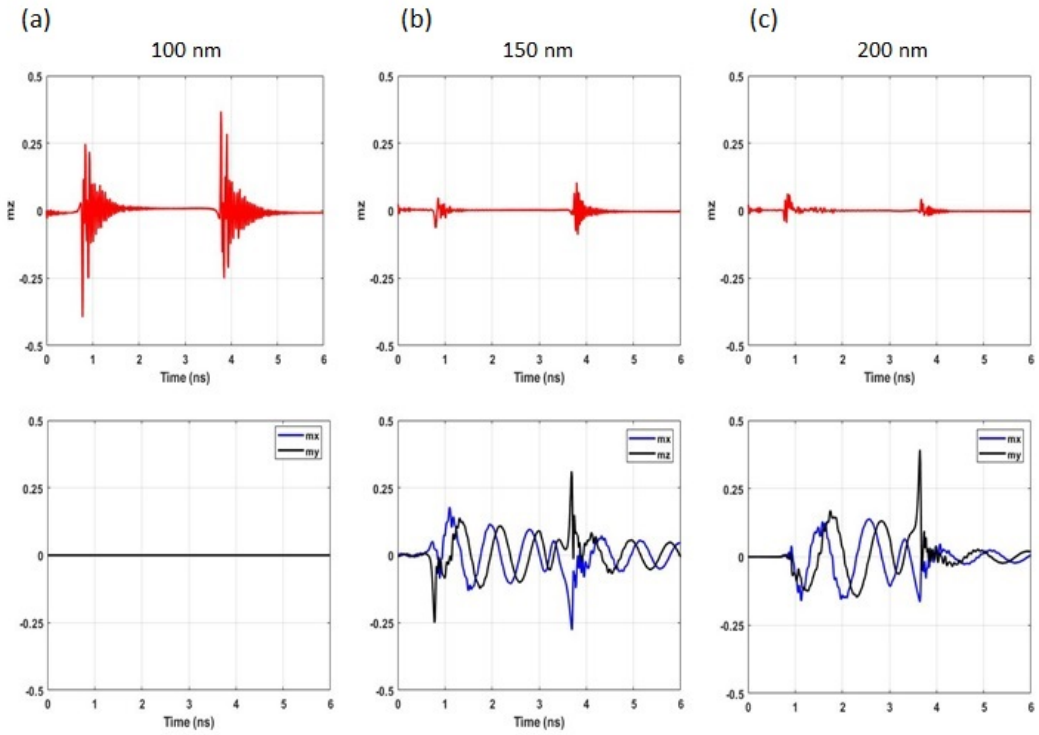


**Figure 3.30** The average of the magnetization components mx (blue), my (black), and mz (red) in 20 thick discs in (a) 100 nm in diameter disc, (b) 150 nm in diameter disc, and (c) 200 nm in diameter disc.

Fig. 3.32 shows the phase diagram of different size PY discs under the effect of two pulses sequence separated by 2 ns that generate an Oersted field provided in Fig. 3.27. In total there are eight simulations of different disc sizes for different combinations of diameters and thicknesses. The vortex chiralities have switched under the effect of two pulses given in Fig. 3.27 for most cases, except the disc with 10 nm thick and 100 nm diameter. On the other hand, the polarities of the vortices got affected mostly by the second pulse, whereas, new vortices with opposite cores settle in the disc center. We detected nucleation of multiple cores of vortices and antivortices with different polarities (See Fig. 3.32 snapshots). Although, the other switching processes show negative and positive polarity, however, there was no evidence of vortex core formation that has both chirality and polarity.

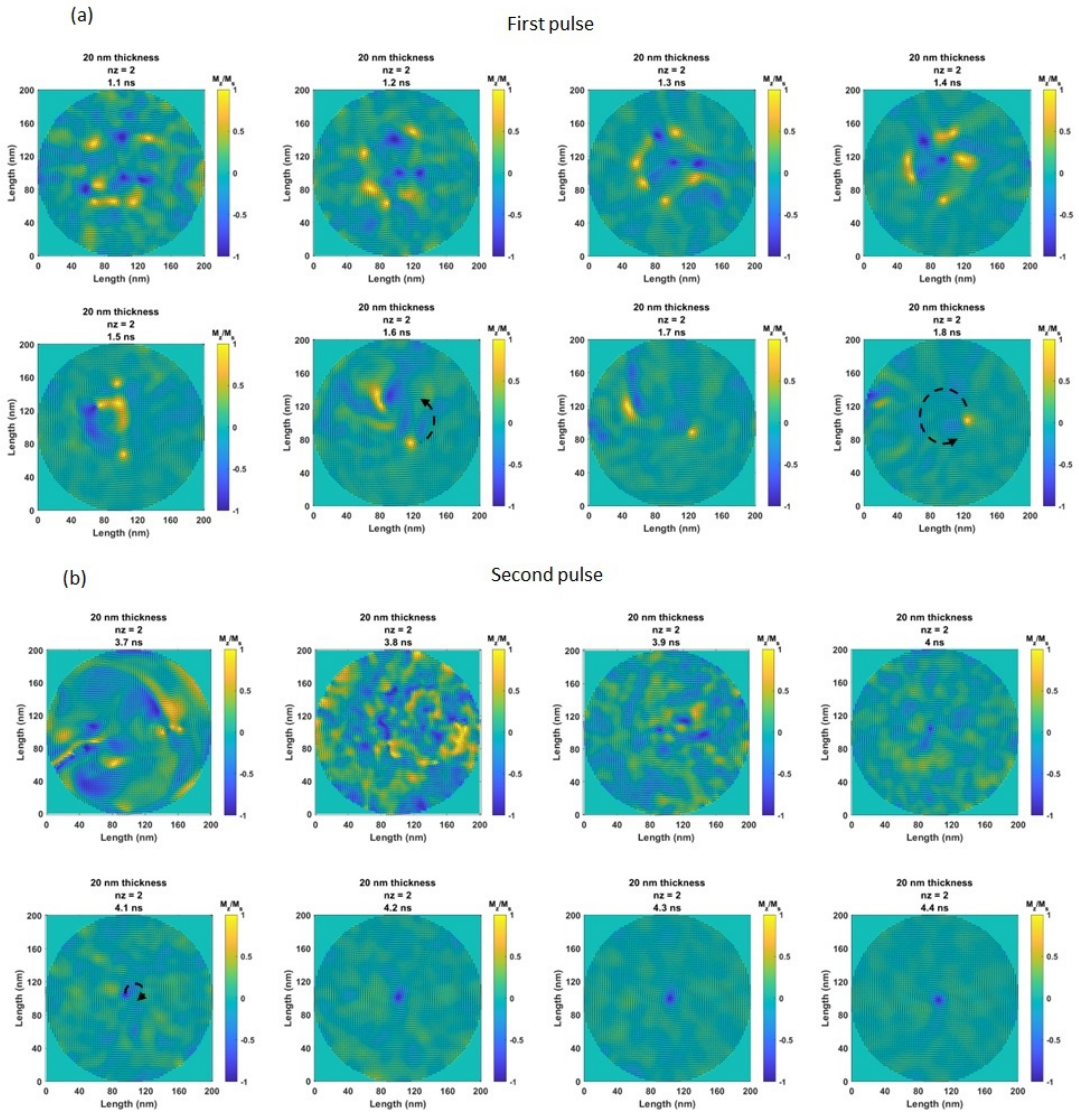


**Figure 3.31** The magnetization vectors superimposed on a colormap of the z component of the magnetization showing the effect of pulses given Fig. 3.27(c), the black arrows represent the gyration orbit of the newly formed core (a) between the first and the second pulses and (b) after the second pulse.

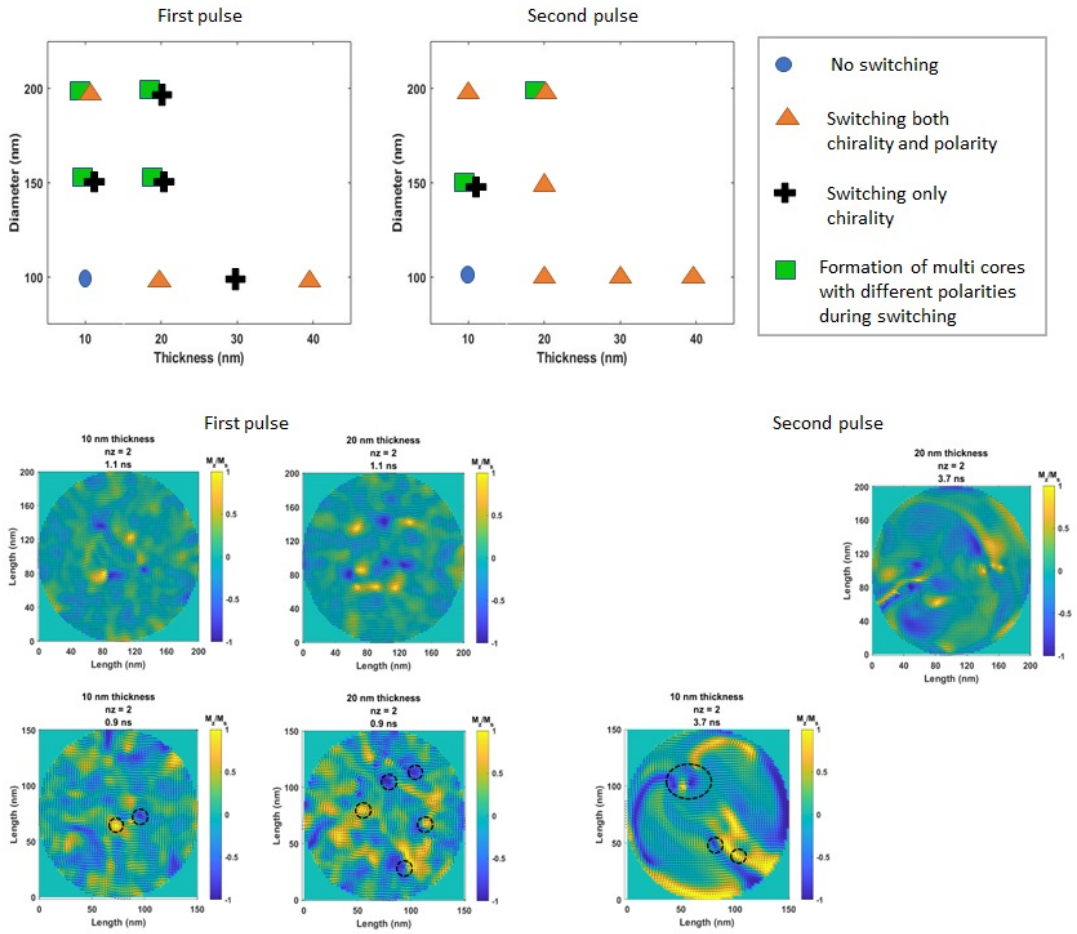


**Figure 3.32** Phase diagram of different size PY discs under the Oersted field distribution given in Fig. 3.27. The phase diagram shows the chirality and polarity switching, no switching, and multi vortex cores formation as function of PY discs' diameter and thickness. The snapshots were taken for different discs during the switching processes show the formation of multi vortex cores, the instantaneous time, diameter, and thickness are indicated on the snapshots.

### 3.9 The spin torque effect on chirality and polarity reversal

Here, we study the spin dynamics of the PY nanodiscs. The diameters of the PY discs are fixed at 100 nm and the thickness varies from 10 to 40 nm. The initial state is a vortex state with ([C, P] = [+1,+1]). The current is applied along the z direction and the spin polarization is along the z (+z) direction when positive (negative) current is applied as shown in Fig. 3.33(a). The dc current induces an in-plane Oersted field. Also the current produces a torque that tends to align

the magnetization vector toward the polarization direction, this effect is known as the spin torque effect (STT). In our simulation, we consider both effects. We use OOMMF code to conduct the simulations [2]. We solve LLGS Eqn. 2.8 which has an additional Slonczewski STT term [102]. P is the degree of spin polarization, and here, we consider P = 0.7 [120]. Material parameters for PY $Ni_{50}Fe_{50}$ are $M_s = 1.11 \times 10^6$ A/m, $A = 5.85 \times 10^{-12}$ J/m, $l_{ex} = 2.76$ nm and $\alpha = 0.02$. Magnetic anisotropy for the composition of interest here is negligibly small and is not considered [109, 114]. The cell size is $2.5 \times 2.5 \times 2.5$ $nm^3$. In this simulation, we apply an out-of-plane spin polarized current with a maximum current density of $\approx 5 \times 10^{12}$ $A/m^2$ and the duration of the pulse is 0.1 ns (See Fig. 3.33(b)), this current would induce an in-plane Oersted field with a maximum B value equal to $\approx 0.16$ $T$ (See Fig. 3.33(a)). Possible Joule heating magnitude is also obtained from Eqn. 2.45 (See Fig. 3.33(c)) for a PY disc of 100 nm in diameter and 10 nm in thickness in response to the pulse shown in Fig. 3.33(b).

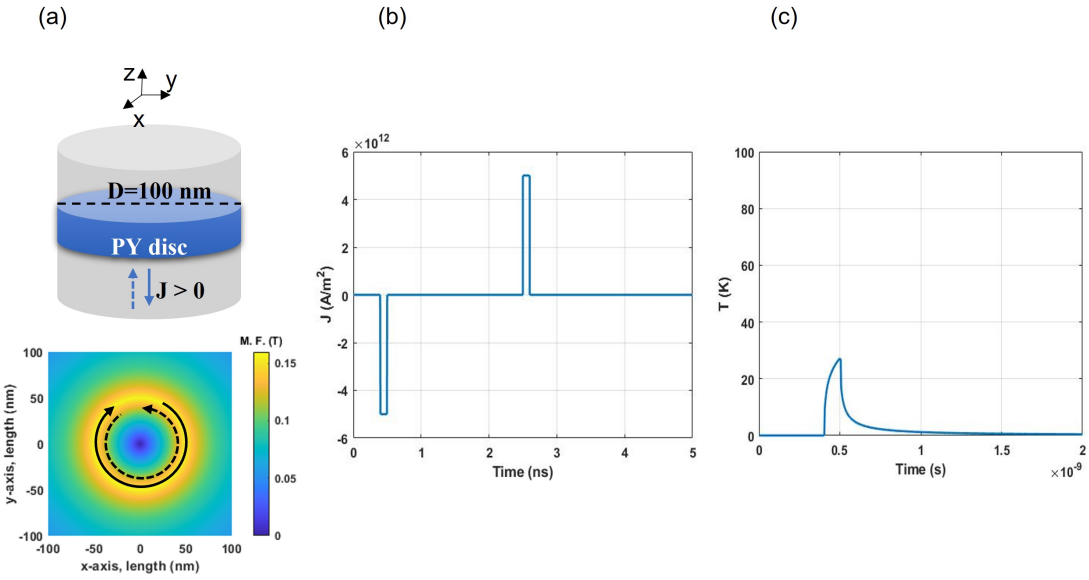


**Figure 3.33** (a) The model system is illustrated. The blue solid and dotted arrows denote the current direction when a negative (positive) current is passing through the system, respectively. The colormap represents the strength of the Oersted field as a function of distance in XY-plane, the solid arrow and dotted arrow denote direction of the magnetic field induced by a negative (positive) current, respectively. (b) The dc current density sign, value and duration. (c) Temperature evolution as a function of time during the application of the first current pulse given in (b).

The chirality and polarity response of the 10, 20, 30, and 40 nm thick discs to the electrical pulses are provided in Fig. 3.34. Upon application of the pulsed electric current in Fig. 3.33(b), the thinner 10 nm disc undergoes a reversal process as tracked via the chirality and polarity displayed in Fig. 3.34(a) and a metastable

(multi vortex-anti-vortex cores with a chirality value equal to ≈ -0.35) state is observed after the first pulse. On the other hand, the thicker discs 20 nm and 30 nm undergo chirality reversal but not polarity during the first pulse, however, the second pulse induces polarity reversal but not chirality. In the 40 nm, both chirality and polarity did switch after the first pulse, nonetheless, only the polarity did switch back after the second pulse. We attribute these differences to unstable states obtained after applying the first pulse.

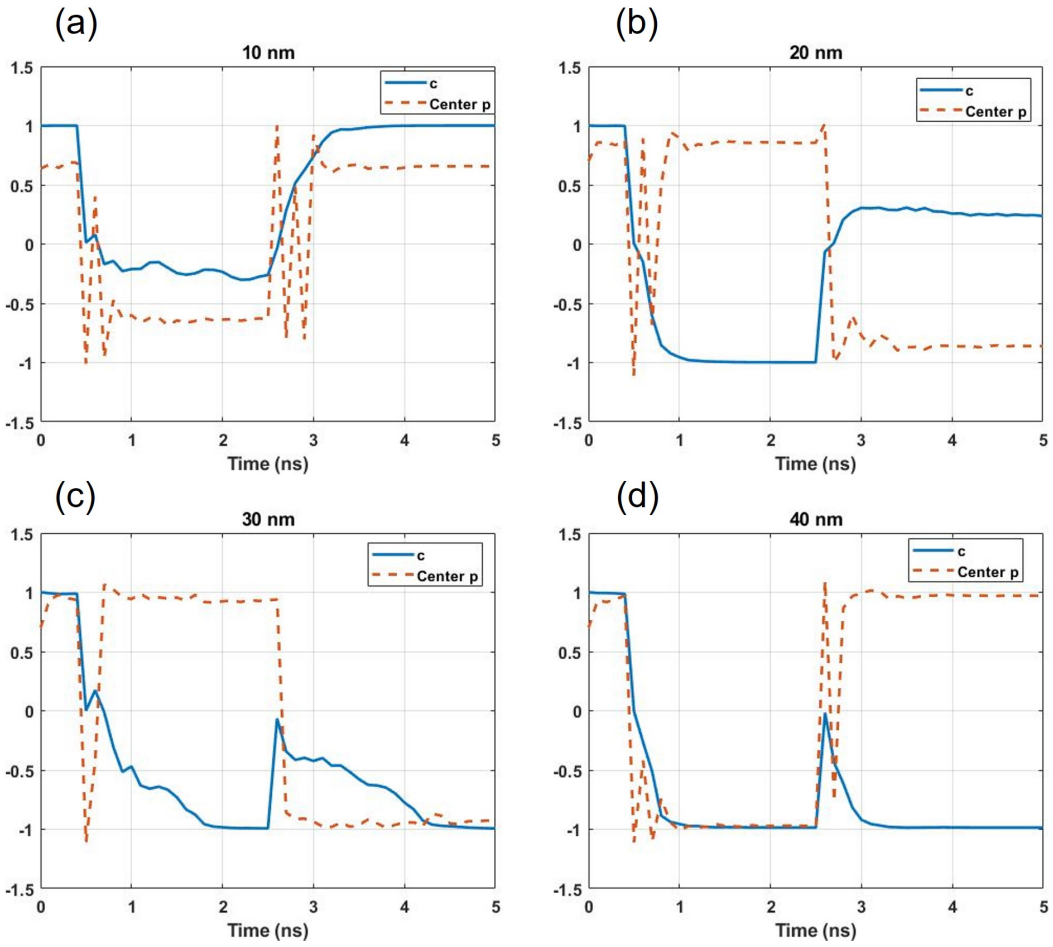


**Figure 3.34** Chirality and polarity of the PY discs of 100 nm in diameter in response to the pulses given in Fig. 3.33(b) for different thicknesses: (a) 10 nm, (b) 20 nm, (c) 30 nm and (d) 40 nm.

Concurrent with the simulation, we computed and tracked the various energy terms in Eqn. 2.9. The exchange and the demagnetization energy terms of the four discs are plotted in Fig. 3.35 during this process. The peak in the demagnetization energy is due to the STT tending to align magnetization towards the spin polarization direction, in this case, it is out-of-plane. Therefore, magnetic poles form along the top/bottom surfaces during the reversal process which induces high demagnetization energy. The magnitude of the barrier to the reversal in the 10 nm thick disc is greater

than that of the thicker discs. Here we notice also that the peak in exchange energy appears after some time from the formation of the demagnetization energy peak. The reason behind that is the magnetic dipoles align in an organized way with the spin polarization direction, then the dipoles want to relax after removing the current. Therefore, the exchange energy arises when the dipoles deviate from the parallel alignment.

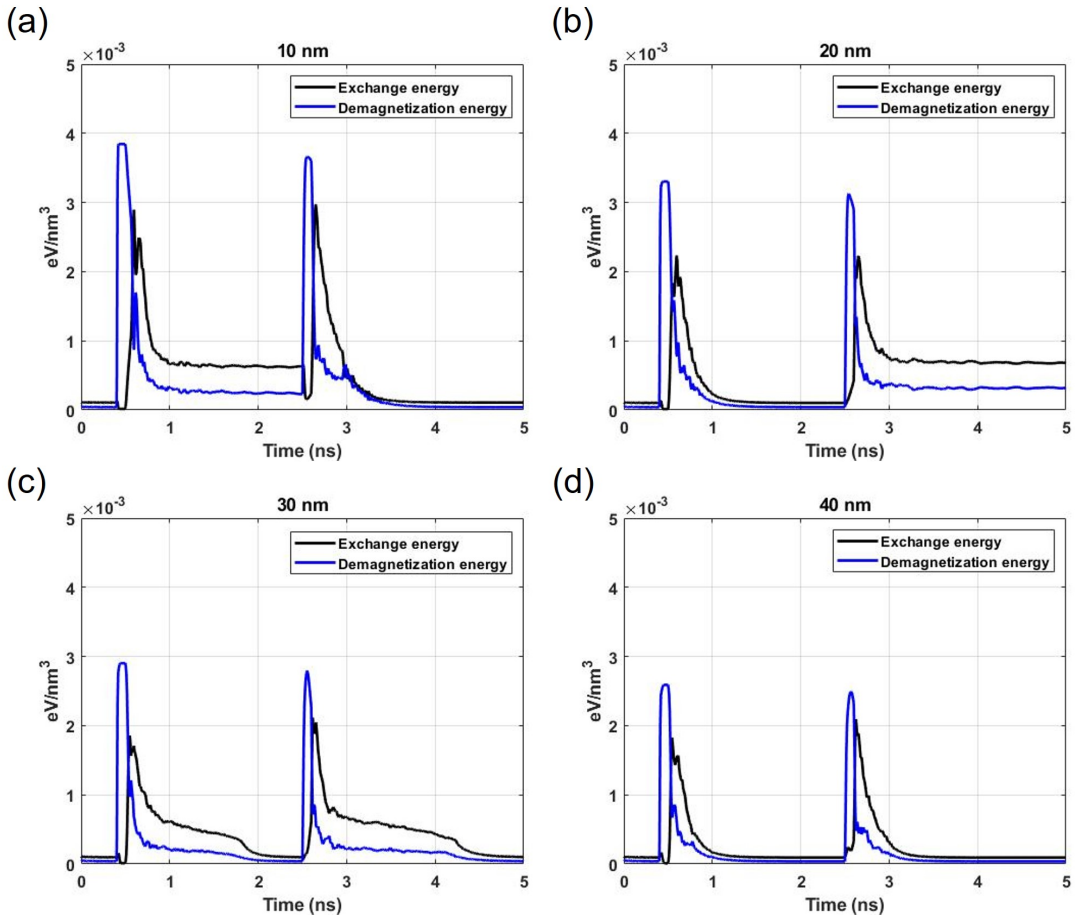


**Figure 3.35** Comparison of the exchange and demagnetization energy terms in (a) 10 nm thick disc, (b) 20 nm thick disc thick, (c) 30 nm thick disc, and (d) 40 nm thick disc under the pulses provided in Fig. 3.33(b).

Fig. 3.36 left panel shows the magnetization vector maps superimposed on mx colormap, these snapshots illustrate the chirality state before and after the effect of the first current pulse. The chirality state did switch within 0.5 ns for both 20 nm and 40 nm thick discs. It is not the same for 10 nm and 30 nm, both form metastable states.

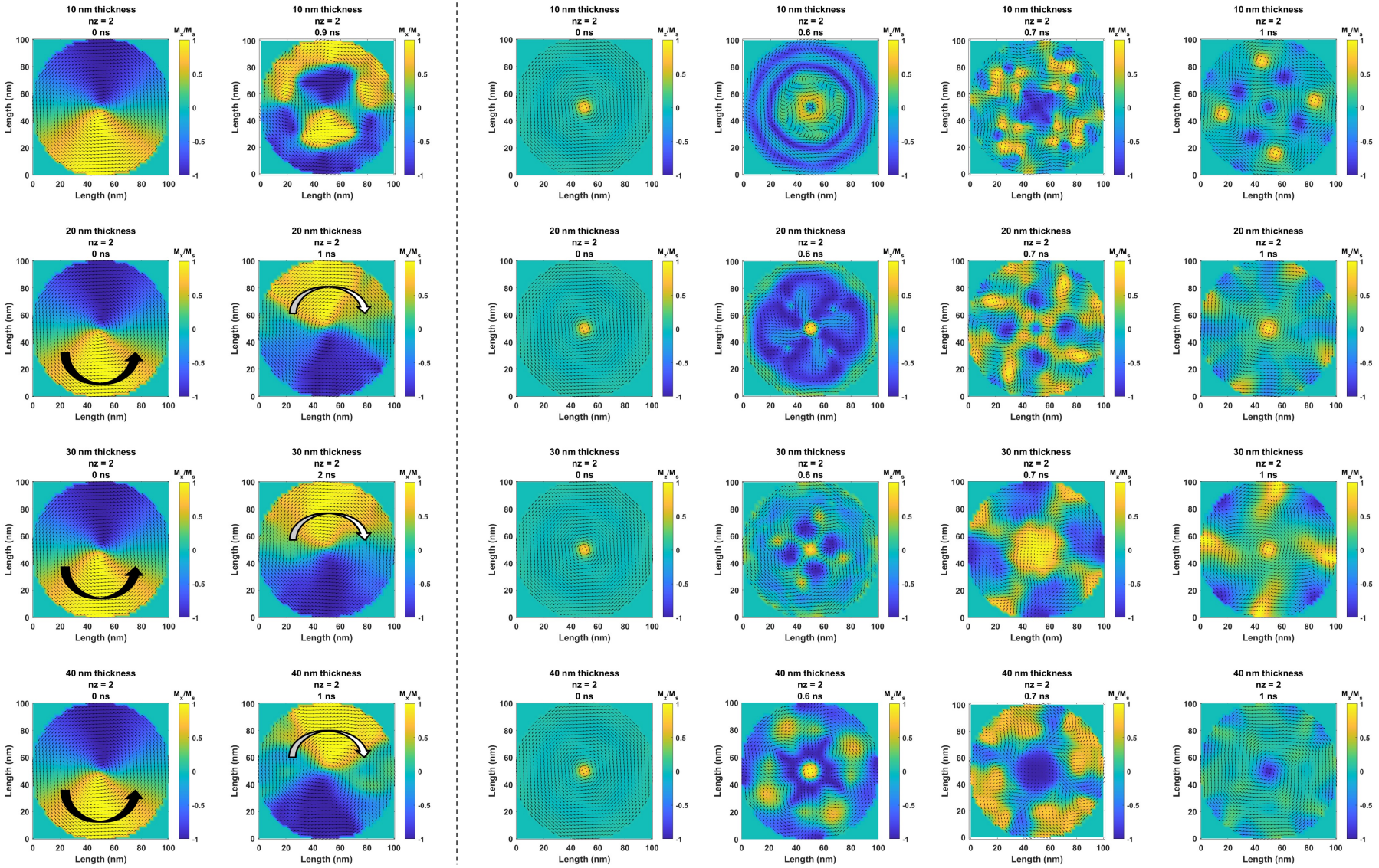


**Figure 3.36** The magnetization vector maps of nanodiscs with different thicknesses superimposed on mx component which reveal information about the chirality state (the left panel), mz component which reveal information about the polarity state and the transient states (the right panel).

Eventually, these metastable states switch to a single vortex state. Fig. 3.36 right panel shows the polarity maps during the switching process. Interesting transient states and the formation of vortex -antivortex lattice are observed.

### 3.10 Thermal field effect on chirality reversal

The micromagnetic simulations are performed using OOMMF code [2]. The Xf-ThermHeunEvolve extension is used to allow the simulation of thermal fluctuation effects on a magnetic ensemble using Heun's method [121]. The thermal fluctuations can be modeled as an effective field derived by Brown, see Eqn. 2.46 [122]. PY $Ni_{50}Fe_{50}$ nanodisc having 100 nm diameter with 20 nm thickness is considered. Material parameters for PY $Ni_{50}Fe_{50}$ are $M_s = 1.11 \times 10^6$ A/m, $A = 5.85 \times 10^{-12}$ J/m, $\lambda_{ex} = 2.76$ nm, and $\alpha = 0.02$. Magnetic anisotropy for the composition of interest here is negligibly small and is not considered [109, 114]. The cell size is $2.5 \times 2.5 \times 2.5$ nm$^3$. Four simulations were conducted for four different temperatures: 0, 200, 300, and 400 $^0K$. The temperature is held constant during the simulation. If one considers a homogenous current density across the cross section of the disc, namely $J \approx 10^{13}$, one can obtain a maximum magnetic field of about $B_s \approx 0.7$ T at the disc periphery (See Fig. 3.37). Note here that the current density used in this section is less than the one used in Sec. 3.3. We also provide the chirality response (See Fig. 3.38) of PY nanodisc to the electrical pulse given in Fig. 3.37 for different temperatures. No switching was observed for both 0 and 200 $^0K$. Although, in 200 $^0K$ the vortex core was excited and did start gyrating around the disc center. At higher temperatures 300 and 400 $^0K$, the chirality did switch and a reversed state is obtained.

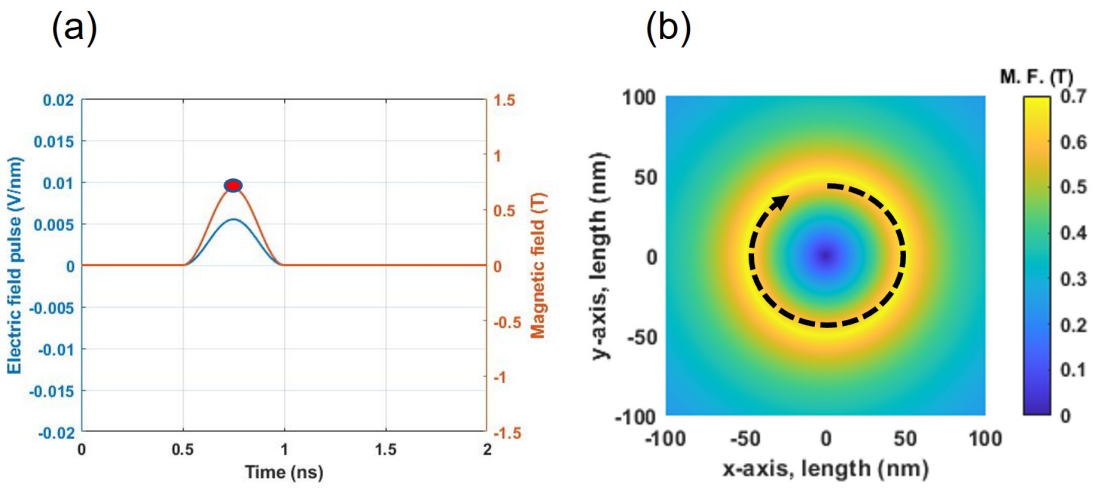


**Figure 3.37** (a) shows a time-varying ns electric current pulse with the accompanying form of the Oersted magnetic field along the disc periphery derived from Eqn. 2.44. (b) The spatial planar distribution of the Oersted field strength (units in Tesla), induced by the current flow of the indicated maxima (red dots) presented in (a)

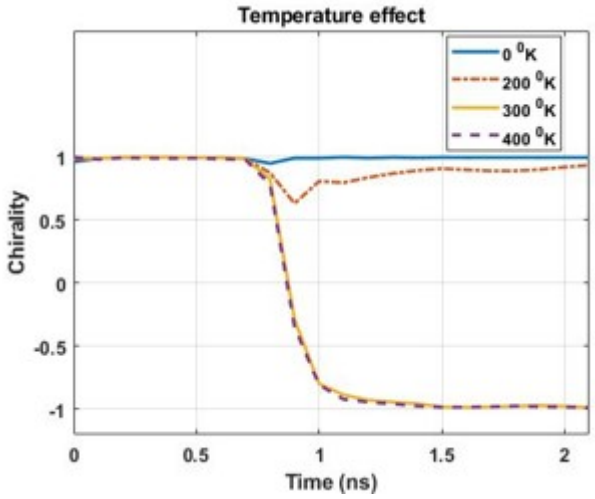


**Figure 3.38** Vortex chirality in response to the time dependent electrical pulses given in Fig. 3.37 for different temperatures.

In order to understand the dramatic difference in the response of PY nanodisc under different temperatures, we computed and tracked the various energy terms in Eqn. 2.9, focusing specifically on the exchange energy and the demagnetization term that arise from the system response to the external pulse and thermal fluctuations. At 0 $^0K$ the system is very stable, with no thermal fluctuations present. The exchange energy and demagnetization energy are approaching zero, and the Oersted field strength is not enough to induce switching (See Fig. 3.39(a)). Increasing the temperature to 200 $^0K$ will induce a random thermal field which forces the magnetic

moments to fluctuate, hence increasing the exchange energy due to the deviation of the magnetic moments from the parallel alignment. Although no switching in chirality is observed, the vortex core is excited and a core gyration is observed. Shallow peaks in exchange and demagnetization energies are observed during the vortex core excitation see Fig. 3.39(b). Increasing the temperature even more to 300 $^0K$ will increase the exchange energy to a level higher than that in 200 $^0K$. And the energy of the system is high enough that with the same field that is used at lower temperatures, a chirality switching can be induced see Fig. 3.39(c). Clear peaks in exchange and demagnetization energies are observed which indicate vortex state reversal. Increasing the temperature even more to 400 $^0K$ will increase the exchange energy a little more (see Fig. 3.39(d)), also a chirality switching is obtained. Fig. 3.40 shows the effect of the thermal field on magnetic moments, at 0 $^0K$ a very stable vortex state is obtained and no chirality reversal is observed. Increasing temperature, we clearly see the disorder in magnetic moments alignment which reduces the average magnetization. Also, it shows the chirality switching in 300 and 400 $^0K$ and vortex core gyration in 200 $^0K$. In fact, that thermal fluctuations influence how the moments respond to the induced magnetic field is an important conclusion reached, with high temperatures it is easier to induce chirality reversal. Also, it is important to keep the temperature of the nanodisc below Curie temperature, otherwise, the ferromagnetic ordering is lost and a random configuration is obtained. Therefore, the applied field (current, optical, laser, or Eddy current) and the induced thermal energy should not raise the temperature of the system near Curie temperature.

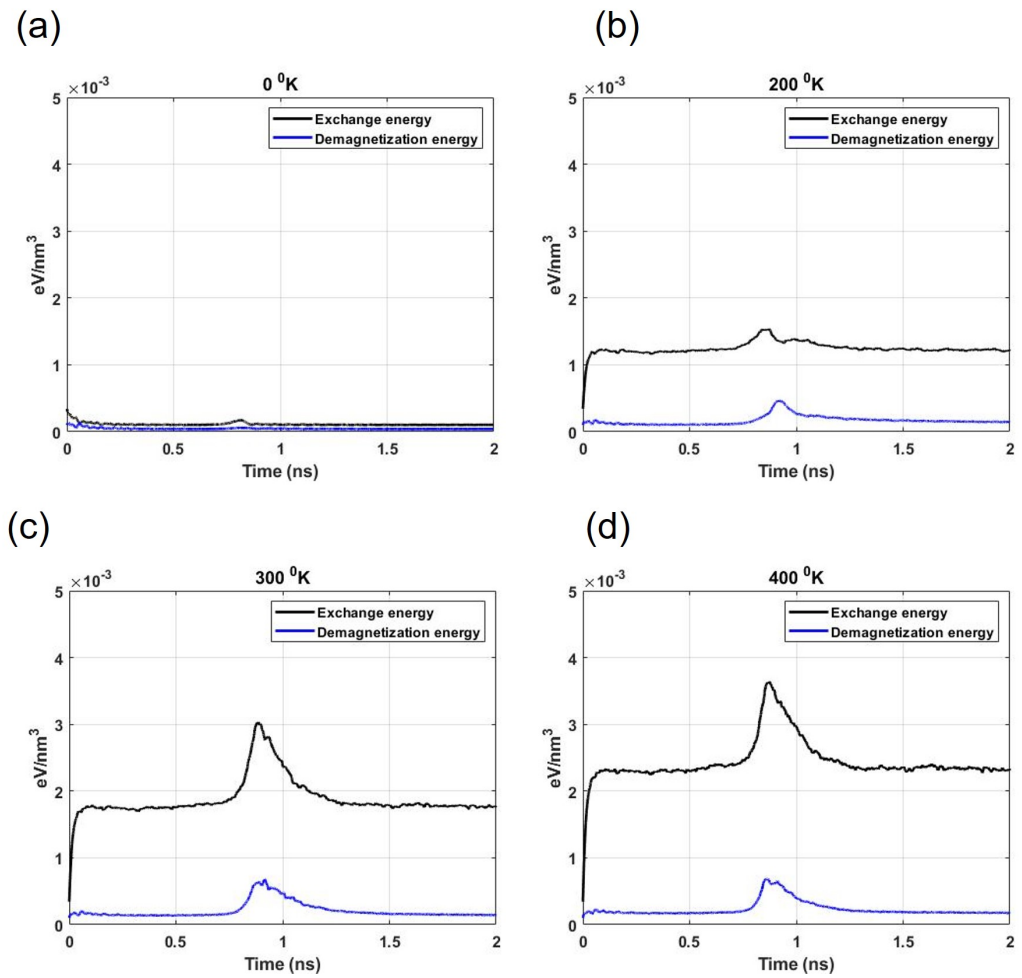


**Figure 3.39** Comparison of the exchange and demagnetization energy terms in PY nanodisc for different temperatures: (a) 0 $^0K$, (b) 200 $^0K$, (c) 300 $^0K$, and (d) 400 $^0K$.

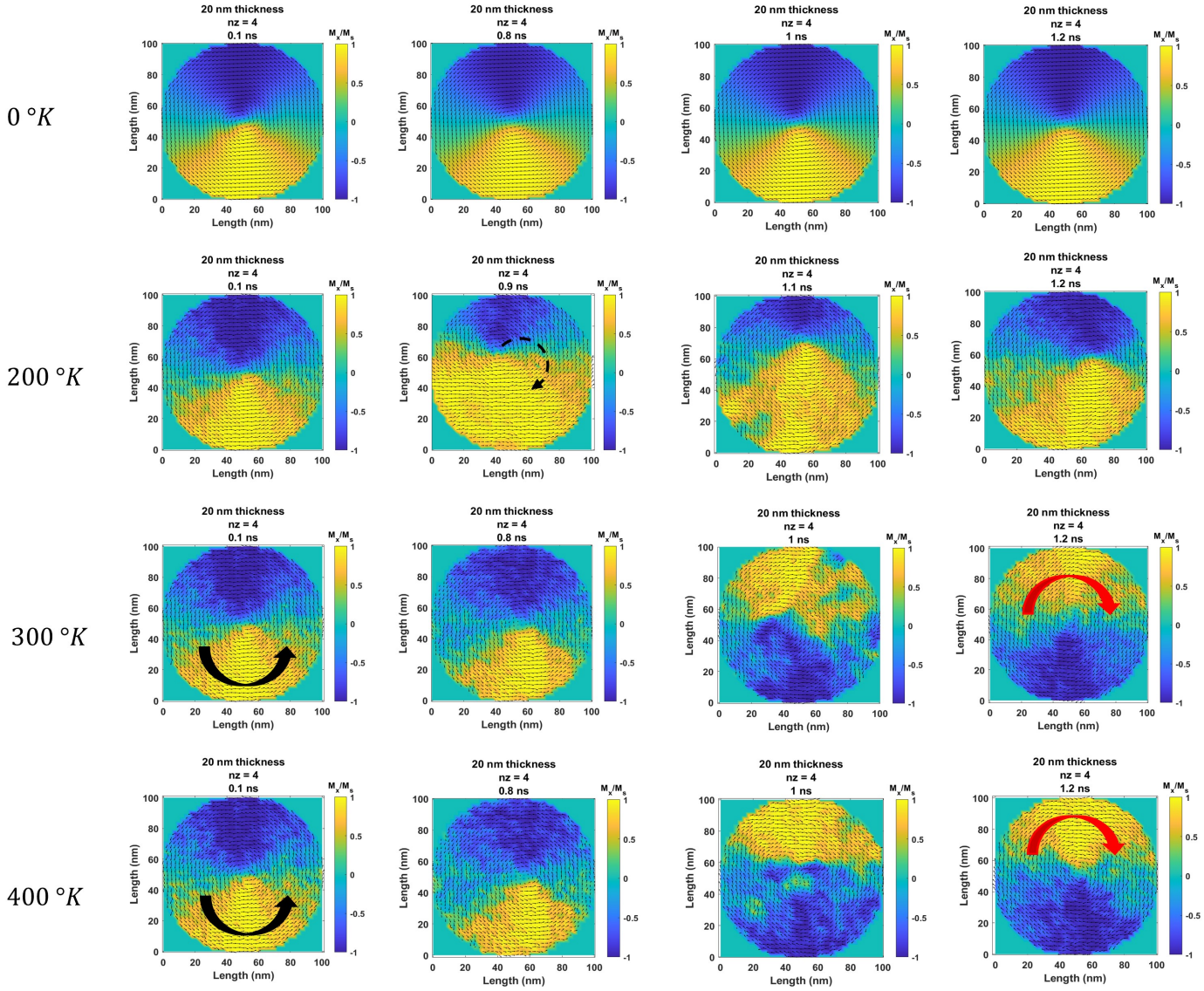


**Figure 3.40** Comparison of the magnetization vector maps in PY nanodisc for different temperatures: 0 $^0K$, 200 $^0K$, 300 $^0K$, and 400 $^0K$. The black doted arrow shows the gyration of the vortex core in 200 $^0K$. The black and red arrow show the sign of the chirality CCW and CW, respectively.

## 3.11 Applications

Micromagnetic simulations are important to understand the behaviour of modern data storage based devices and the research of novel materials and designs which could be incorporated into future devices. The computational resources can be used to provide a link between experiment and theory. Using computer simulations is important for two main reasons: First, it could be used to explain experimental results. Second, one can predict new designs for some components, and parts. Subsequently, new devices can be developed, hence reducing costs.

Storing data in a solid-state magnetic medium is one of the important parameters behind the computer technology revolution. Apart from data storage, spintronic applications where the spin of the electron is tailored rather than its charge in a transistor-like device have taken a new leap with nano-level processing of magnetic materials, paving the way towards faster and low power consumption devices. In the mid-1980s, the Giant Magnetoresistance (GMR) effect in multilayers composed of alternating ferromagnetic and non-magnetic conductive layers was discovered by Fert and Grünberg, tailoring hard drives based on utilizing this concept have made a huge contribution to computer technology. Sub-micron GMR layers have exhibited that the magnetization in a very small local magnetic layer on hard magnetic disks can be detected and manipulated, allowing for increases in hard disk drive data density. A while later after the discovery of the GMR effect, the "Colossal Magnetoresistance (CMR)" effect was discovered in some materials, mostly manganese-based perovskite oxides and materials exhibiting tunneling magnetoresistance (TMR) have been researched and tailored. TMR effect allows more powerful signals relying on spin polarization within the tunneling process in comparison with the classic GMR effect, this indicates that the new devices will be designed based on the previous principle.

Manipulating the magnetization that forms a vortex state in ferromagnetic nanostructures has become an interesting topic that gains considerable attention together with methods to design these structures with desired properties [33, 35]. The four states of a magnetic vortex allow for storing 2 bits instead of 1 bit of information in one single nanodisc. The curl magnetization ordering also minimizes the demagnetization field of each disc thus the interaction between neighboring discs. These properties make magnetic vortices attractive as information carriers. To store the information, a fast, repeatable, and robust transition between these four states is demanded. In this study, we did investigate the switching of both chirality and po-

larity, energy densities, geometry effects, core precession, thermal effects, and spin torque effect. The findings are important in spintronics applications.

# 4. Conclusions

We have demonstrated, using the LLG formalism, that a time-wise electric pulse with a critical amplitude and duration can be designed to induce chirality switching via electrodynamic coupling to the magnetic dipoles in the nanodisc within ns timescale. We tracked the degree of chirality in the nanodisc structure that allowed us to characterize the switching process. The chirality switching process occurs in 3 steps: First, the magnetization near the disc edge loses the order and switches into the opposite direction after coupling to the tangential magnetic field where the field amplitude is at its maximum. In parallel, a “chirality" ring appears to be nucleating from which a distinct new center forms that is attracted to the central “old" core. Finally, the old core disappears and the new one locates itself in the center. We also note that, during chirality switching, the polarity of the magnetic vortex can vary several times, and therefore the deterministic control of the polarity state appears to be difficult to control. In the case of an array of discs with some radial size distribution to perform a specific action such as memory storage, the needed pulse duration and amplitude depend on the area enclosing the electric flux intersecting the disc along the disc normal. Therefore, the dependency of the azimuthally induced magnetic field as a result of the time derivative of the electric flux needed to switch the chirality of a nanodisc could vary slightly.

We also studied the chirality reversal of ferromagnetic nanodiscs for different thicknesses. The simulations were carried out for a conducting permalloy disc and in the insulating limit. An Oersted magnetic field whose amplitude varies with radius is possible to achieve either via the consideration of a current flowing along the disc normal or a time varying electric flux, constituting the two origins of this magnetic field. Micromagnetic simulations are mainly carried out for the former whose results are presented. We analyze the thickness effect, which is a geometrical parameter in the stabilization of a vortex as the ground state, and find that it determines the ease with which the chirality of the vortex can be reversed under an electric pulse of the type discussed in this work. By tracking the exchange and demagnetizing energies of the two discs, we were able to show that the thinner discs have to overcome a

greater barrier to switching than the thicker ones. The thinner disc requires a pulse higher in amplitude and therefore a stronger Oersted field to undergo chirality reversal. This is an important result given that spintronic devices often function on the reversibility of the magnetic order of a ferromagnet. Moreover, during the chirality reversal of the thinner disc, a transient v-av configuration rotating about the disc center appears which then transitions into a single vortex state having a chirality opposite of the initial state. The polarity of the thinner disc remains the same as that of the initial state despite the chirality switching, unlike what is obtained in the thicker 20 nm disc. The polarity switching accompanies the chirality reversal in the 20 nm disc where the z-component of the magnetism experiences weaker demagnetizing fields along the disc normal than that of the 10 nm thick disc.

The disc diameter inherently becomes another factor in determining the threshold of the field required to initiate chirality reversal. Larger diameter discs, therefore, undergo chirality reversal at small pulse amplitudes or current densities as the reversal starts from the regions near the disc periphery where the induced magnetic field is maximum. This would, in principle, allow one to use weaker currents or electric pulse amplitudes to initiate chirality reversal given that the reversal process starts from the disc periphery.

Applying a polarized current induces a spin transfer torque effect which forces the magnetic dipoles to align with the polarization direction. This effect allows one to control the vortex state with less current density applied, however, deterministic switching is not realized and require different pulse durations and amplitudes for different aspect ratio.

We did also investigate Joule heating when a current is applied to the system, and how much heat is generated which is proportional to the square of the current density. Larger diameter discs allow us to use lower current density to induce switching, therefore, lower heat is generated. On the other hand, the Joule heating is proportional to the volume of the disc, therefore, smaller discs generate less heat if the same current pulse is used compared to the larger ones. We did incorporate the thermal fluctuations into the micromagnetic simulations, and we considered a constant temperature during the application of electrical pulses. The thermal field induces random vibrations in the magnetic moments, and these vibrations increase the exchange energy. One can utilize these vibrations to induce chirality switching by applying less current density.

The polarity-chirality coupling thus appears to be a function of thickness or aspect ratio in such nanostructures. Next to vortex stability, the aspect ratio of the nanodiscs is also an important parameter that determines the ease of reversal of the

chirality and the vortex core, a vital factor in data storage applications and new generation spintronic devices tailoring exotic states of magnetism.

# 5. Future work

We could investigate Dzyaloshinskii-Moriy's interaction at the interface between a ferromagnet and an oxide. The interface between heavy metals and a ferromagnet can induce different phenomena. These phenomena include perpendicular anisotropy, also known as Dzyaloshinskii-Moriya interaction (DMI). Although there are many experimental and theoretical publications regarding this topic, however, some areas are missing the physical explanation and need to be highlighted.

We could focus on the phenomenon of Joule heating and how the thermal energy profile generated by the current pulse passing through the magnetic layer affects the order of magnetic spins. Had the heating effects associated with currents been considered, which we estimated previously to range from a few tens of K to a few hundred depending on the disc aspect ratio and the substrate it is interfacing, chirality and polarity reversal can be expected to occur even at lower electric signals than what is predicted in this work. As Joule heating will increase the temperature of the disc and dominate the exchange field, vortex reversal would proceed at weaker Oersted fields.

We may also investigate the magneto-optical coupling in thin ferromagnetic films, and how the light scattering or reflection in a specific spectral range may be employed to detect the magnetization direction.

Another topic to take this study to another level is to investigate the magnetic skyrmions, which are achiral, or chiral solitonic quasi-particles that may exist both as dynamic excitations, and stable or metastable states on the sub-micrometer scale. Their stability and small size, skyrmions have been promoted as candidates for carrying information.

We will also try to investigate the antiferromagnetic and ferrimagnetic topological defects which are relevant for technological applications in several branches of condensed matter physics. Experimentally, skyrmions have been observed in ferrimagnetic thin films which have similar structures to some extent with antiferromagnetic. Theoretically, skyrmions could also appear in antiferromagnetic and a spin polar-

ized current can drive these features making them feasible information carriers for technological data storage applications.

## REFERENCES


[1] Zhu, R. (2015). Accelerate micromagnetic simulations with gpu programming in matlab. *arXiv preprint arXiv:1501.07293*.

[2] Donahue, M. J., & Donahue, M. (1999). Oommf user's guide, version 1.0.

[3] Landau, L. (1984). Electrodynamics of continuos media, landau and lifshitz. *Course of theoretical physics*, *8*.

[4] Abrikosov, A. A. (1957). On the magnetic properties of superconductors of the second group. *Sov. Phys. JETP*, *5*, 1174–1182.

[5] Hess, H. F., Robinson, R. B., Dynes, R. C., Valles, J. M., & Waszczak, J. V. (1989). Scanning-tunneling-microscope observation of the abrikosov flux lattice and the density of states near and inside a fluxoid. *Phys. Rev. Lett.*, *62*, 214–216.

[6] Yamada, K., Kasai, S., Nakatani, Y., Kobayashi, K., Kohno, H., Thiaville, A., & Ono, T. (2007). Electrical switching of the vortex core in a magnetic disk. *Nature materials*, *6*(4), 270–273.

[7] Hertel, R. (2013). Vortex states a la carte. *Nature nanotechnology*, *8*(5), 318–320.

[8] Konoto, M., Yamada, T., Koike, K., Akoh, H., Arima, T., & Tokura, Y. (2008). Formation and control of magnetic vortex chirality in patterned micromagnet arrays. *Journal of Applied Physics*, *103*(2), 023904.

[9] Levanyuk, A., & Blinc, R. (2013). Ferroelectric phase transitions in small particles and local regions. *Physical Review Letters*, *111*(9), 097601.

[10] Lee, B., Nakhmanson, S. M., & Heinonen, O. (2014). Strain induced vortex-to-uniform polarization transitions in soft-ferroelectric nanoparticles. *Applied Physics Letters*, *104*(26), 262906.

[11] Hanneken, C., Otte, F., Kubetzka, A., Dupé, B., Romming, N., Von Bergmann, K., Wiesendanger, R., & Heinze, S. (2015). Electrical detection of magnetic skyrmions by tunnelling non-collinear magnetoresistance. *Nature nanotechnology*, *10*(12), 1039–1042.

[12] Noske, M., Stoll, H., Fähnle, M., Gangwar, A., Woltersdorf, G., Slavin, A., Weigand, M., Dieterle, G., Förster, J., Back, C. H., et al. (2016). Spin wave mediated unidirectional vortex core reversal by two orthogonal monopolar field pulses: The essential role of three-dimensional magnetization dynamics. *Journal of Applied Physics*, *119*(17), 173901.

[13] Urbánek, M., Uhlíř, V., Lambert, C.-H., Kan, J. J., Eibagi, N., Vaňatka, M., Flajšman, L., Kalousek, R., Im, M.-Y., Fischer, P., et al. (2015). Dynamics and efficiency of magnetic vortex circulation reversal. *Physical Review B*, *91*(9), 094415.

[14] Uhlíř, V., Urbánek, M., Hladík, L., Spousta, J., Im, M., Fischer, P., Eibagi, N., Kan, J., Fullerton, E., & Šikola, T. (2013). Dynamic switching of the spin circulation in tapered magnetic nanodisks. *Nature nanotechnology*, *8*(5), 341–346.

[15] Wen, Y., Feng, Z., Miao, B., Cao, R., Sun, L., You, B., Wu, D., Zhang, W., Jiang, Z., Cheng, R., et al. (2014). Fast and controllable switching the circulation and polarity of magnetic vortices. *Journal of Magnetism and Magnetic Materials*, *370*, 68–75.

[16] Gaididei, Y., Sheka, D. D., & Mertens, F. G. (2008). Controllable switching of vortex chirality in magnetic nanodisks by a field pulse. *Applied Physics Letters*, *92*(1), 012503.

[17] Pinilla-Cienfuegos, E., Mañas-Valero, S., Forment-Aliaga, A., & Coronado, E. (2016). Switching the magnetic vortex core in a single nanoparticle. *ACS nano*, *10*(2), 1764–1770.

[18] Fischer, P., & Ohldag, H. (2015). X-rays and magnetism. *Reports on Progress in Physics*, *78*(9), 094501.

[19] Im, M.-Y., Fischer, P., Yamada, K., Sato, T., Kasai, S., Nakatani, Y., & Ono, T. (2012). Symmetry breaking in the formation of magnetic vortex states in a permalloy nanodisk. *Nature communications*, *3*(1), 1–6.

[20] Potonié, R. (1928). Hund, f.-linienspektren und periodisches system der elemente. *Scientia, Rivista di Scienza*, *22*(44).

[21] Pauli, W. (1925). Über den zusammenhang des abschlusses der elektronengruppen im atom mit der komplexstruktur der spektren. *Einführung und Originaltexte*, (p. 229).

[22] Heisenberg, W. (1985). Zur theorie des ferromagnetismus. In *Original Scientific Papers Wissenschaftliche Originalarbeiten*, (pp. 580–597). Springer.

[23] Cullity, B. D., & Graham, C. D. (2011). *Introduction to magnetic materials*. John Wiley & Sons.

[24] Mermin, A. (1978). Solid state physics. von nw ashcroft und nd mermin; holt, rinehart and winston, new york 1976, xxii, 826 seiten, 19, 95. *Physik in unserer Zeit*, *9*(1), 33–33.

[25] Chikazumi, S., & Graham, C. D. (1997). *Physics of ferromagnetism*. 94. Oxford university press.

[26] McQuarrie, D. A. (2000). *Statistical mechanics*. Sterling Publishing Company.

[27] Kittel, C., McEuen, P., & McEuen, P. (1996). *Introduction to solid state physics*, vol. 8. Wiley New York.

[28] Magnani, N. (2005). Ferromagnetism. In F. Bassani, G. L. Liedl, & P. Wyder (Eds.) *Encyclopedia of Condensed Matter Physics*, (pp. 201–210). Oxford: Elsevier.
https://www.sciencedirect.com/science/article/pii/B0123694019011153

[29] Meng, Q. (2008). *Magnetic Vortex*. Ph.D. thesis, PhD thesis.

[30] Ionescu, A., Llandro, J., & Ziebeck, K. R. (2019). Magnetism, magnetic materials, and nanoparticles. In *Magnetic Nanoparticles in Biosensing and Medicine*, (pp. 1–51). Cambridge University Press.

[31] Bhatia, E., Barber, Z. H., Maasilta, I. J., & Senapati, K. (2019). Domain wall induced modulation of low field ht phase diagram in patterned superconductor-ferromagnet stripes. *AIP Advances*, *9*(4), 045107.

[32] Mermin, N. D. (1979). The topological theory of defects in ordered media. *Reviews of Modern Physics*, *51*(3), 591.

[33] Shinjo, T., Okuno, T., Hassdorf, R., Shigeto, K., & Ono, T. (2000). Magnetic vortex core observation in circular dots of permalloy. *Science*, *289*(5481), 930–932.

[34] Tóbik, J., Cambel, V., & Karapetrov, G. (2012). Dynamics of vortex nucleation in nanomagnets with broken symmetry. *Physical Review B*, *86*(13), 134433.

[35] Wachowiak, A., Wiebe, J., Bode, M., Pietzsch, O., Morgenstern, M., & Wiesendanger, R. (2002). Direct observation of internal spin structure of magnetic vortex cores. *science*, *298*(5593), 577–580.

[36] Pratzer, M., Elmers, H. J., Bode, M., Pietzsch, O., Kubetzka, A., & Wiesendanger, R. (2001). Atomic-scale magnetic domain walls in quasi-one-dimensional fe nanostripes. *Phys. Rev. Lett.*, *87*, 127201.
https://link.aps.org/doi/10.1103/PhysRevLett.87.127201

[37] Heinze, S., Bode, M., Kubetzka, A., Pietzsch, O., Nie, X., Blügel, S., & Wiesendanger, R. (2000). Real-space imaging of two-dimensional antiferromagnetism on the atomic scale. *Science*, *288*(5472), 1805–1808.
https://www.science.org/doi/abs/10.1126/science.288.5472.1805

[38] Kubetzka, A., Bode, M., Pietzsch, O., & Wiesendanger, R. (2002). Spin-polarized scanning tunneling microscopy with antiferromagnetic probe tips. *Phys. Rev. Lett.*, *88*, 057201.
https://link.aps.org/doi/10.1103/PhysRevLett.88.057201

[39] Braun, H.-B. (2012). Topological effects in nanomagnetism: from superparamagnetism to chiral quantum solitons. *Advances in Physics*, *61*(1), 1–116.

[40] Bader, S. D. (2006). Colloquium: Opportunities in nanomagnetism. *Reviews of Modern Physics*, *78*(1), 1.

[41] Cowburn, R. P. (2007). Change of direction. *Nature Materials*, *6*(4), 255–256.

[42] Sugimoto, S., Fukuma, Y., Kasai, S., Kimura, T., Barman, A., & Otani, Y. (2011). Dynamics of coupled vortices in a pair of ferromagnetic disks. *Physical Review Letters*, *106*(19), 197203. https://link.aps.org/doi/10.1103/PhysRevLett.106.197203

[43] Fu, X., Pollard, S. D., Chen, B., Yoo, B.-K., Yang, H., & Zhu, Y. (2018). Optical manipulation of magnetic vortices visualized in situ by lorentz electron microscopy. *Science Advances*, *4*(7), eaat3077. http://advances.sciencemag.org/content/4/7/eaat3077.abstract

[44] Pigeau, B., de Loubens, G., Klein, O., Riegler, A., Lochner, F., Schmidt, G., Molenkamp, L. W., Tiberkevich, V. S., & Slavin, A. N. (2010). A frequency-controlled magnetic vortex memory. *Applied Physics Letters*, *96*(13), 132506. https://doi.org/10.1063/1.3373833

[45] García Sánchez, F. (2007). Modeling of field and thermal magnetization reversal in nanostructured magnetic materials.

[46] Abo, G. S., Hong, Y.-K., Park, J., Lee, J., Lee, W., & Choi, B.-C. (2013). Definition of magnetic exchange length. *IEEE Transactions on Magnetics*, *49*(8), 4937–4939.

[47] Miltat, J. E., Donahue, M. J., et al. (2007). Numerical micromagnetics: Finite difference methods. *Handbook of magnetism and advanced magnetic materials*, *2*, 742–764.

[48] Frei, E. H., Shtrikman, S., & Treves, D. (1957). Critical size and nucleation field of ideal ferromagnetic particles. *Physical Review*, *106*(3), 446.

[49] Seberino, C., & Bertram, H. N. (1997). Micromagnetics of long ferromagnetic particles. *IEEE Transactions on Magnetics*, *33*(5), 3055–3057.

[50] Ferré, R. (1997). Large scale micromagnetic calculations for finite and infinite 3dferromagnetic systems using fft. *Computer physics communications*, *105*(2-3), 169–186.

[51] Guslienko, K. Y., Novosad, V., Otani, Y., Shima, H., & Fukamichi, K. (2001). Magnetization reversal due to vortex nucleation, displacement, and annihilation in submicron ferromagnetic dot arrays. *Physical Review B*, *65*(2), 024414.

[52] Yu, D., Kang, J., Berakdar, J., & Jia, C. (2020). Nondestructive ultrafast steering of a magnetic vortex by terahertz pulses. *NPG Asia Materials*, *12*(1), 1–8.

[53] Yakata, S., Miyata, M., Nonoguchi, S., Wada, H., & Kimura, T. (2010). Control of vortex chirality in regular polygonal nanomagnets using in-plane magnetic field. *Applied Physics Letters*, *97*(22), 222503.

[54] Metlov, K. L., & Guslienko, K. Y. (2002). Stability of magnetic vortex in soft magnetic nano-sized circular cylinder. *Journal of magnetism and magnetic materials*, *242*, 1015–1017.

[55] Scholz, W., Guslienko, K. Y., Novosad, V., Suess, D., Schrefl, T., Chantrell, R., & Fidler, J. (2003). Transition from single-domain to vortex state in soft magnetic cylindrical nanodots. *Journal of magnetism and magnetic materials*, *266*(1-2), 155–163.

[56] Usov, N., & Peschany, S. (1993). Magnetization curling in a fine cylindrical particle. *Journal of Magnetism and Magnetic Materials*, *118*(3), L290–L294.

[57] Usov, N., & Peschany, S. (1994). Vortex magnetization distribution in a thin ferromagnetic cylinder. *Fiz. Met. Metalloved*, *12*, 1–13.

[58] Metlov, K. L., & Lee, Y. (2008). Map of metastable states for thin circular magnetic nanocylinders. *Applied Physics Letters*, *92*(11), 112506.

[59] Pigeau, B., De Loubens, G., Klein, O., Riegler, A., Lochner, F., Schmidt, G., Molenkamp, L., Tiberkevich, V., & Slavin, A. (2010). A frequency-controlled magnetic vortex memory. *Applied Physics Letters*, *96*(13), 132506.

[60] Bussmann, K., Prinz, G., Cheng, S.-F., & Wang, D. (1999). Switching of vertical giant magnetoresistance devices by current through the device. *Applied physics letters*, *75*(16), 2476–2478.

[61] Van Waeyenberge, B., Puzic, A., Stoll, H., Chou, K., Tyliszczak, T., Hertel, R., Fähnle, M., Brückl, H., Rott, K., Reiss, G., et al. (2006). Magnetic vortex core reversal by excitation with short bursts of an alternating field. *Nature*, *444*(7118), 461–464.

[62] Guslienko, K. Y., Lee, K.-S., & Kim, S.-K. (2008). Dynamic origin of vortex core switching in soft magnetic nanodots. *Physical review letters*, *100*(2), 027203.

[63] De Loubens, G., Riegler, A., Pigeau, B., Lochner, F., Boust, F., Guslienko, K. Y., Hurdequint, H., Molenkamp, L., Schmidt, G., Slavin, A. N., et al. (2009). Bistability of vortex core dynamics in a single perpendicularly magnetized nanodisk. *Physical Review Letters*, *102*(17), 177602.

[64] Vavassori, P., Grimsditch, M., Metlushko, V., Zaluzec, N., & Ilic, B. (2005). Magnetoresistance of single magnetic vortices. *Applied Physics Letters*, *86*(7), 072507.

[65] Baibich, M. N., Broto, J. M., Fert, A., Van Dau, F. N., Petroff, F., Etienne, P., Creuzet, G., Friederich, A., & Chazelas, J. (1988). Giant magnetoresistance of (001) fe/(001) cr magnetic superlattices. *Physical review letters*, *61*(21), 2472.

[66] Daughton, J., Brown, J., Chen, E., Beech, R., Pohm, A., & Kude, W. (1994). Magnetic field sensors using gmr multilayer. *IEEE Transactions on magnetics*, *30*(6), 4608–4610.

[67] Tsang, C., Fontana, R. E., Lin, T., Heim, D. E., Speriosu, V. S., Gurney, B. A., & Williams, M. L. (1994). Design, fabrication and testing of spin-valve read heads for high density recording. *IEEE Transactions on Magnetics*, *30*(6), 3801–3806.

[68] Dax, M. (1997). The non-volatile memory challenge. *Semiconductor international*, *20*(10), 84–89.

[69] Pratt Jr, W., Lee, S.-F., Slaughter, J., Loloee, R., Schroeder, P., & Bass, J. (1991). Perpendicular giant magnetoresistances of ag/co multilayers. *Physical review letters*, *66*(23), 3060.

[70] Hrkac, G., Keatley, P. S., Bryan, M. T., & Butler, K. (2015). Magnetic vortex oscillators. *Journal of Physics D: Applied Physics*, *48*(45), 453001.

[71] Pankhurst, Q. A., Connolly, J., Jones, S. K., & Dobson, J. (2003). Applications of magnetic nanoparticles in biomedicine. *Journal of physics D: Applied physics*, *36*(13), R167.

[72] Torrejon, J., Riou, M., Araujo, F. A., Tsunegi, S., Khalsa, G., Querlioz, D., Bortolotti, P., Cros, V., Yakushiji, K., Fukushima, A., et al. (2017). Neuromorphic computing with nanoscale spintronic oscillators. *Nature*, *547*(7664), 428–431.

[73] Suess, D., Bachleitner-Hofmann, A., Satz, A., Weitensfelder, H., Vogler, C., Bruckner, F., Abert, C., Prügl, K., Zimmer, J., Huber, C., et al. (2018). Topologically protected vortex structures for low-noise magnetic sensors with high linear range. *Nature Electronics*, *1*(6), 362–370.

[74] Vitol, E. A., Novosad, V., & Rozhkova, E. A. (2012). Microfabricated magnetic structures for future medicine: from sensors to cell actuators. *Nanomedicine*, *7*(10), 1611–1624.

[75] Goiriena-Goikoetxea, M., García-Arribas, A., Rouco, M., Svalov, A., & Barandiaran, J. (2016). High-yield fabrication of 60 nm permalloy nanodiscs in well-defined magnetic vortex state for biomedical applications. *Nanotechnology*, *27*(17), 175302.

[76] Hanarp, P., Sutherland, D. S., Gold, J., & Kasemo, B. (2003). Control of nanoparticle film structure for colloidal lithography. *Colloids and Surfaces A: Physicochemical and Engineering Aspects*, *214*(1-3), 23–36.

[77] Fredriksson, H., Alaverdyan, Y., Dmitriev, A., Langhammer, C., Sutherland, D. S., Zäch, M., & Kasemo, B. (2007). Hole–mask colloidal lithography. *Advanced Materials*, *19*(23), 4297–4302.

[78] Cowburn, R. P., Koltsov, D., Adeyeye, A., Welland, M., & Tricker, D. (1999). Single-domain circular nanomagnets. *Physical Review Letters*, *83*(5), 1042.

[79] Novosad, V., Guslienko, K. Y., Shima, H., Otani, Y., Kim, S., Fukamichi, K., Kikuchi, N., Kitakami, O., & Shimada, Y. (2002). Effect of interdot magnetostatic interaction on magnetization reversal in circular dot arrays. *Physical Review B*, *65*(6), 060402.

[80] Chung, S.-H., McMichael, R. D., Pierce, D. T., & Unguris, J. (2010). Phase diagram of magnetic nanodisks measured by scanning electron microscopy with polarization analysis. *Physical Review B*, *81*(2), 024410.

[81] Antos, R., & Otani, Y. (2009). Simulations of the dynamic switching of vortex chirality in magnetic nanodisks by a uniform field pulse. *Physical Review B*, *80*(14), 140404. https://link.aps.org/doi/10.1103/PhysRevB.80.140404

[82] Dumas, R. K., Gilbert, D. A., Eibagi, N., & Liu, K. (2011). Chirality control via double vortices in asymmetric co dots. *Physical Review B*, *83*(6), 060415. https://link.aps.org/doi/10.1103/PhysRevB.83.060415

[83] Uhlíř, V., Urbánek, M., Hladík, L., Spousta, J., Im, M. Y., Fischer, P., Eibagi, N., Kan, J. J., Fullerton, E. E., & Šikola, T. (2013). Dynamic switching of the spin circulation in tapered magnetic nanodisks. *Nature Nanotechnology*, *8*(5), 341–346. https://doi.org/10.1038/nnano.2013.66

[84] Choi, B. C., Rudge, J., Girgis, E., Kolthammer, J., Hong, Y. K., & Lyle, A. (2007). Spin-current pulse induced switching of vortex chirality in permalloycuco nanopillars. *Applied Physics Letters*, *91*(2), 022501. https://doi.org/10.1063/1.2756109

[85] Luo, Y., Wu, Y., Yu, C., Li, H., Wen, J., Zhu, L., Qian, Z., & Zhou, T. (2019). Separated edge-soliton-mediated dynamic switching of vortex chirality and polarity. *Physical Review Applied*, *11*(4), 044090.

[86] Ross, C., Hwang, M., Shima, M., Cheng, J., Farhoud, M., Savas, T., Smith, H. I., Schwarzacher, W., Ross, F., Redjdal, M., et al. (2002). Micromagnetic behavior of electrodeposited cylinder arrays. *Physical Review B*, *65*(14), 144417.

[87] Metlov, K. L. (2013). Equilibrium large vortex state in ferromagnetic disks. *Journal of Applied Physics*, *113*(22), 223905.

[88] Vargas, N., Allende, S., Leighton, B., Escrig, J., Mejía-López, J., Altbir, D., & Schuller, I. K. (2011). Asymmetric magnetic dots: a way to control magnetic properties. *Journal of Applied Physics*, *109*(7), 073907.

[89] Schneider, M., Hoffmann, H., & Zweck, J. (2001). Magnetic switching of single vortex permalloy elements. *Applied Physics Letters*, *79*(19), 3113–3115.

[90] Kimura, T., Otani, Y., Masaki, H., Ishida, T., Antos, R., & Shibata, J. (2007). Vortex motion in chilarity-controlled pair of magnetic disks. *Applied Physics Letters*, *90*(13), 132501.

[91] Pribiag, V., Krivorotov, I., Fuchs, G., Braganca, P., Ozatay, O., Sankey, J., Ralph, D., & Buhrman, R. (2007). Magnetic vortex oscillator driven by dc spin-polarized current. *Nature Physics*, *3*(7), 498–503.

[92] Hertel, R., Gliga, S., Fähnle, M., & Schneider, C. (2007). Ultrafast nanomagnetic toggle switching of vortex cores. *Physical Review Letters*, *98*(11), 117201.

[93] Kravchuk, V. P., Gaididei, Y., & Sheka, D. D. (2009). Nucleation of a vortex-antivortex pair in the presence of an immobile magnetic vortex. *Physical Review B*, *80*(10), 100405.

[94] Kammerer, M., Weigand, M., Curcic, M., Noske, M., Sproll, M., Vansteenkiste, A., Van Waeyenberge, B., Stoll, H., Woltersdorf, G., Back, C. H., et al. (2011). Magnetic vortex core reversal by excitation of spin waves. *Nature Communications*, *2*(1), 1–6.

[95] Pigeau, B., De Loubens, G., Klein, O., Riegler, A., Lochner, F., Schmidt, G., & Molenkamp, L. W. (2011). Optimal control of vortex-core polarity by resonant microwave pulses. *Nature Physics*, *7*(1), 26–31.

[96] Lee, K.-S., Yoo, M.-W., Choi, Y.-S., & Kim, S.-K. (2011). Edge-soliton-mediated vortex-core reversal dynamics. *Physical review letters*, *106*(14), 147201.

[97] Choi, Y.-S., Yoo, M.-W., Lee, K.-S., Yu, Y.-S., Jung, H., & Kim, S.-K. (2010). Out-of-plane current controlled switching of the fourfold degenerate state of a magnetic vortex in soft magnetic nanodots. *Applied Physics Letters*, *96*(7), 072507.

[98] Kronmüller, H. (2007). General micromagnetic theory. *Handbook of Magnetism and Advanced Magnetic Materials*.

[99] Landau, L., & Lifshitz, E. (1935). Anomalous high-frequency resistance of ferromagnetic metals. *Phys. Z. Sowjetunion*, *8*, 153–169.

[100] Berkov, D. V. (2007). Magnetization dynamics including thermal fluctuations: Basic phenomenology, fast remagnetization processes and transitions over high-energy barriers. *Handbook of Magnetism and Advanced Magnetic Materials*.

[101] Gilbert, T. L. (2004). A phenomenological theory of damping in ferromagnetic materials. *IEEE transactions on magnetics*, *40*(6), 3443–3449.

[102] Slonczewski, J. C. (1996). Current-driven excitation of magnetic multilayers. *Journal of Magnetism and Magnetic Materials*, *159*(1-2), L1–L7.

[103] Labrune, M., & Miltat, J. (1995). Wall structures in ferro/antiferromagnetic exchange-coupled bilayers: a numerical micromagnetic approach. *Journal of Magnetism and Magnetic Materials*, *151*(1-2), 231–245.

[104] Kákay, A. (2005). Numerical investigations of micromagnetic structures.

[105] Newell, A. J., Williams, W., & Dunlop, D. J. (1993). A generalization of the demagnetizing tensor for nonuniform magnetization. *Journal of Geophysical Research: Solid Earth*, *98*(B6), 9551–9555.

[106] O'handley, R. C. (2000). *Modern magnetic materials: principles and applications*. Wiley.

[107] Kittel, C. (1949). Physical theory of ferromagnetic domains. *Reviews of modern Physics*, *21*(4), 541.

[108] Aharoni, A., et al. (2000). *Introduction to the Theory of Ferromagnetism*, vol. 109. Clarendon Press.

[109] Yin, L., Wei, D., Lei, N., Zhou, L., Tian, C., Dong, G., Jin, X., Guo, L., Jia, Q., & Wu, R. (2006). Magnetocrystalline anisotropy in permalloy revisited. *Physical review letters*, *97*(6), 067203.

[110] You, C.-Y., Sung, I. M., & Joe, B.-K. (2006). Analytic expression for the temperature of the current-heated nanowire for the current-induced domain wall motion. *Applied physics letters*, *89*(22), 222513.

[111] Ito, K., Devolder, T., Chappert, C., Carey, M., & Katine, J. (2006). Probabilistic behavior in subnanosecond spin transfer torque switching. *Journal of applied physics*, *99*(8), 08G519.

[112] Finocchio, G., Carpentieri, M., Azzerboni, B., Torres, L., Martinez, E., & Lopez-Diaz, L. (2006). Micromagnetic simulations of nanosecond magnetization reversal processes in magnetic nanopillar. *Journal of applied physics*, *99*(8), 08G522.

[113] Moskalenko, A. S., Zhu, Z.-G., & Berakdar, J. (2017). Charge and spin dynamics driven by ultrashort extreme broadband pulses: a theory perspective. *Physics Reports*, *672*, 1–82.

[114] Boardman, R. P. (2005). *Computer simulation studies of magnetic nanostructures*. Ph.D. thesis, University of Southampton.

[115] Goiriena-Goikoetxea, M., Guslienko, K., Rouco, M., Orue, I., Berganza, E., Jaafar, M., Asenjo, A., Fernández-Gubieda, M., Barquín, L. F., & García-Arribas, A. (2017). Magnetization reversal in circular vortex dots of small radius. *Nanoscale*, *9*(31), 11269–11278.

[116] Barrera, G., Celegato, F., Coisson, M., Manzin, A., Lupi, F. F., Seguini, G., Boarino, L., Aprile, G., Perego, M., & Tiberto, P. (2017). Magnetization switching in high-density magnetic nanodots by a fine-tune sputtering process on a large-area diblock copolymer mask. *Nanoscale*, *9*(43), 16981–16992.

[117] Li, W., Qiu, X., Lv, B., Zhang, B., Tang, J., Xu, J., Tian, K., Zhao, Z., Zeng, Y., Huang, X., et al. (2022). Free-standing 2d ironene with magnetic vortex structure at room temperature. *Matter*, *5*(1), 291–301.

[118] Wu, Y., Jiang, J., Wang, Y., Li, J., Xiong, Y., & Kong, L. (2022). Stabilizations and field-driven core reversals of magnetic vortices in fe3sn2 disks. *Applied Physics Letters*, *120*(4), 042403.

[119] Guslienko, K. Y., Ivanov, B., Novosad, V., Otani, Y., Shima, H., & Fukamichi, K. (2002). Eigenfrequencies of vortex state excitations in magnetic submicron-size disks. *Journal of Applied Physics*, *91*(10), 8037–8039.

[120] Kim, S.-K., Choi, Y.-S., Lee, K.-S., Guslienko, K. Y., & Jeong, D.-E. (2007). Electric-current-driven vortex-core reversal in soft magnetic nanodots. *Applied Physics Letters*, *91*(8), 082506.

[121] Scholz, W., Schrefl, T., & Fidler, J. (2001). Micromagnetic simulation of thermally activated switching in fine particles. *Journal of Magnetism and Magnetic Materials*, *233*(3), 296–304.

[122] Brown Jr, W. F. (1963). Thermal fluctuations of a single-domain particle. *Physical review*, *130*(5), 1677.